# Stony Brook University

# Electronic Transport Properties of Semiconductor Nanostructures

A Dissertation Presented

by

## Yan Zhang

to

The Graduate School

in Partial Fulfillment of the Requirements

for the Degree of

## Doctor of Philosophy

in

## Physics

Stony Brook University

May 2011

**Stony Brook University**

The Graduate School

# Yan Zhang

We, the dissertation committee for the above candidate for the Doctor of Philosophy degree, hereby recommend acceptance of this dissertation.

Emilio E. Mendez - Dissertation Advisor
Professor, Department of Physics and Astronomy

Xu Du - Chairperson of Defense
Assistant Professor, Department of Physics and Astronomy

Thomas T. S. Kuo
Professor, Department of Physics and Astronomy

Maria Victoria Fernandez-Serra
Assistant Professor, Department of Physics and Astronomy

Sergey Suchalkin
Research Professor, Department of Electrical and Computer Engineering

This dissertation is accepted by the Graduate School.

Lawrence Martin
Dean of the Graduate School

Abstract of the Dissertation

# Electronic Transport Properties of Semiconductor Nanostructures

by

**Yan Zhang**

**Doctor of Philosophy**

in

**Physics**

Stony Brook University

2011

With reduced size and dimensions, semiconductor nanostructures have dramatic difference in electrical properties than their bulk counterparts. These differences have raised many interesting topics, such as quantum Hall effects and bandgap engineering. By utilizing these properties of nanostructures, numerous electrical devices have been proposed and created to improve human life quality and production efficiency.

Graphene, carbon atoms formed in only one-atomic-layer, has been discovered in lab in 2004 and raised a lot of attentions. It has unique electronic band structure and promising applications. Many fundamental physics questions and practical limitations on device functions need to be addressed.

We have investigated the low-frequency 1/f noise, which poses a limit on the signal-to-noise ratio in broad band electrical circuit, in both suspended and on-substrate graphene field-effect transistors, from T = 30 to 300K. We have found that, compared to on-substrate devices, in general suspended graphene devices show lower 1/f noise, as a result of their higher mobility. We explain the observed noise dependence on gate voltage using the Hooge's empirical relation with a variable Hooge parameter.

We have also studied metal-insulator transition in monolayer graphene, and a phase diagram of metal and insulator phases from reported and our own results was proposed. Anomalous quantum Hall effect in ABC-stacked trilayer graphene was also studied, and we found chiral fermions with Berry's phase $3\pi$ and unusual Landau level quantization with 12-fold and 4-fold degeneracy in the $n=0$ and $n > 0$ Landau levels, respectively. With the help of spacially resolved scanning photocurrent, we have studied charge transport in graphene in quantum Hall regime. And we found that the net photocurrent is determined by hot carriers transported to the device edges, where quantum Hall edge states provide efficient channels for their extraction to contacts.

Moreover, optical bandgap and electrical properties of $(GaN)_{1-x}(ZnO)_x$ solid solution nanowire have been studied to explore the possibility of using this material as a photovoltaic catalyst in water splitting for generating renewable energy. The nanowires with composition $x \approx 0.12$ were found with an optical bandgap $\sim 2.7$ eV. And the nanowire FETs were n-type conduction, with background carrier density $\sim 10^{19}/cm^3$ and electron mobility $\sim 1 cm^2/V \cdot s$.

To my parents and my fiancée.

# Contents

# List of Figures

# List of Tables

# Acknowledgements

Graduate school has taught me to be not only an independent researcher but also a team player, and the years in Stony Brook were such an enjoyable adventure in my life.

I would like to thank my advisor, Prof. Emilio Mendez, for his instructions and support during my PhD study. He impressed me so many times with his unbelievable memory and straightforward logic thinking. He led me through the ups and downs with his passion in research and his constant encouragements.

I am very lucky to get the opportunities to work together with many prestigious scientists from Stony Brook University (SBU) and Brookhaven National Laboratory (BNL). It was a pleasure to work together with Prof. Xu Du for a project on graphene, I learned a lot of knowledge and experimental skills about graphene from him. His passion in science and fruitful ideas inspired me. I would also like to thank Prof. Liyuan Zhang, who used to be a postdoc in BNL. He taught me how to make graphene FETs. And I enjoyed the days and nights that we worked together fabricating devices in the cleanroom and running magnet in the lab. Prof. George Nazin, who also used to be a postdoc in BNL, we worked together on a joint project on photocurrent study in graphene. His hard working ethic and in-depth knowledge in physics has been a major source to deliver the nice results. Moreover, I would like to thank Dr. Weiqiang Han from Center for Functional Nanomaterials (CFN) at BNL, who gave me the opportunities to work on first-hand photovoltaic nanomaterials.

Now I would like thank my colleagues who led me into the laboratories. Bent Nielsen, A.K.M. Newaz and Megumi Kinoshita were the ones who taught me first-hand knowledge and experiences in the labs. Without them, I would be begging Emilio all the time to come to the lab and teaching me the equipments that I've never seen in my life before. Moreover, Fernando Camino, Chang-Yong Nam, Ming Lu, Aaron Stein and Don Elliott were the ones who helped me to get used to the instruments in CFN. I would also like to thank Paul DiMatteo, Mark Jablonski, Jeffrey Slechta, Jeffrey Thomas and Walter Schmeling from the machine shop. They offered me with their expertise in machining, and I enjoyed the days I spent in the student machine shop to make fancy pieces for my research. Eugene Shafto and Chuck Pancake from the electronics shop have been the ones who helped me with expertise and knowledge in electronic circuits.

Finally, I want to thank my family and friends. My parents are always supportive to my decisions, and they have taught me to be an honest and hard working person with their own examples. I would also love to express my appreciation to my fiancée. She brought so much joy and courage to me that I can survive the jungle of graduate school. I would like to thank all my friends who have made my life in Stony Brook a superb experience, and I will list them in my heart instead of occupying pages of the dissertation here.

# List of Publications

- Mobility Dependent Low Frequency Noise in Graphene Transistors

  **Y. Zhang**, E. E. Mendez, and X. Du. To be submitted.

- The Experimental Observation of Quantum Hall Effect of $l = 3$ Chiral Quasiparticles in Trilayer Graphene

  L. Zhang, **Y. Zhang**, J. Camacho, M. Khodas, and I. A. Zaliznyak. To be submitted.

- Visualization of Charge Transport through Landau Levels in Graphene

  G. Nazin, **Y. Zhang**, L. Zhang, E. Sutter, and P. Sutter. *Nature Physics* **6**, 870-874 (2010)

- Metal to Insulator Transition on the N=0 Landau Level in Graphene

  L. Zhang, **Y. Zhang**, M. Khodas, T. Valla, and I. A. Zaliznyak. *Physical Review Letters* **105**, 046804 (2010)

- Growth and Electronic Properties of GaN/ZnO Solid Solution Nanowires

  W. Han, **Y. Zhang**, C. Nam, C. T. Black, and E. E. Mendez. *Applied Physics Letters* **97**, 083108 (2010)

- Magnéli Phases $Ti_nO_{2n-1}$ Nanowires: Formation, Optical, and Transport Properties

  W. Han, and **Y. Zhang**. *Applied Physics Letters* **92**, 203117 (2008)

# Chapter 1

# Introduction

## 1.1 Semiconductor nanostructures

Semiconductors, which are materials with a fundamental energy band gap between that of a metal and an insulator, are the backbone of modern electronics because of their great flexibility in terms of allowing the control of electronic and optical properties. In computers, telecommunications, health, and transportation, they are almost everywhere in our daily life. The demand for smaller, faster and more energy efficient semiconductor devices has been driving the multibillion business for years, and it continues that way. Following the International Technology Roadmap for Semiconductors, transistor dimensions have been reduced from $10\mu$m in 1971 to 32nm in 2010, and the electronic properties of material have changed dramatically due to the size reduction.

Generally, a nanostructure can be defined as a structure with size smaller than one hundred nanometer in at least one of the three dimensions, with a variety from two to zero dimension confinements, i.e. quantum well, quantum wire and quantum dot for 2-, 1-, 0-dimensions nanostructures, respectively. The electronic properties of structures depend on

the dimensionality and the geometric details of the materials.

About forty years ago, Dr. Gordon E. Moore, Intel's co-founder, described the trend of progress in electronics with an empirical observation: *the number of transistors that can be placed in an integrated circuit with respect to the minimum component cost doubles approximately every two years*, which is now known as Moore's law. So far the semiconductor industry is still on track with the prediction, with the help of mature silicon technology, which enjoys the advantages of ultra low defect density, thin and stable dielectric $SiO_2$, and extraordinary low cost. However, fundamental limits pose obstacles for better electronics, such as electron mobility poses a limit on transistor operational frequency. Thus the scientific and technology world have been looking for alternative materials for years, which can give rise to cheaper and faster devices. So far, numerous materials have been developed, but none of them can replace silicon in terms of cost and overall performance.

People have put in a lot of effort on carbon, which is easy to access; numerous groundbreaking discoveries have been made during the past twenty years. Carbon nanotubes (CNT) raised a lot of interest, due to its high mobility and potential as a ballistic transistor. However, the difficulties in sorting nanotubes (metallic or semiconducting, diameter, and chirality) make it hard to utilize CNTs in industrial scale electrical circuits. In 2004, graphene, carbon atoms formed in a single atomic layer, was discovered in the laboratory. The unique electronic structure, high electrical mobility and potential to be engineered with existing Si technology has brought huge interest in graphene from both the academic and industrial worlds. Thus studying the electrical properties of graphene has become an interesting work to do.

Besides making smaller and faster devices, finding energies to power up these devices is also important. The majority of energy supporting human activities is from coal, oil and natural gas, which took hundreds of millions of years to form. These energy sources

will be used up eventually. Thus saving energy and exploring new energy sources become an important issue for society. Solar energy, which used to be stored in coal, oil and natural gas, is among one of the promising renewable energy sources. One effective way to use solar energy is through solar cells, which collect solar light and transform it to electricity. On the other hand, photocatalysis is also a promising direction, in which one uses solar energy to split a water molecule into oxygen and hydrogen, and the produced hydrogen can be stored and used as a fuel that could be burned whenever it is needed. Thus finding a suitable photocatalyst with high catalysis efficiency is a crucial step towards obtaining $H_2$ fuel. Nanostructuring photocatalysts is one of the ways to find highly efficient photocatalysts, due to its large surface to volume ratio which is crucial in surface reactions in the photocatalytic process.

In the following two sections, background of graphene and photocatalyst is covered separately.

## 1.2    What is graphene?

Graphene, a flat monolayer of carbon atoms formed in a 2D honeycomb lattice[1], has been studied by theoriticians for over sixty years and is widely used to describe properties of carbon-based materials. It can be stacked into 3D graphite, rolled into 1D carbon nanotube or wrapped up into 0D fullerene. It was believed not to exist stably and freely as its curved counterparts – nanotube and fullerene. However, in 2004, Andre Geim and Konstantin Novoselov at Manchester University in England demonstrated its existence in the laboratory[1], and their work was awarded the Nobel prize in physics in 2010. The experiment was as simple as drawing on a piece of paper with a pencil. Basically, the researchers

---

[1]Although strictly speaking, graphene consists of a monolayer of carbon atoms, we often speak of bilayer or trilayer graphene which refer to two or three atomic layers of carbon atoms, respectively.

used scotch tape to peel bulk graphite to very thin layers and stuck them onto a $SiO_2/Si$ wafer. After removing the adhesive tapes, an atomic thin graphite layer was magically found on the wafer under an optical microscope. The thickness of $SiO_2$ appeared to be critical for successful observations of monolayer graphene on wafers. It was found that 90nm and 300nm thick $SiO_2$ have good contrast between graphene and wafer.

Since the discovery in 2004, research on graphene has exploded. Graphene has exceptional mechanical, electronic and optical properties. It is the thinnest however strongest material ever measured, with Young's modulus $\sim$1.0TPa [2]. The charge carriers in graphene have huge intrinsic mobility and zero effective mass, and they can travel for micrometers without scattering at room temperature. Graphene has been demonstrated as a sensor to detect pH in solution[3] and detect single gas molecule[4]. Additionally, graphene has very high optical transparency, with $\sim$ 98% in monolayer graphene and $\sim$ 95% in bilayer graphene[5], which together with its high electrical conductivity makes it a very good candidate as a transparent conductor for LCD and solar cells.

In order to produce graphene in industrial scale, a mass production method is needed, since the scotch tape exfoliation method would be too slow and costly. So far graphene has been successfully grown on SiC [6, 7], and a few different metals, such as Ru, Ni, Cu [8–10]. However, there hasn't been a good way to transfer graphene from its initial substrate onto a dielectric substrate to make field effect transistors (FET). People have tried coating as-grown graphene with resist and etching away the substrate, and then placing the graphene-attached resist onto the target wafer and dissolving the resist to make successful transfer. The transferred graphene flakes appear to have lots of wrinkles and cracks, which degrade the electronic properties dramatically. These engineering issues need to be solved, in order to improve the quality of devices made from grown graphene.

The exceptional electronic and optical properties of graphene make it a good candidate

for many applications. However, several fundamental electronic transport properties need to be addressed to predict and control the electronic behavior of graphene devices.

## 1.3   Topics we want to study on graphene

Noise in electrical systems refers to the electrical signal fluctuations in excess of the target signal, posing a limit on signal to noise ratio, which is important in electrical systems. The fluctuations are not always undesirable, and the nature of them usually depend on the underlying physical process. By measuring noise, information not available from time-averaged measurements, can be retrieved. Usually electrical measurements in a conductor, such as voltage, current and resistance, are time-averaged values. These measurements do not contain any information about the fluctuations. In order to measure fluctuations, time resolved methods are needed.

There are three types of electrical noise, thermal noise, shot noise, and low-frequency or 1/f noise. Thermal noise is due to thermal fluctuations of charge carriers in a conductor, and is frequency-independent. Shot noise is due to the particle nature of charge carriers, and also is frequency-independent (becoming frequency-dependent in very high frequency). When average current $\overline{I}$ passes through a potential barrier randomly and independently, its spectral density of current noise is given by $S_I = 2e\overline{I}$. The shot noise may deviate from this value when the motions of charge carriers passing through the potential barrier are not independent.

Low-frequency noise arises from mobility fluctuations of charge carriers or from number fluctuations, caused by charge trapping and detrapping. Low-frequency noise is frequency-dependent, with a spectral density in the resistance that typically follows $S_R \propto 1/f$. This type of noise is important in broadband and low-frequency circuits.

Since low-frequency noise carries information about the number and mobility fluctuations in a conductor, studying its behavior in graphene helps elucidate the influence of charge traps and different scattering mechanisms on the electrical conduction process.

Besides electrical noise, the fundamental electronic structure is interesting to a larger scientific community because it determines the macroscopic uniqueness of graphene. Graphene has a linear energy dispersion, which is similar to photon, and it is quite different from quadratic dispersion in standard semiconductors. The charge carriers in graphene can be explained by relativistic Dirac equation. It is a zero band gap semiconductor or semimetal, and the charge polarity can be easily switched from hole to electron by changing gate voltage from negative to positive values, which is impossible in traditional semiconductors.

The electronic transport of graphene in magnetic field is also very interesting. It has four-fold degeneracy in the quantum Hall effect (QHE), which is due to spin and valley degeneracy[11]. Numerous theoretical and experimental work have been done on graphene in the quantum Hall regime. However, the nature of the electronic states at $n = 0$ Landau level are still unclear. Some theories predict unusual metallic transport via gapless edge states[12, 13] and other suggest a gap opened up at high magnetic fields, resulting in an insulating state near the charge-neutrality point[14, 15]. There have been several experimental studies on this topic and so far there has not been an agreement. We explored the electronic states at $n = 0$ Landau level and tried to gave more evidence and well founded explanations.

Besides studying the electronic states at $n = 0$ Landau level, we are also interested in how the charge transport takes place in the quantum Hall regime. Similar to QHE in standard semiconductors, band bending creates pathways for charge carrier transport. Due to the fact that graphene is exposed to external environment, its electronic properties are affected dramatically by external charged impurities and substrate roughness. Thus, besides band bending, charge transport should be also affected by potential fluctuations caused by the

external imperfections, which will create an uneven local electric field across the device. If we direct a laser on graphene, the generated electron-hole pairs could be separated by the local electric field at the laser spot and transported across the device to reach the electrodes. Thus by measuring the photovoltage on the electrodes while scanning the position of the laser spot, we can gather information about local potential distribution. With this method, we explored the effect of external surface doping in graphene on charge transport through Landau levels in the quantum Hall regime.

In contrast to monolayer graphene, with its linear energy dispersion and zero band gap, bilayer graphene has a quadratic dispersion relation and also zero band gap, which has already been studied extensively[15, 16]. It is natural to think about what happens in trilayer graphene. With only one additional layer, it is actually much more complicated than bilayer graphene. Trilayer graphene has two different stacking orders (ABA and ABC), which will be explained in the next chapter, with two different electronic band structures. The electronic band structure of ABA-stacked trilayer graphene consists of superimposed monolayer and bilayer band structures[17, 18], which are linear and quadratic, respectively. And it has been already studied in experiments[19, 20]. On the other hand, the electronic band structure in ABC-stacked graphene has been predicted in theory to be a unique cubic dispersion which is different from both monolayer and bilayer graphene[18, 21–23]. To our best knowledge, there has not been any experimental study done on ABC-stacked graphene and we explored it in detail. Twelve- and four-fold degeneracy in $n = 0$ and $n > 0$ Landau levels, respectively, has been observed in our experiments.

## 1.4 Photovoltaic effect in semiconductors and its application in water splitting

Photovoltaic effect is the direct conversion of light into electricity at the atomic level. Some materials exhibit a property to absorb photons of light and generate electron-hole pairs. When these electron-hole pairs are well separated and collected before their recombination, in an open-circuit configuration, an electric voltage can be generated on the charge collection electrodes. If a resistive load is connected between the electrodes, a photocurrent is expected.

The photoelectric effect was first noted by a French physicist, Alexandre Edmond Becquerel, in 1839, who found that certain materials would produce small amounts of electric current when exposed to light[24, 25]. In 1905, Albert Einstein described the nature of light and the photoelectric effect on which photovoltaic technology is based, for which he won a Nobel prize in physics in 1921.

To generate the photovoltaic effect in a semiconductor, the photon energy needs to be greater than the energy band gap of the material, so that electrons can be excited from the valence band to the conduction band and then possibly collected by electrodes. This effect has a few applications. The first well known application is solar cell, which converts solar energy to electricity, and the first photovoltaic module was built by Bell Lab in 1954.

Another interesting application is found in a photocatalytic reaction, which happens when electron-hole pairs, created by incident light, generate free radicals able to undergo secondary reactions, such as splitting water molecule to hydrogen and oxygen. The minimum energy needed into separate $H_2O$ molecule to $H_2$ and $O_2$ is 1.23 eV. A photocatalyst needs to have its conduction band edge well above the hydrogen reduction level and the valence band edge well below the water oxidation level for an efficient production of hydrogen and oxygen from water. This is because the electrons and holes will migrate to the surface of the

semiconductor and need enough energy to reduce and oxidize the reactants adsorbed on the surface.

Theoretically, semiconductors satisfy the energy band structure requirement can be used for photocatalytic hydrogen production, however, there are other factors influencing hydrogen production efficiency. First, if the conduction-band electrons and valence-band holes recombine before they reach the surface, they will release energy in the form of unproductive heat or light and not participate in any catalytic reactions. Second, even if the hydrogen and oxygen are successfully generated, they can recombine quickly into water (backward reaction) and be unable to be collected separately. Third, generally the efficiency of catalytic reaction increases with increasing surface area of the catalyst, reaches a maximum and may stay constant or decrease with further increase in surface area, and the situation differs from system to system[26]. Additionally, the width of energy band gap is also a factor. Wide band-gap semiconductors, such as $TiO_2$ with a 3.2 eV band gap, can only absorb UV light for catalytic reaction. Since UV light only accounts for about 4% of the solar energy while the visible light contributes about 50%, reducing the band gap of photocatalyst can potentially capture larger portion of the solar energy.

ZnO, another wide band-gap semiconductor, has been proposed as a water-splitting photocatalyst, and it was found that by forming GaN/Zno solid solution, the band gap can be reduced to 2.2 eV[27], which is well in the visible light spectrum. However, the electronic properties of this material, such as charge carrier concentration and electrical mobility, are still not clear but are essential for understanding the catalytic behavior. We conducted electronic and optoelectronic transport measurements in the GaN/ZnO solid solution nanowire devices trying to address some of these questions.

9

## 1.5 Organization of the dissertation

This dissertation is organized in a logical order and focused on transport studies of graphene. In Chapter 2, the electronic structure of graphene will be introduced. The transport properties with and without the presence of magnetic field will be both covered in this chapter. An overview of suspended graphene will be introduced. In Chapter 3, the low-frequency noise study in graphene will be presented. A detailed device fabrication procedure will be included along with the experimental setup for low-frequency noise (1/f noise) measurement. 1/f noise has been studied in both on-substrate and suspended devices, and we have found a relation between noise parameters and device mobilities. In Chapter 4, magnetotransport studies of graphene at low temperatures will be presented. The metal insulator transition in monolayer graphene, and unconventional quantum Hall effect in ABC-stacked trilayer graphene will be discussed. Chapter 5 will cover photocurrent study on graphene FETs. A spatially resolved photocurrent study of graphene devices in magnetic field at low temperatures successfully demonstrated charge transport in the quantum Hall regime. In Chapter 6, the results of electronic and optoelectronic study of $(\mathrm{GaN})_{1-x}(\mathrm{ZnO})_x$ solid solution nanowires will be presented. Along with the device fabrication techniques, device mobility measured in electrical measurements and optical band gap measured with monochromator will be shown in this chapter. The work presented in this dissertation will be summarized in the final chapter, Chapter 7. In the appendix, experimental results from GaN/AlGaN high electron mobility transistors under hydrostatic pressure are presented. Those results are not conclusive and have not been published, so they are presented in appendix instead of a regular chapter.

# Chapter 2

# Synthesis and Electronic Properties of Graphene

## 2.1 Crystal structure of graphite

As shown in Fig.2.1, three-dimensional graphite is formed by loosely coupled layers of two-dimensional carbon atoms, which are ordered in hexagonal lattice. A single layer of two-dimensional carbon atoms is named graphene. The in-plane C-C bonds, with distance of 1.42Å, are formed by strong covalent interactions. On the other hand, the out-of-plane bonds between graphene layers is by van der Waals force, which is much weaker than the former force, with a layer-layer distance of 3.35Å.

The stacking order of graphene layers can be of two different types, which are Bernal (ABA) and rhombohedral (ABC), shown in Fig.2.1(a) and (b), respectively. Large single crystal Bernal graphite is rare in nature and when it appears it usually has high defect density. High quality Bernal graphite can be synthesized in the form of highly oriented pyrolytic graphite (HOPG), which is formed by cracking hydrocarbons at high temperature
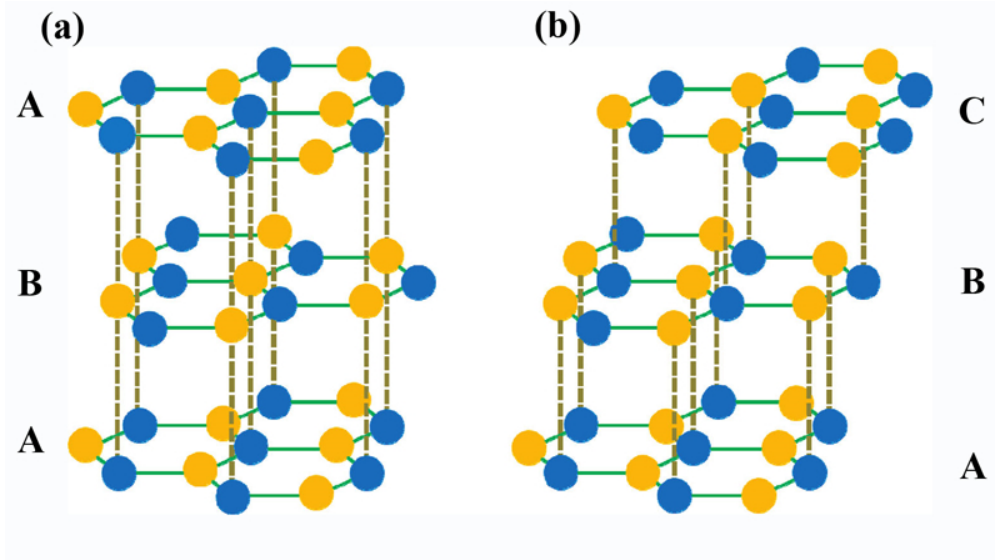
Figure 2.1: (a) ABA stack order. (b) ABC stack order.

and subsequently treating them with high pressure. The high purity of HOPG makes it a good material for graphene transistor fabrication. On the other hand, rhombohedral graphite can be obtained from kish graphite, which is a byproduct of steel manufacture.

## 2.2 Band structure of graphene

Graphite with different number of carbon layers has different electronic band structures. Here band structures of monolayer, bilayer and trilayer graphene will be discussed.

### 2.2.1 Energy dispersion in monolayer graphene

The simplest model to calculate band structure of graphene with reasonable results is the tight-binding method, in which only the nearest neighbor interaction is considered[28]. As shown in Fig. 2.2(a), there are two inequivalent carbon atoms, A and B, in a unit cell of
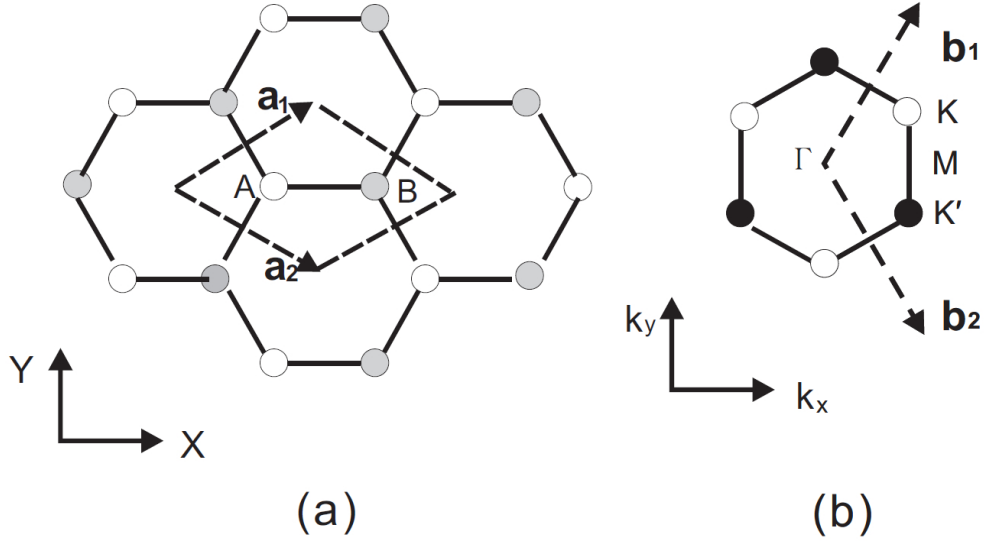
Figure 2.2: (a) Hexagonal crystal lattice in graphene, $a_1$ and $a_2$ are lattice vectors. (b) The first Brillouin zone in the reciprocal lattice.

graphene lattice. $a_1$ and $a_2$ are the lattice vectors, where $a$ is the lattice constant $a$=2.46Å.

$$a_1 = (\sqrt{3}a/2, a/2), a_2 = (\sqrt{3}a/2, -a/2) \tag{2.1}$$

As shown in Fig.2.2(b), the reciprocal lattice also has hexagonal symmetry. The primitive lattice vectors $b_1$ and $b_2$ are calculated with Eq.(2.2), and $a_3$ is the unit vector perpendicular to the graphene plane.

$$b_1 = 2\pi \frac{a_2 \times a_3}{a_1 \cdot (a_2 \times a_3)}, b_2 = 2\pi \frac{a_3 \times a_1}{a_1 \cdot (a_2 \times a_3)} \tag{2.2}$$

From nearest-neighbor tight-binding calculation, the energy dispersion is described by Eq.(2.3), where $\gamma = 3$ eV is the nearest-neighbor hopping energy[29]. And the relation is shown in Fig.2.3.
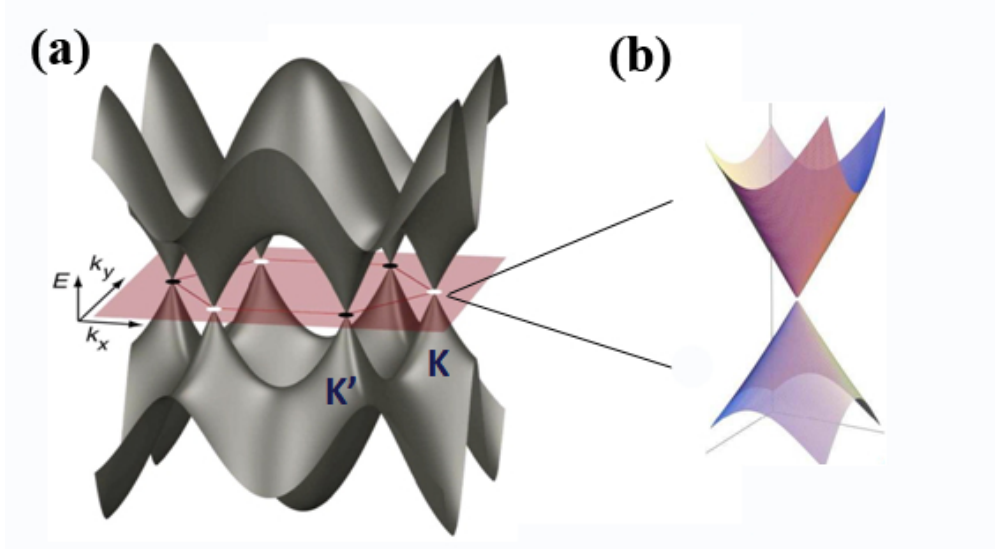
Figure 2.3: Electronic band structure of graphene from tight-binding calculation (a) The energy dependence on wavevector $k_x$ and $k_y$. (b) The low energy dispersion relation near Dirac point K.

$$E(k_x, k_y) = \pm\gamma\sqrt{1 + 4cos(\frac{\sqrt{3}k_x a}{2})cos(\frac{k_y a}{2}) + 4cos^2(\frac{k_y a}{2})} \tag{2.3}$$

Carbon atom has six electrons, and the ground state is in the configuration of $1s^2 2s^2 2p^2$. Four outer electrons $2s^2 2p^2$ are weakly bound and called valence electrons. In the crystalline phase, the valence electrons give rise to $2s, 2p_x, 2p_y$ and $2p_z$ orbitals which are important in forming covalent bonds in graphite[30]. Since energy difference between $2s$ and $2p$ levels is small compared to the binding energy of the chemical bonds, the electronic wave functions for these four electrons can mix with each other to enhance the binding energy of C–C bonds. As shown in Fig.2.4, the in-plane mixing of $2s, 2p_x$ and $2p_y$ orbitals form strongly coupled $\sigma$ bands, which is also known as $sp^2$ hybridization. The weakly coupled $2p_z$ orbital gives rise to two $\pi$ bands. The lower $\pi$ bonding band forms the valence band and the upper $\pi$ antibonding band forms the conduction band. The conduction band and valence band touch
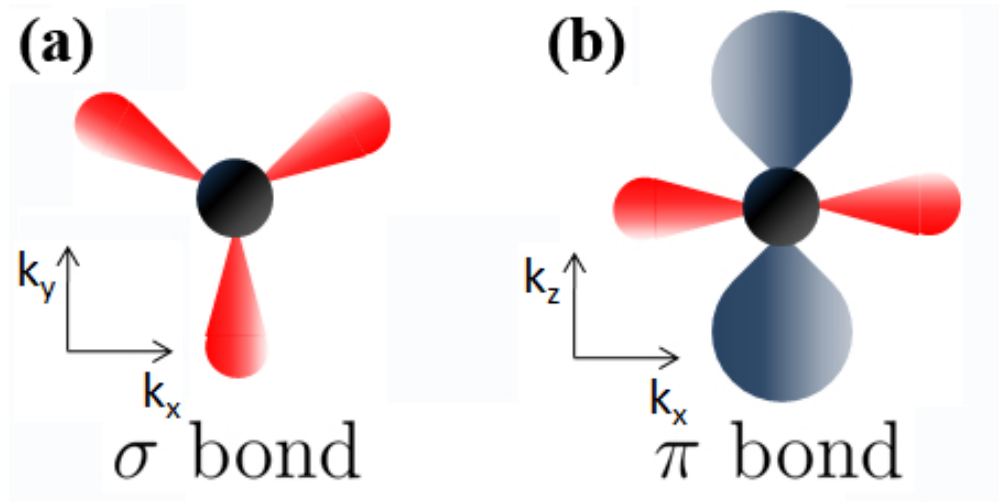
Figure 2.4: (a) In-plane $\sigma$ bonds. (b) Out-of-plane $\pi$ bonds.

precisely at two kinds of inequivalent corners (K, K') of the first Brillouin zone, which are called Dirac points, as shown in Fig.2.3(b). There are two kinds of Dirac points due to two inequivalent carbon atoms in each unit cell. And graphene is a zero band gap semiconductor and semimetal.

Charge carriers in graphene follow Dirac-Weyl equation for the Hamiltonian $H = \hbar v_F \cdot \vec{\sigma} \cdot \vec{k}$, where $v_F$ is the Fermi velocity and $\vec{\sigma}$ is the 2D Pauli matrix[31]. It leads to a linear energy dispersion (Fig.2.3(b)) as $E = \hbar v_F |k|$, which is similar to photon and implicates the charge carriers are massless, with $v_F \approx 1 \times 10^6 m/s$. The Dirac-Weyl equation also introduces an additional quantum number, $\sigma$, which is referred as pseudospin due to the equivalence of A and B sublattices in the graphene crystal lattice as shown in Fig.2.2. Pseudospin has two values, +1 and -1, similar to spin, thus the degeneracy is 2×2=4 in graphene.

### 2.2.2 Energy dispersion in few-layer graphene

The stacking order in few-layer graphene affects its band structure[17, 21, 29, 32–34]. It has been found that bilayer graphene is a zero band gap semiconductor (and semimetal) with a parabolic energy dispersion relation. When an electric field is applied perpendicular to the carbon-plane, the symmetry along the c-axis is broken and the two layers are no longer equivalent, thus an energy band gap between the conduction and valence band can be induced.

In trilayer graphene, ABA-stacked graphene (Fig.2.1(a)) is semimetallic with a small overlap between the conduction and valence bands, and external electric field does not induce a band gap in the ABA-stacked trilayer graphene. On the other hand, ABC-stacked trilayer graphene (Fig.2.1(b)) is a zero band gap semiconductor with a band contact near the K point on the KM symmetry line, and it opens up a band gap at the K point with an external electric field.

## 2.3 Minimum conductivity in graphene

Undoped intrinsic graphene, in which the carrier density is absolutely zero everywhere across the sample, was predicted to have a precise ballistic conductivity of $\sigma_D = 4e^2/(\pi h)$ using an effective field theory of Dirac fermions[35]. However, the experiments have shown sample dependent minimal conductivity $\sigma_m \approx 4e^2/h$ around the Dirac point[31]. The non-existence of universal minimal conductivity $\sigma_D$ clearly disagrees with the theoretical predictions. This discrepancy could be due to the theoretical approximations, localization, charge inhomogeneity, etc.[15, 31].

Charge inhomogeneity could come from charged impurity centers in the environment (known as electron-hole puddles), and ripples associated with the intrinsic structural wrinkles

or the substrate interface roughness[15]. At low charge carrier density or low gate voltage in field-effect transistors, the density fluctuations induced by the charge inhomogeneity become larger than the electric field induced average density, then the concept of homogeneous samples breaks down.

## 2.4 Suspended graphene

Most of the interesting physics happens in the low density regime or around the Dirac point, however, substrate-induced charge inhomogeneity due to substrate roughness and trapped charges in the oxide or at the graphene–oxide interface, will induce potential fluctuations near the Dirac point which makes the physics near Dirac point hardly accessible. Removing the dielectric layer under graphene helps to accesses the intrinsic electrical properties near the Dirac point. The topography of this suspended graphene sheet was studied with STM and TEM[36, 37], and TEM study showed that the suspended graphene sheet was not perfectly flat in the plane but with 1nm out-of-plane wiggles[36].

Making such suspended device was an important experimental milestone where $SiO_2$ dielectric layer underneath graphene was chemically etched away after exfoliating graphene and depositing electrical contacts[38, 39]. A cartoon and an SEM image of suspended graphene device are shown in Fig.2.5. Quite surprisingly, the just-made suspended graphene devices had no significant difference with the on-substrate devices on electrical mobilities near the Dirac point[39]. This suggested that impurities sticking to the graphene flake, other than the substrate, also limit the transport properties. Only after removing the impurities with annealing, such as temperature annealing by heating up the entire substrate or current annealing ($\sim$ few $mA/\mu m$ in width) by locally heating up the graphene sheet[39, 40], the suspended graphene devices showed dramatically higher mobilities. By lowering the temper-
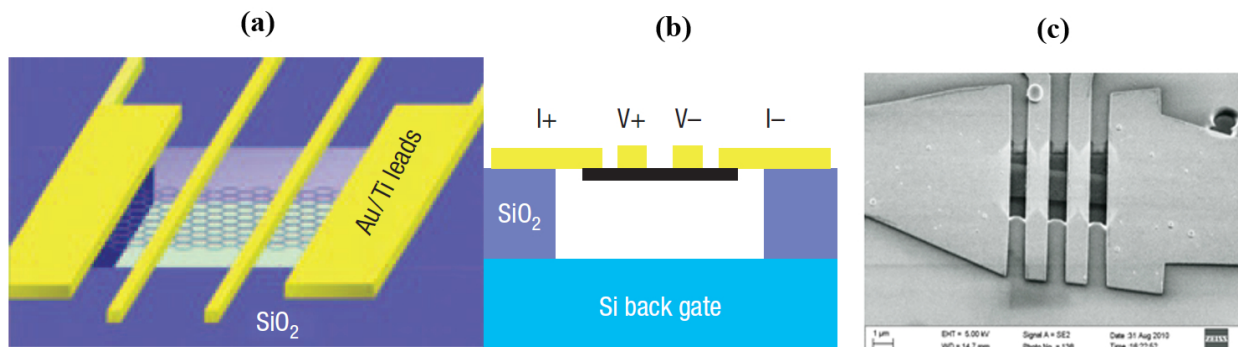
Figure 2.5: (a) Cartoon of top-view of suspended graphene device. (b) Side-view of suspended graphene device[38]. (c) SEM image of a real suspended graphene device

ature to decrease temperature excitations, carrier mobility of more than 200,000 $cm^2/V \cdot s$ has been achieved[38, 39]. One problem with suspended graphene is that only a small gate voltage ∼15-20 V can be applied due to the electrostatic attraction between the charges in the graphene sheet and the gate, which tends to collapse the graphene sheet from the top of the trench to the substrate. This is in clear contrast to on-substrate graphene where gate voltage can be as high as ∼100V.

## 2.5 Quantum Hall effect (QHE) in graphene

In typical graphene field-effect transistors (FETs), graphene flakes are mechanically exfoliated onto highly doped Si substrate with 300nm $SiO_2$ as dielectric layer in between. By sweeping the gate voltage $V_g$ from positive to negative values, the polarity of the charge carrier can be easily tuned from electron to hole, with a carrier density of $7.2 \times 10^{10} cm^2/V$ of $V_g$.

When applying a perpendicular magnetic field $B$ on the sample, two-dimensional electrons or holes confined in graphene are constrained to move in close cyclotron orbits that are

quantized in quantum mechanics. The quantization of the cyclotron orbits is reflected in the quantization of energy levels, which are called Landau levels (LL) at finite $B$. For any LL there are $N_\Phi = BA/\Phi_0$ orbital states, where $A$ is the area of the sample and $\Phi_0 = h/e$ is the magnetic quantum flux. Quantum Hall effects appear when $N_\Phi$ is comparable to the total number of quasiparticles in the sample[15]. In the quantum Hall regime, the Hall conductivity $\sigma_{xy}$ exhibits plateaus as a function of carrier density or magnetic field where it takes quantized values. Meanwhile, the longitudinal conductivity $\sigma_{xx}$ is minimum where the $\sigma_{xy}$ is at plateaus. When the magnetic field increases, the longitudinal conductivity $\sigma_{xx}$ oscillates as a function of $B$, a phenomenon known as Shubnikov-de Haas oscillations (SdHOs). In traditional two-dimensional electron gas (2DEG), the LLs have energies of $\hbar\omega_c(n + 1/2)$, where $n = 0, 1, 2, \cdots$ and cyclotron frequency $\omega_c = eB/m^*$ with $m^*$ being the effective mass. The case in graphite has to be considered separately for different number of carbon layers.

### 2.5.1 Quantum Hall effect in monolayer graphene

The low energy fermions (electrons and holes) in graphene are massless which would give rise to an infinite $\omega_c$, thus the results in standard 2DEG cannot be applied to graphene. The 2D Dirac equation was applied to find out the LL in the presence of a magnetic field, and the result is shown in Eq.(2.4) [41]. An unconventional QHE was found for $\sigma_{xy}$ as shown in Eq.(2.5), where $g$ is the degeneracy, and illustrated in Fig.2.6(b).

$$E_n = sgn(n)v_F\sqrt{2e\hbar B|n|}, \ with \ n = 0, \pm 1, \pm 2, \cdots \qquad (2.4)$$

$$\sigma_{xy} = g(n + \frac{1}{2})\frac{e^2}{h} \qquad (2.5)$$

As shown in Fig.2.6(a), the integer QHE in standard 2DEG has a form of $\sigma_{xy} = gn\frac{e^2}{h}$,
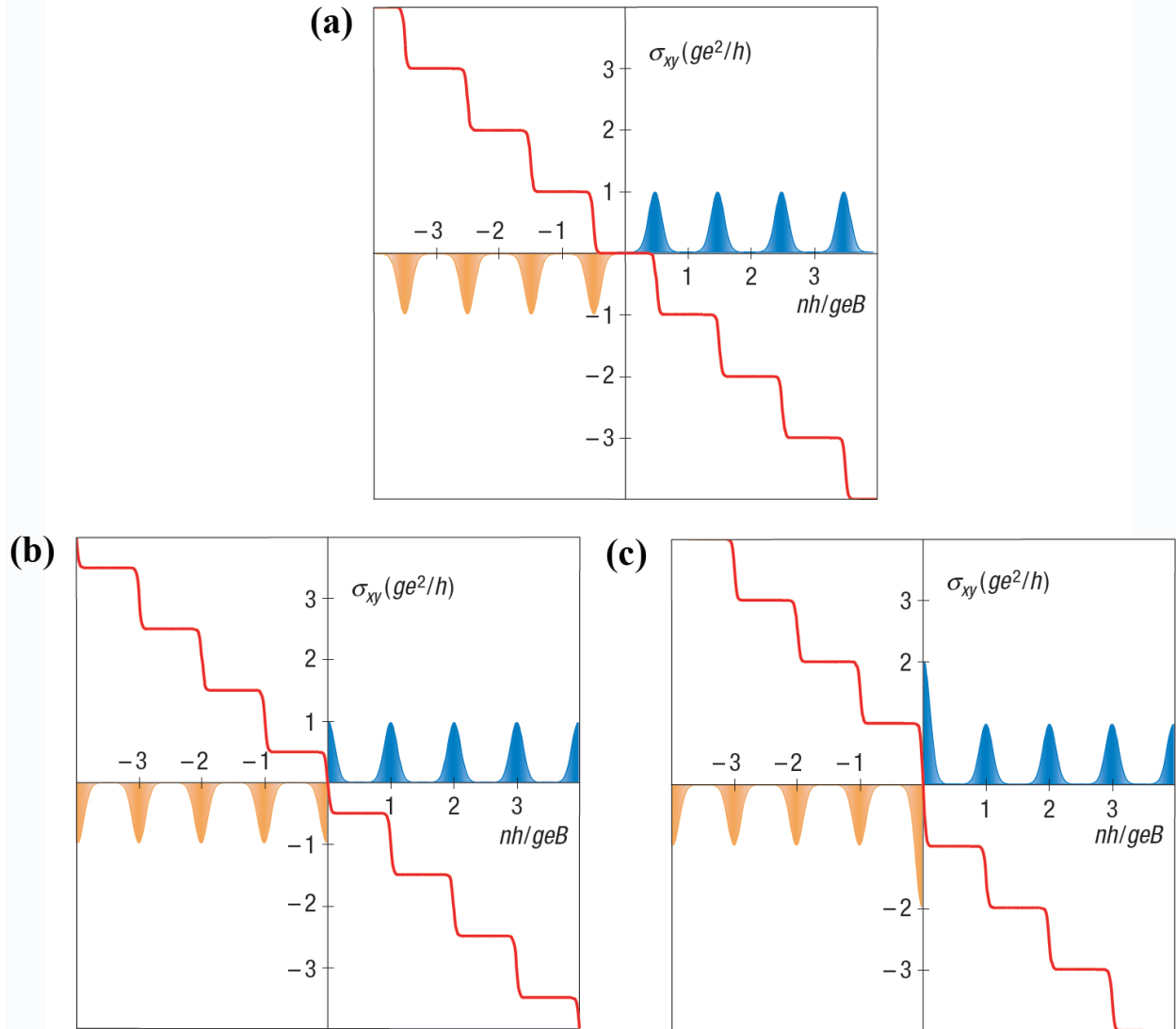
Figure 2.6: Integer quantum Hall effect. (a) Illustration of conventional integer QHE in standard 2DEG. (b) Unconventional integer QHE of massless Dirac fermions in monolayer graphene. (c) Unconventional integer QHE of massive fermions in bilayer graphene. Adapted from Novoselov *et al.*[16]

which is quite different from the QHE in monolayer graphene. In graphene, due to the spin and valley degeneracy, $g$ in Equa. 2.4 has $g = 4$, as discussed in Sec.2.2.1. The factor $1/2$ in Eq.(2.5) is due to the chiral nature of the quasiparticles in graphene, and can be understood as a term induced by the additional Berry phase ($\pi$) that the electron needs to complete a close orbit, due to their chiral nature[42]. The QHE in monolayer graphene was experimentally observed by Novoselov $et$ $al.$[11] and Zhang $et$ $al.$[43], and they agreed quite well with the calculations. The results from Zhang $et$ $al.$[43] are shown in Fig.2.7, with quantum Hall states well developed at $\nu = 2, 6, 10, \cdots$, where $\nu = n_s h/(Be)$ is the filling factor.

## 2.5.2  Quantum Hall effect in bilayer graphene

Similar to monolayer graphene, bilayer graphene also has four-fold degeneracy, however, there are a lot of differences between them. Unlike in monolayer graphene, carriers in bilayer graphene are massive Dirac fermions. The band structure is parabolic near the Dirac point[29, 33], and it is shown in Fig.2.8(a). The parabolic structure might suggest similar QHE as in standard 2DEG, however, there are two important differences: the bandgap in bilayer graphene is zero in the absence of external electric field, and the fermions are also chiral, similar to monolayer graphene but with a Berry's phase of $2\pi$ instead of $\pi$[44]. An external electric field on bilayer graphene can induce a bandgap between the conduction and valence bands[45], making it an interesting semiconductor with tunable bandgap (Fig.2.8(b)).

Similar to monolayer graphene, LLs in bilayer graphene are also four-fold degenerate, thus the Hall conductivity follows $\sigma_{xy} = 4n\frac{e^2}{h}$, where $n = \pm1, \pm2, \cdots$[16], noting that the $n = 0$ level is missing. The origin of this could be understood from the coupling between the two graphene layers where A, B sublattices in these two layers are not equivalent, which is
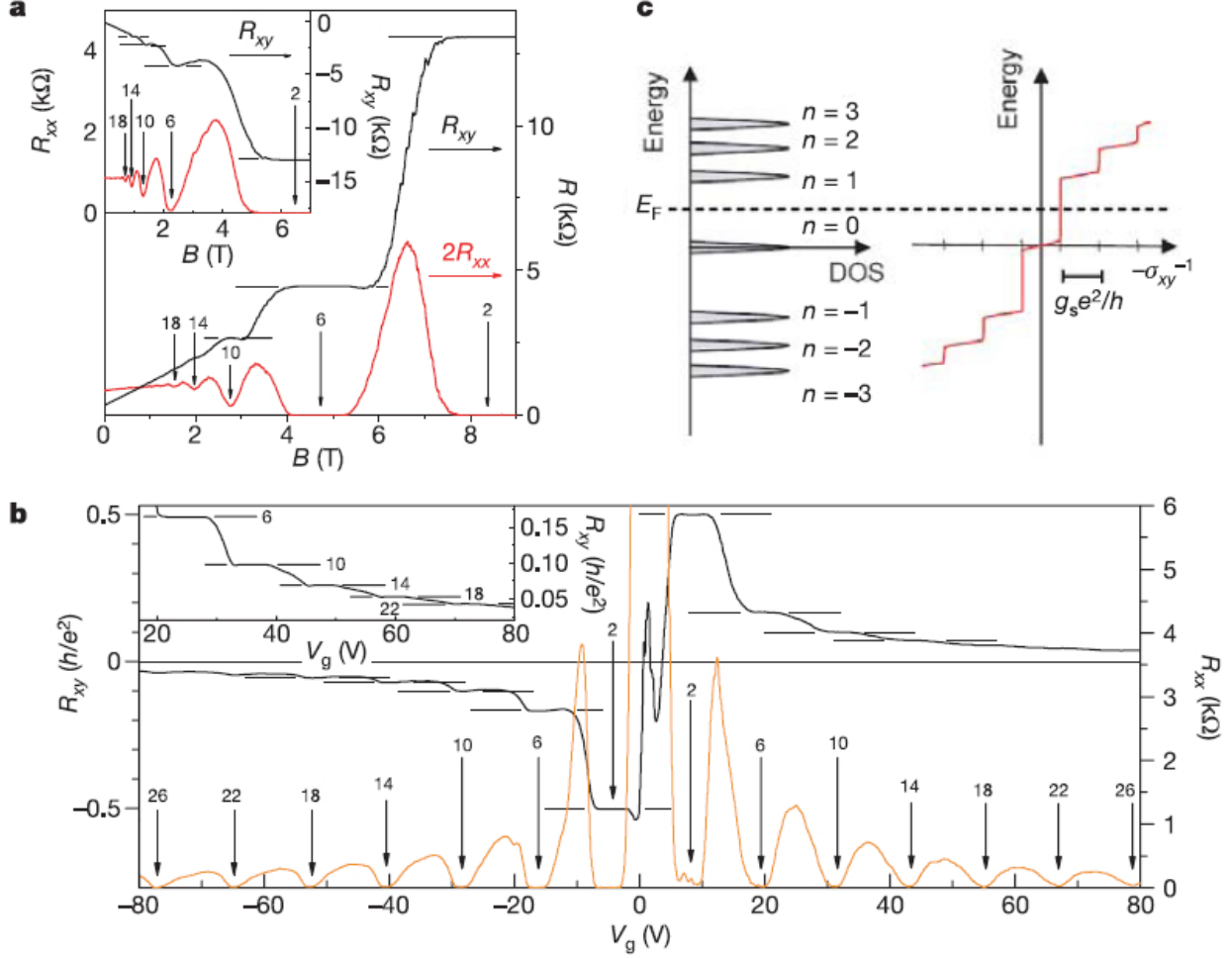
Figure 2.7: Quantized magnetoresistance $R_{xx}$ and Hall resistance $R_{xy}$ in a monolayer graphene FET. (a) $R_{xy}$ (black)and $R_{xx}$ (red) measured with $V_g$=15V, $T$=30mK. The vertical arrows indicate the quantum Hall states and the corresponding filling factor $\nu$. The inset shows the QHE with $V_g$=-4V, $T$=1.6K. (b) $R_{xy}$ (black)and $R_{xx}$ (orange) measured as a function of $V_g$ with fixed $B$=9T, $T$=1.6K. The inset shows a detailed view of high-filling-factor plateaux measured at 30mK. (c) Schematic diagram of LL density of states (DOS) and corresponding quantum Hall conductance ($\sigma_{xy}$) as a function of energy. Adapted from Zhang *et al.*[43]
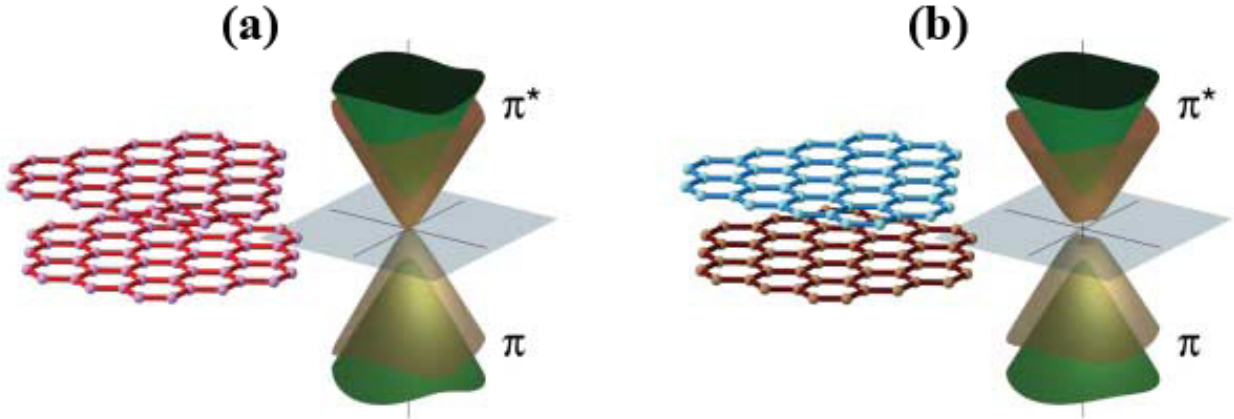
Figure 2.8: Electronic band structure of bilayer graphene.[46] (a) Band structure without electric field. (b) Band structure with electric field which opens up a bandgap.

different from monolayer graphene. The parabolic energy dispersion follows $E = \hbar^2 k^2 / 2m$, where the effective mass $m = 0.05 m_e$[16]. The quantized energy levels in magnetic field follow $E_n \approx \pm \hbar \omega_c \sqrt{n(n-1)}$[44]. Apparently energy levels with $n = 0$ and $n = 1$ are degenerate. Taking the four-fold degeneracy from spin and valley into account, the overall $2 \times 4e^2/h$ step is formed near the zero-energy region in bilayer graphene, and the diagram is shown in Fig.2.6(c). Experimentally, the QHE in bilayer graphene was observed by Novoselov *et al.* (2006)[16], which agreed well with theory.

## 2.6 Device fabrication

Generally, the graphene devices were first exfoliated with scotch-tape onto $SiO_2$/Si substrate and processed with e-beam lithography and metal deposition.
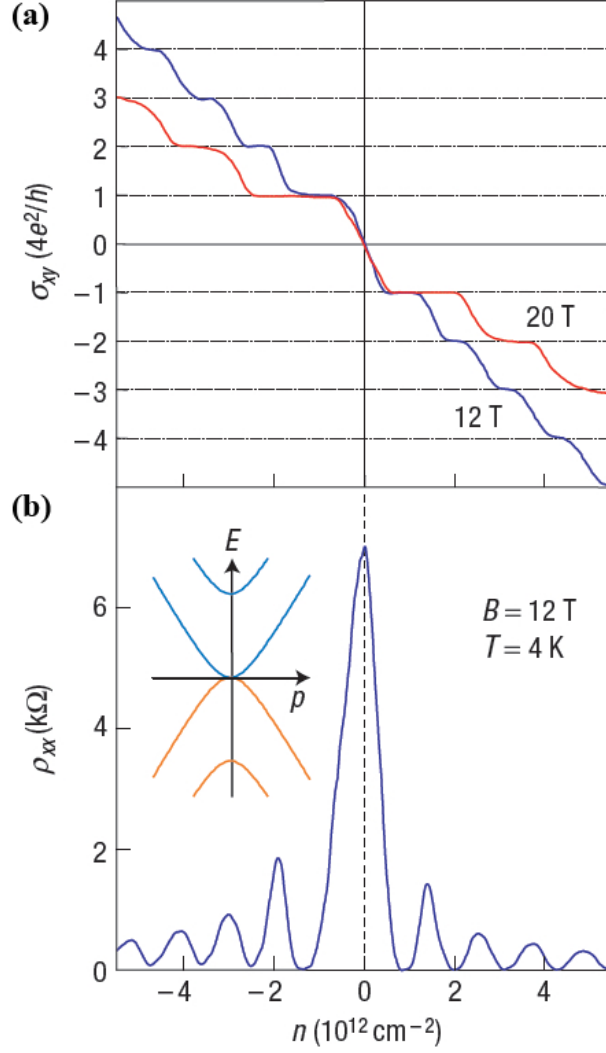
Figure 2.9: Quantum Hall effect in bilayer graphene. (a) Hall conductivity $\sigma_{xy}$ as a function of charge density n at fixed $B = 12, 20T$ and temperature $T = 4K$. $\sigma_{xy} = \rho_{xy}/(\rho_{xx}^2 + \rho_{xy}^2)$ was calculated from experimental results of $\rho_{xx}$ and $\rho_{xy}$. (b) Magnetoresistivity $\rho_{xx}$ as a function of carrier density. The inset shows the calculated energy dispersion for bilayer graphene, which is parabolic near Dirac point. Adapted from Novoselov *et al.*[16]
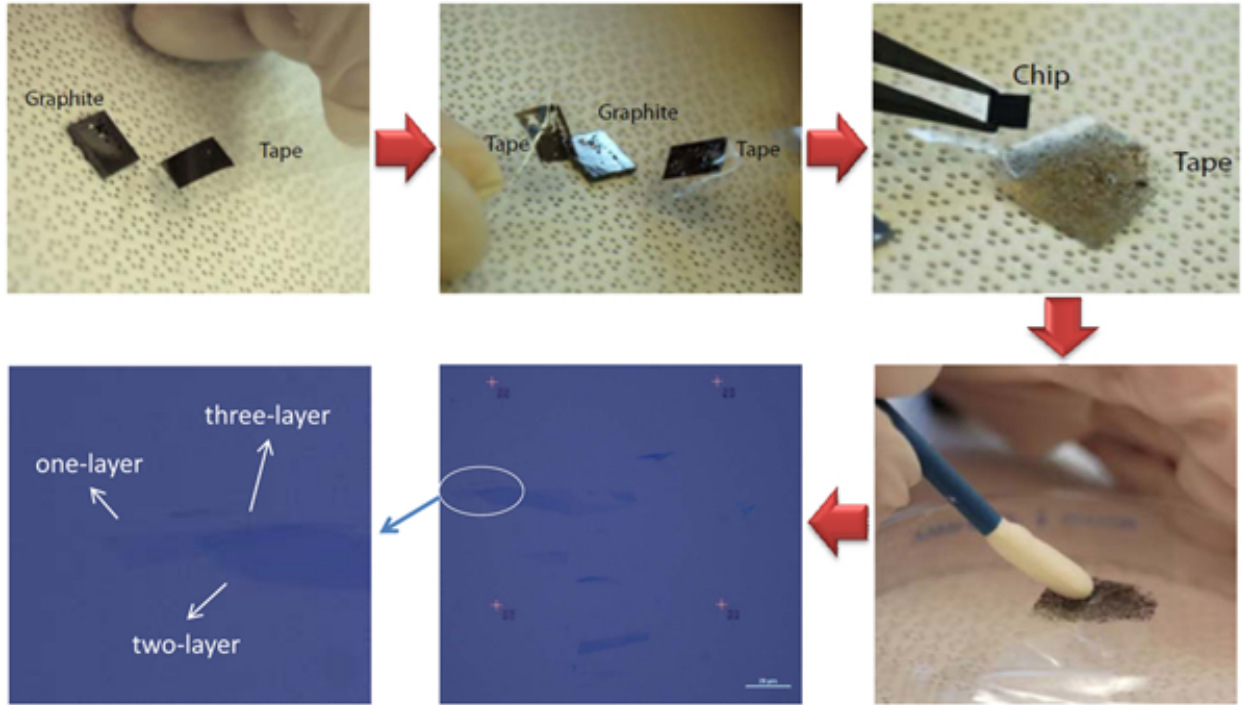
Figure 2.10: Procedures of graphene exfoliation. First four pictures are adapted from Williams's thesis[47].

## 2.6.1 Graphene exfoliation

We selected highly p-doped ($B$ doped) Si wafer with characteristics of $< 100 >$ orientation, 0.001-0.002 $\Omega \cdot cm$ resistivity, 500-550 $\mu m$ thick prime grade Si with one side polished, and it has chlorinated dry-thermal oxide on both sides with a thickness of 2850 Å±5%. The wafer is cut to 1×1 $cm^2$ pieces and cleaned with sonication through acetone, isopropanol and DI water. The the small pieces of substrate are baked on hot plate at 120°C for a few minutes to remove absorbed moisture.

After wafer cleaning, the graphene is exfoliated on top of substrate. Highly oriented pyrolytic graphite (HOPG) was used in most of the projects in this dissertation, along with kish graphite used in trilayer graphene QHE. As shown in Fig. 2.10, a thick layer of graphite
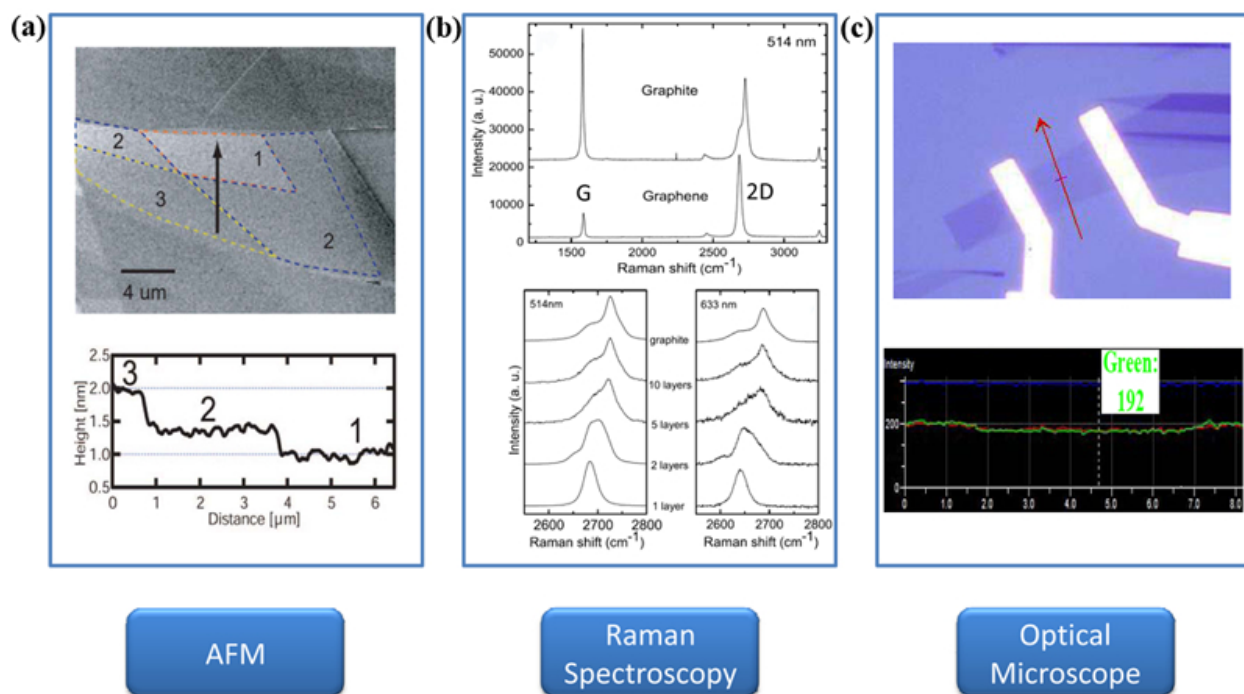
Figure 2.11: Methods to measure number of graphene layers. (a) Atomic force microscope. Adapted from Lin *et al.*[48]. (b) Raman spectroscopy. Adapted from Ferrari *et al.*[49]. (c) Optical microscope intensity profile.

is peeled off with scotch tape from a piece of HOPG, and then the thick graphite is thinned down with more tapes. Until an optimum thickness on tape, which is based on experience, that is thin enough to produce monolayer graphene but thick enough for moderate yield. The final tape is pressed onto Si substrate, and removed later. Then the substrate is examined under optical microscope for locations of graphene. As shown in Fig. 2.10, darker color of graphite correspond to thicker layers.

There are three typical methods to measure the number of graphene layers. As shown in Fig. 2.11(a), with atomic force microscope (AFM), each carbon layer corresponds to $\sim 0.5$ nm step. Besides AFM, Raman spectroscopy can also get the number of layers reliably[49]. As shown in Fig. 2.11(b), with 514nm laser, the Raman spectrum of graphene has a 2D
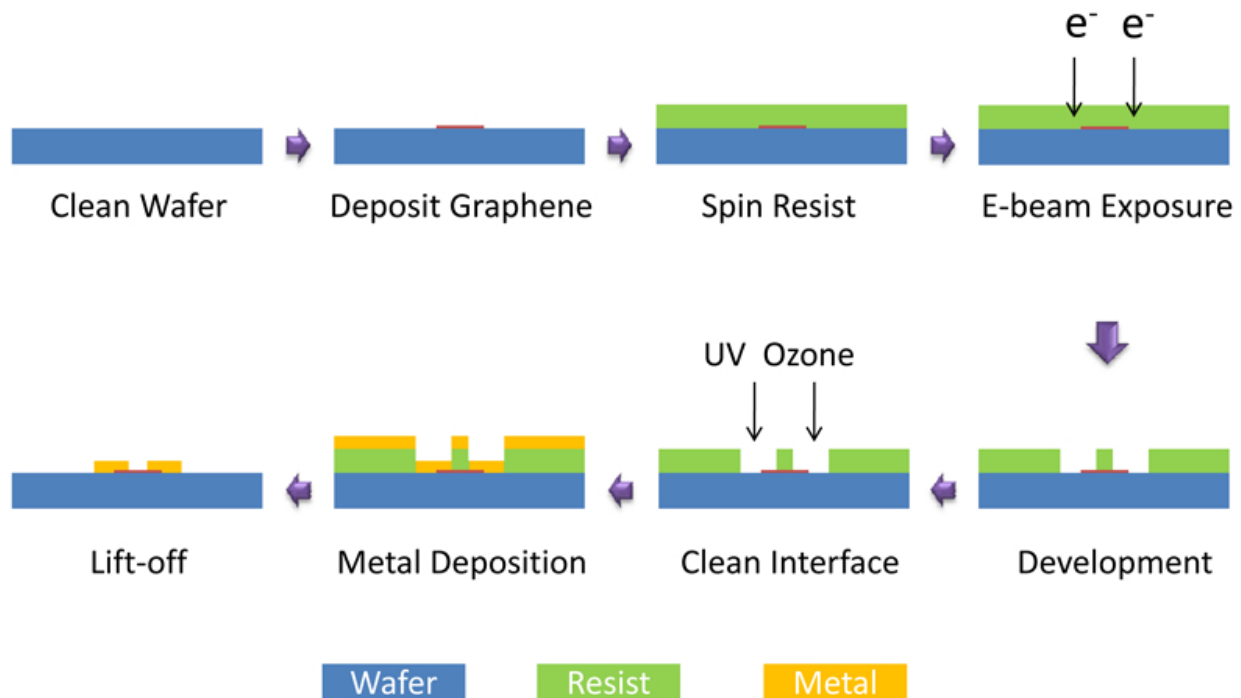
Figure 2.12: Diagram of device fabrication procedure.

peak $\sim 2680 cm^{-1}$, and the peak shifts toward large numbers for thicker layers; the actual Raman shift is a reliable parameter to mark the number of graphene layers. There is an even easier way, using optical microscope, as shown in Fig. 2.11(c). After taking the optical intensity profile with a CCD (green light is more sensitive than red and blue light), monolayer graphene will show 4% lower reflective intensity than the $SiO_2$, whereas bilayer and trilayer graphene will exhibit reductions of $\sim 8\%$ and $\sim 12\%$, respectively.

## 2.6.2   E-beam lithography and metal deposition

As shown in Fig. 2.12, after depositing graphene on a substrate, e-beam resist PMMA(950 C4) is spun on top at 5000rpm for 45 seconds, which will create $\sim$300nm thickness. Then the optical image of graphene is taken as a reference to design the e-beam pattern with

DesignCAD (or AutoCAD). E-beam patterning is done with a FEI Helio e-beam/ion-beam dual beam system at the Center for Functional Nanomaterials (CFN) in Brookhaven National Laborotary (BNL). The electron exposure dose is typically $285\mu C/cm^2$ with 20keV beam energy. Then the sample is developed in MIBK/IPA 1:3 for 30 seconds followed by 30 seconds cleaning with pure isopropyl alcohol (IPA). After the pattern is developed, the device is placed in UV ozone for two minutes before metal deposition. UV ozone is very effective at cleaning organic residues and gives cleaner graphene interface for better metal contacts. Metal deposition of Cr/Au (3/35nm) is typically done with a Kurt J. Lesker PVD 75 vacuum electron beam deposition system. Then the sample is immersed in hot acetone ($\sim 70°$C) for one hour and cleaned with IPA and deionized water afterwards.

### 2.6.3 Suspended graphene device fabrication

Suspended graphene devices are fabricated from standard on-substrate devices (Fig.2.13 (a)). E-beam resist PMMA(950 C4) is spun on top of a standard on-substrate graphene device at 5000rpm for 45 seconds. As shown in Fig.2.13 (b), one step of lithography is used to open a window in PMMA right on top of the device, so that wet etcher can etch the $SiO_2$ underneath the graphene flake through the window and $SiO_2$ in other parts of the substrate are protected by PMMA. The device with PMMA window is immersed in buffered oxide etch (BOE) 7:1, in which the active reactant is hydrofluoric acid, for five minutes to completely remove the $SiO_2$ under the graphene flake, as shown in Fig.2.13 (c) cartoon. After wet-etching, the device is transferred to large amount of deionized water to completely remove the BOE, then it is transferred to hot acetone to completely remove the PMMA. Finally, the device is transferred to hot isopropanol and taken out directly from the liquid with device's substrate along vertical direction so that isopropanol on top of graphene flake evaporates
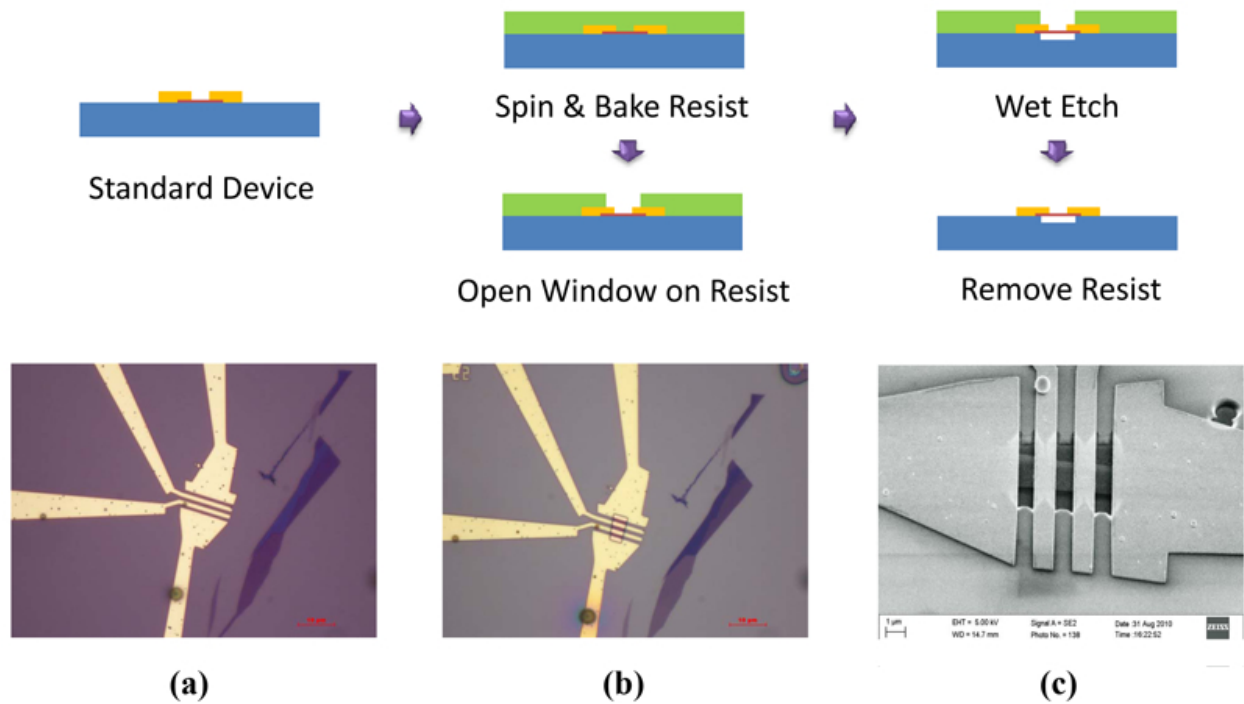
Figure 2.13: Diagram and images of suspended graphene device fabrication procedure. (a) A standard device. (b) PMMA spun on top of the substrate with a window opened on top of graphene flake though e-beam lithography. (c) Wet etching the device as prepared in (b), followed by PMMA removal and an SEM image of a fabricated suspended graphene device.

quickly[38]. Starting from the step of BOE etching, the device is kept in liquid all the time during transferring until it is taken out from hot isopropanol. If device is taken out from liquid in any step, the graphene flake will be easily broken by liquid surface tension. An SEM image of a typical suspended graphene device with four metal contacts is shown in Fig.2.13 (c).

# Chapter 3

# Low-Frequency Noise in Graphene

## 3.1 Introduction

Inherent noise, especially low-frequency noise poses a practical limit on how small an input signal can be in broadband circuits. Understanding low-frequency noise in graphene devices is a key step to increase the signal-to-noise ratio and improve the performance of circuits based on them.

Thus far, several groups have reported studies on the behavior of low-frequency noise in monolayer and few-layer graphene field-effect transistors (FETs)[48, 50–56]. It has been generally observed that the low-frequency noise power in graphene FETs follows a 1/f frequency dependence, and that noise is lower in suspended graphene than in on-substrate graphene[55]. However, the gate-voltage (or, equivalently, the charge carrier density) dependence has exhibited a variety of behaviors. In monolayer graphene nanoribbons with device width of ∼30nm, the low-frequency noise power density $S_V$ was found to be inversely proportional to the number of charged carriers, following Hooge's empirical relation[48, 57],

$$S_V(f) = \frac{\alpha_H V^{2+\beta}}{N f^\gamma} = A \frac{V^{2+\beta}}{f^\gamma} \qquad (3.1)$$

where $\beta \sim 0$, $\gamma \sim 1$, and $V$ and $N$ are the source-to-drain voltage and the total number of charge carriers in the conducting channel, respectively. $A$ is usually called the *noise amplitude* and $\alpha_H$ the *Hooge parameter*. $A$ depends on the the area of the sample whereas $\alpha_H$ is an intensity parameter.

In devices with widths larger than 500nm, however, the gate-voltage dependence of noise does not follow Hooge's relation but is rather complicated[52, 53]. In the vicinity of the charge neutrality voltage (Dirac point), at which the number of carriers is lowest (zero, ideally), noise is at a minimum, contrary to Hooge's relation. With the gate voltage, $V_g$, increasingly away from the Dirac point, the noise increases until it reaches a maximum at a sample-dependent gate voltage, beyond which the noise starts to decrease. When both gate voltage polarities are considered, graphically, the noise dependence on $V_g$ displays an M-like shape. A simpler, V-shaped dependence, (which does not follow Hooge's relation, either) has been found in bilayer and multi-layer graphene samples[50].

To account for these observations, several models have been proposed. For example, in a liquid-based field-effect device the observed M-shaped dependence was explained in terms of a charge noise model, by which, at low carrier density, noise was dominated by random charge fluctuations close to the graphene layer, and at high density, by carrier scattering in the graphene layer[52]. The model also explained why the noise maxima occurred when the normalized transconductance, $(dI_d/dV_g)/I_d$, was the largest. On the other hand, in an in-vacuum FET device, the observed increase of noise with increasing carrier density was attributed to the decrease of minority charge carriers induced by charge impurities (spatial-charge inhomogeneity model)[53].

Furthermore, 1/f noise has been studied in a large number of devices exposed to air for extended periods of time (more than a month). The observed increase of noise with time was attributed to decreased mobility and increased contact resistance[56]. Overall, there has been no consensus on an unified relationship that can account for the diverse behavior of 1/f noise in graphene devices.

We conducted comparative study of the low-frequency noise (henceforth denoted simply as noise) in suspended and on-substrate graphene devices. Our results are interpreted in terms of a modified Hooge model that also explains those from previous reports in the literature. In our model, the Hooge parameter, $\alpha_H$ , is not constant but variable. We have found that $\alpha_H$ is affected by: a) scattering of the charge carriers, which contributes to a universal (i.e. sample independent) dependence of $\alpha_H$, on device mobility; and b) the dynamics of the scattering, such as trapping-detrapping, which, although makes a sample- and temperature-dependent contribution to $\alpha_H$, does not have direct manifestation in the DC transport characteristics. It follows the model that the Hooge parameter would be reduced by reducing charge trapping and the number of scattering centers[38, 58], consistent with our observation of reduced noise in suspended graphene.

## 3.2   Instrument setup

Since noise is usually a very small quantity compared to the signal, it typically needs to be pre-amplified before going into the measurement equipment. As shown in Fig. 3.1, graphene FET is biased with a current source on drain-source leads and controlled by the gate voltage source. The drain-source voltage ($V_d$) is pre-amplified with a Stanford Research Systems SIM910 amplifier with a gain of 100, and the output from SIM910 is fed into a multimeter (Keithley 196) and a spectrum analyzer (Stanford Research Systems SR770) in parallel. The
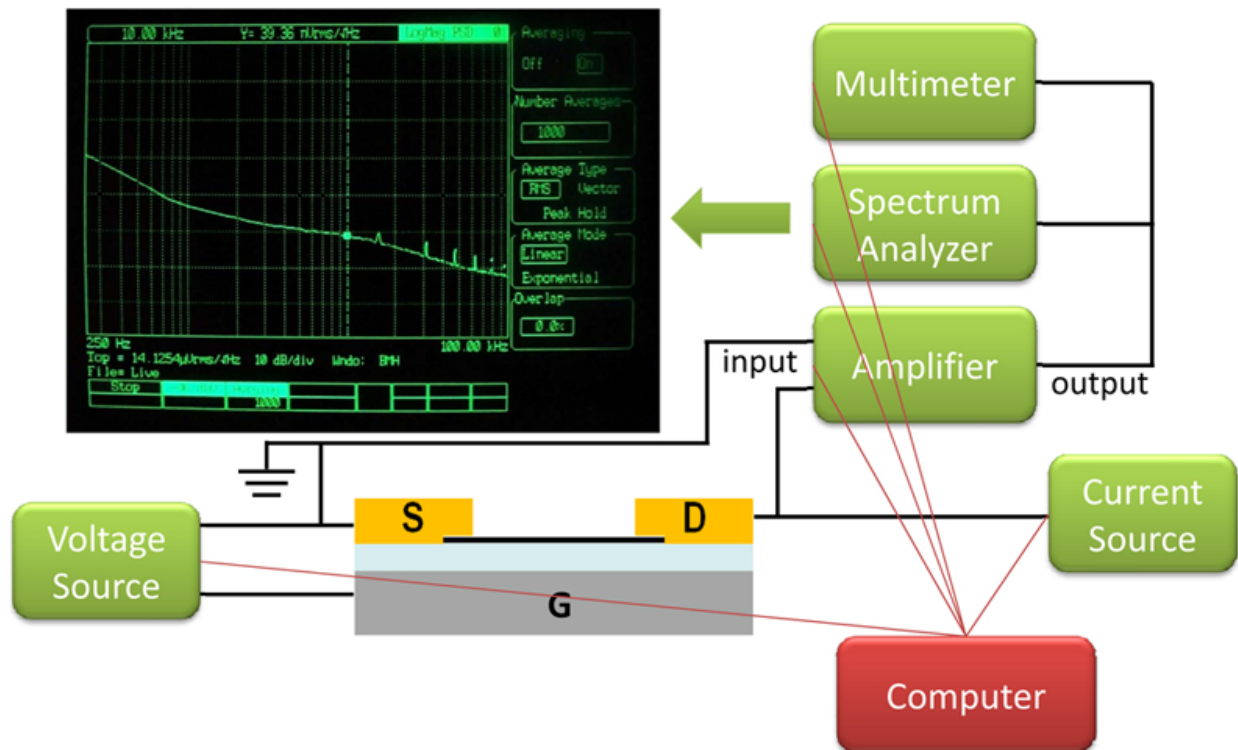
Figure 3.1: Diagram of DC voltage and noise measurement setup.

multimeter takes DC $V_d$ and the spectrum analyzer does fast Fourier transformation to the time-domain signal and transform it to the frequency domain and calculate the fluctuations' amplitude. All these instruments are controlled by a computer with LabVIEW programming to take and analyze data automatically.

## 3.3    Results of resistivity and noise measurements

In total, we measured the noise characteristics as a function of gate voltage in six on-substrate, or non-suspended graphene devices (NSG) and five suspended devices (SG) (The geometries of the samples are listed in Table 3.1). In all cases, we found that, through-
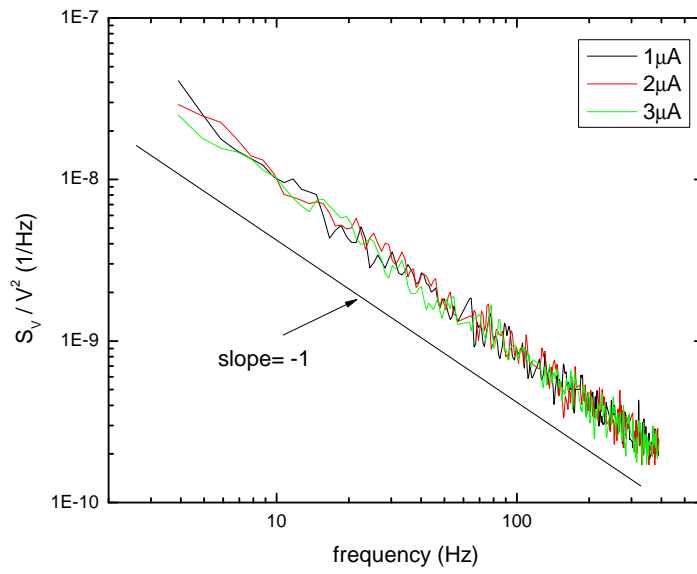
Figure 3.2: Normalized noise spectra for NSG5 at different drain current $I_d$, with $V_g$=0V. The solid line indicates the slope of 1/f dependence.
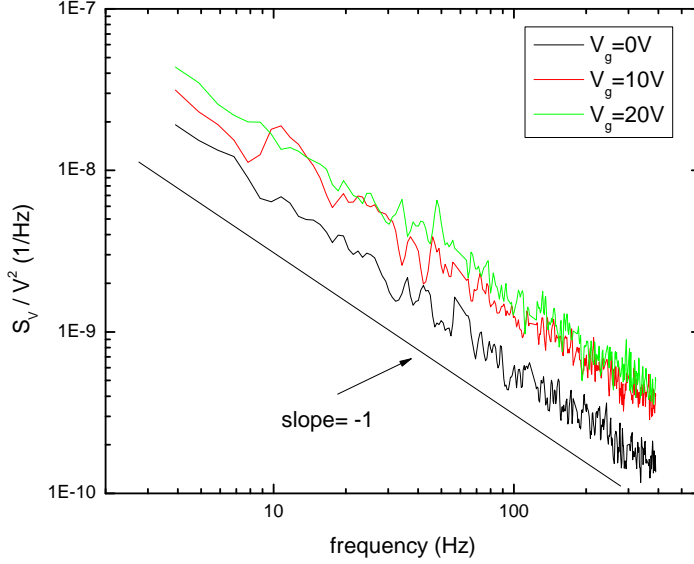
Figure 3.3: Normalized noise spectra for NSG5 at gate voltage of 0, 10, 20V, with $I_d$=1$\mu A$. The solid line indicates the slope of 1/f dependence.

out the temperature range of this work, the normalized voltage noise $S_V/V^2$ was independent of the external drain current (Fig.3.2), indicating that the noise was due to resistance fluctuations[58]. The normalized noise spectra with drain current $I_d$=1$\mu A$ at $V_g = 0, 10, 20V$ are shown in Fig.3.3, indicating gate dependent noise strength.

The observed normalized voltage noise, $S_V(f)/V^2$ generally followed the $1/f$ dependence of the Hooge's relation[57] (Eq.3.1). The noise power parameter, $\gamma$, was found to be $\gamma = 1.0\pm0.1$. The noise amplitude, $A$, was determined from a fit of the experimental $f \times S_V(f)/V^2$ data to Eq.3.1, which is frequency independent, since $S_V(f)/V^2$ depends on $1/f$. Figs. 3.4 and 3.5 show the gate-voltage dependence of the resistivity and the noise amplitude at room temperature for a typical on-substrate graphene device (NSG5) and a suspended graphene device (SG5), respectively. The charge carrier densities are proportional to $V_g$,
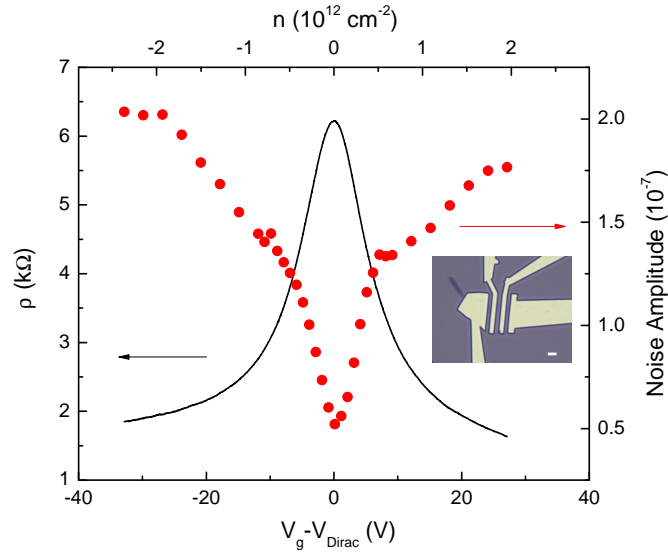
Figure 3.4: Resistivity and noise amplitude measurements in single-layer NSG5 device at room temperature. Inset shows typical optical image and the scale bar is 1 $\mu$m.
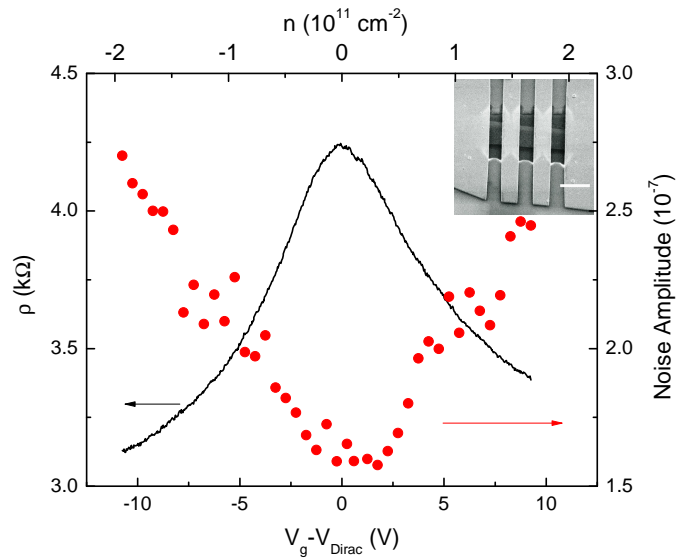


Figure 3.5: Resistivity and noise amplitude measurements in single-layer SG5 device at room temperature. Inset shows a typical SEM image and the scale bar is 2 $\mu$m.
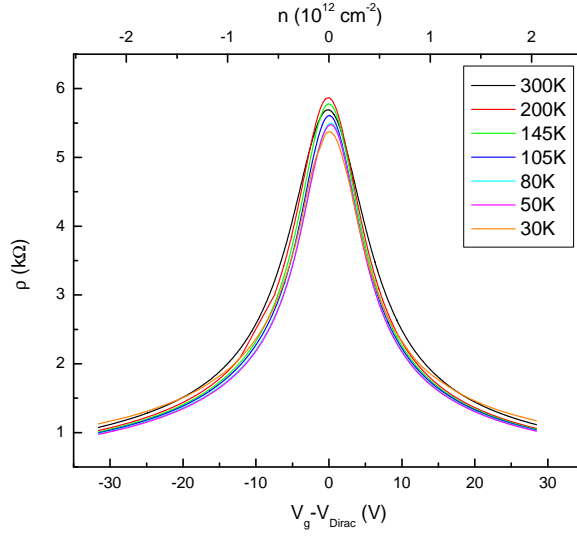
Figure 3.6: Temperature dependent resistivity measurements of NSG1 in temperature range of 30-300K.

with proportionality constants of $7.2 \times 10^{10}/cm^{-2} \cdot V$ and $1.8 \times 10^{10}/cm^{-2} \cdot V$, for NSG5 and SG5, respectively. As seen in Figs.3.4 and 3.5, in both samples the noise amplitude $A$ increases monotonically with increasing carrier density. The observed V-like shapes are contrary to what Hooge's relation (Eq.3.1) predicts, but are quite similar to the dependence found by others in bilayer and multi-layer graphene samples[50]. In other samples, such as NSG1 (see Fig.3.7), we observed an M-shaped dependence where noise amplitude increases with increasing $V_g$ near the charge neutrality point but then follows an opposite trend at higher $V_g$, analogous to recent results in single layer graphene and liquid-gated graphene transistors[52, 53].

Next we turn to the temperature dependence of the devices' resistance and noise characteristics. Fig.3.6 shows the resistivity versus gate voltage in an on-substrate device (NSG1) from T = 300K to 30K. The change of the resistance with temperature is quite small, especially away from the Dirac point. This is not surprising, since for graphene-on-SiO$_2$ devices
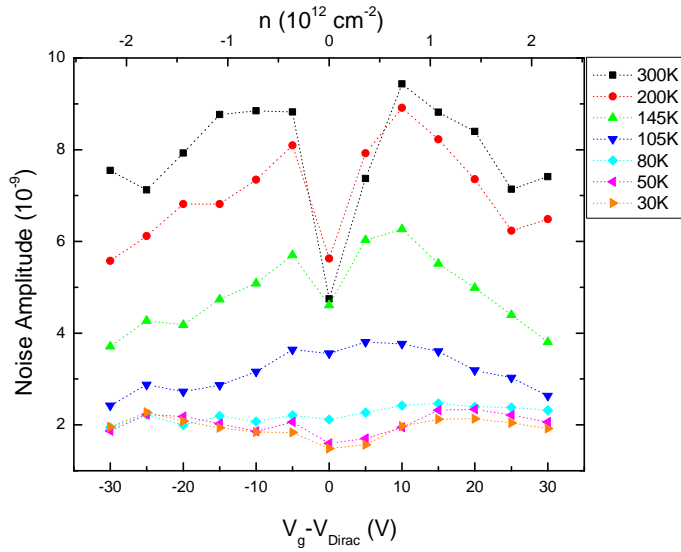
Figure 3.7: Noise amplitude dependence on gate voltage of NSG1 in temperature range of 30-300K.
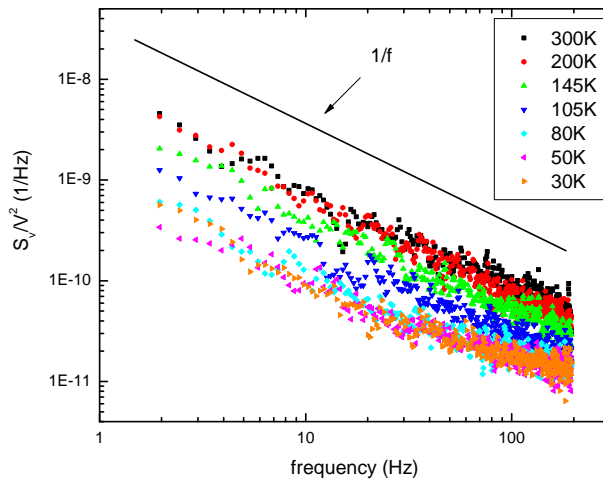


Figure 3.8: Normalized noise vs. frequency for NSG1 at temperatures from 30 to 300K, with $V_g$=-10V. The solid line indicates the slope of 1/f.
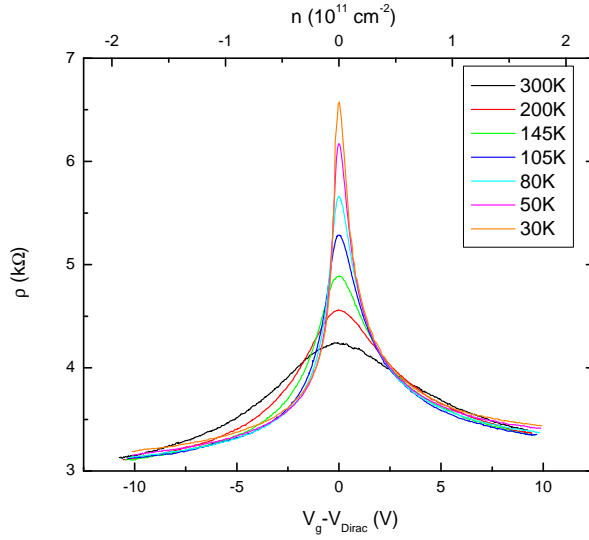
Figure 3.9: Temperature dependent resistivity measurements of SG5 in temperature range of 30-300K.

the mobility is mainly governed by temperature-independent charged-impurity scattering. In sharp contrast, the temperature dependence of noise is very strong, as seen in Fig.3.7, where we can appreciate an M-shape behavior especially pronounced at room temperature. (NSG1 has an area ∼35 times larger than NSG5.) The noise amplitude decreased monotonically with decreasing temperature, up to a factor of about 4 between 300K and 30K, a range in which the noise spectrum was linear with $1/f$. Around 30K, a deviation from linearity was observed, perhaps due to the onset of random telegraph noise (Fig.3.8), which is outside the scope of this work. The very different dependence on temperature of the resistance and the noise highlights the sensitivity of the latter to microscopic processes to which the resistance is almost immune.

Similarly, we have studied the temperature dependence of the noise amplitude in suspended graphene devices. Fig.3.9 shows the resistivity versus gate voltage for the case of device SG5 between 300K and 30K. As seen in the figure, the resistivity at the Dirac point
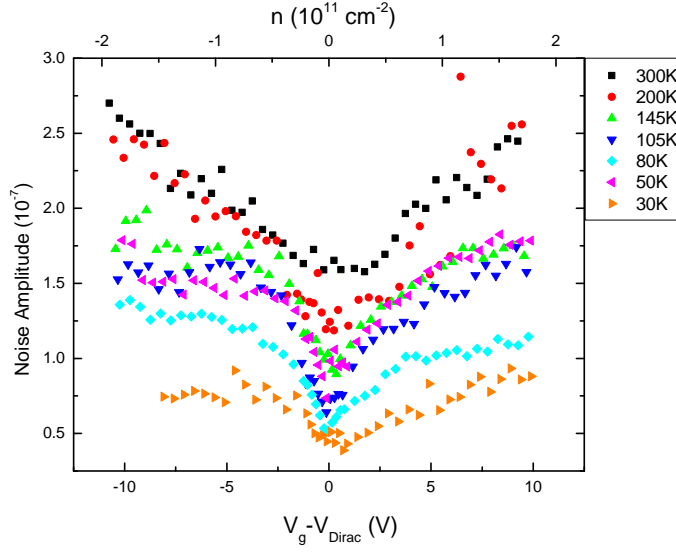
Figure 3.10: Noise amplitude dependence on gate voltage of SG5 in temperature range of 30-300K.

increases much more with decreasing temperature than in the case of on-substrate graphene, as a result of a reduced residual carrier density[38, 39]. On the other hand, the mobility of SG5 (and other suspended devices) shows very weak temperature dependence, similarly to on-substrate devices.

The dependence of the noise amplitude on gate voltage for SG5 at different temperatures is summarized in Fig.3.10, which is similar to that of other devices that exhibit a V-shape dependence. As temperature decreases from 300K to 30K, the noise amplitude decreases monotonically, except for an anomaly at T = 50K, in which the noise level is comparable to that between 105K and 145K. The overall noise reduction at 30K relative to 300K is about three times, that is, comparable to the reduction observed in NSG1 (Fig.3.7). The anomalous behavior at T = 50K has been observed in other suspended devices, although at different temperatures. Its origin is not known.

## 3.4 Noise model from Hooge's relation with a variable Hooge parameter

To shed light on the results described in Section 3.3, we have revisited Hooge's relation assuming a variable Hooge parameter. Indeed the quantity of $\alpha_H$ is not necessarily a constant, but may instead depended on crystal quality and on the scattering mechanisms that determine the mobility $\mu$[59]. In a graphene device these include charged impurity scattering, short range disorder scattering, ripple scattering, etc.[15]. While the carrier mobility associated with charged impurity scattering has been shown to be $V_g$ independent, mobility associated with all other scattering mechanisms does depend on $V_g$[15]. Thus it is reasonable to assume that $\alpha_H$ should also depend on $V_g$ instead of being a constant.

Based on the above consideration, we characterize graphene by its mobility and look for a correlation between $\alpha_H$ and $\mu$. The calculated Drude mobility ($\mu = \sigma/ne$) and the Hooge parameter $\alpha_H = A \times N = (S_V/V^2) \times f \times N$ for all the samples studied (both on-substrate and suspended graphene) are plotted in logarithmic scales on the upper part of Fig.3.11. Because of potential fluctuations induced by charged impurities, the carrier concentration in the vicinity of Dirac point cannot be reduced to zero. Charge carrier density smaller than residual charge desnity (typically $10^{11}cm^{-2}$ or $V_g \sim$ few V in on-substrate devices, and $10^{10}cm^{-2}$ or $V_g \sim$ 1V in suspended devices) is not considered for $\alpha_H$ and $\mu$ calculations.

For each sample there are two curves (that in many cases practically overlap), corresponding to the electron and hole branches of Figs.3.4 and 3.5. The correlation between $\alpha_H$ and $\mu$ is obvious: in all cases $\alpha_H$ decreases with increasing $\mu$, but for suspended graphene devices the decrease is considerably slower than for on-substrate devices, corresponding to slopes of approximately -1.5 and -3, respectively, as shown in Fig.3.11. In principle, we do not have any reason to believe that this definite difference in slope values is intrinsic, and it
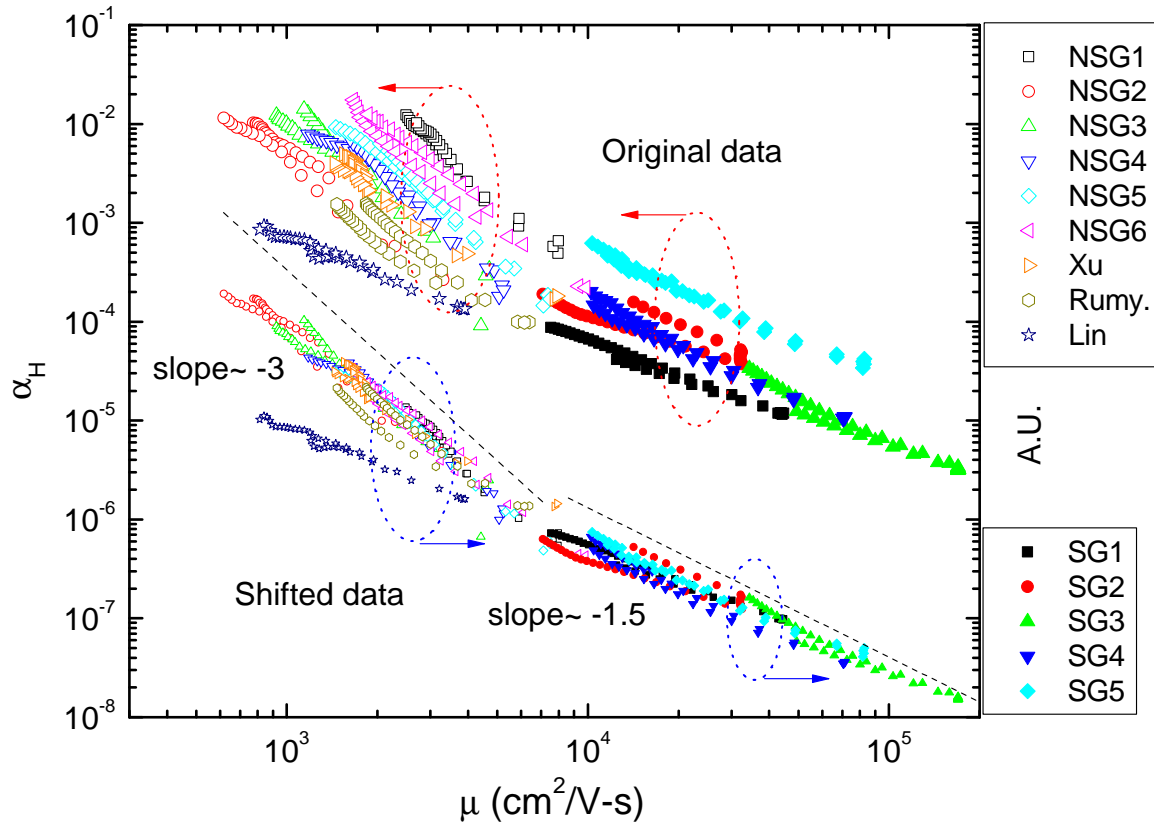
Figure 3.11: Dependence of Hooge parameter on carrier mobility at room temperature. The hollow symbols are results from on-substrate devices and the solid symbols are results from suspended devices. The upper part is the original data, and the lower part is shifted by dividing Hooge parameter with an arbitrary number to make them fall on the same master curve. Shifted data are using the same symbols as their original counterpart.

may simply represent two different regimes of a common dependence. The fact that both the devices with V-shaped noise characteristics and those with M-shaped characteristics have very similar $\alpha_H$ vs $\mu$ dependence suggests that there is a physical phenomenon behind such a common dependence, and calls for further experimental and theoretical study.

In Fig.3.11, we have also included data extracted from the literature[48, 53, 56], plotted along our own data to test the generality of our model. These data were extracted to our best knowledge with information on the publications. Here we note that the $\alpha_H$ vs. $\mu$ curve of graphene nanoribbon from Lin *et al.*(2008)[48] has a unique slope $\sim$ -1, which leads to $A = \alpha_H/N \sim 1/\mu N \sim R$ hence the observed noise amplitude showed a maximum at Dirac point[48]. Although this behavior appears qualitatively different from the results from wide graphene devices, the physical models behind them are quite similar, the only difference is the slope of $\alpha_H$ vs. $\mu$ dependence. The deviation of the slope for graphene nanoribbon may be attributed to the change of electronic structures in the geometrically confined devices.

In both suspended and on-substrate graphene devices, the $\alpha_H$ – $\mu$ dependence at T = 300K shown in Fig.3.11 persists at lower temperatures, down to 30K, although in general, the lower temperature the smaller value of $\alpha_H$, such as the results of SG5 shown in Fig.3.12. Since $\mu$ is almost independent of T (see the discussion above in relation to Figs.3.6 and 3.9) but $\alpha_H$ is not, we can factorize $\alpha_H$ double dependence on $\mu$ and T:

$$\alpha_H \sim f(\mu) \times g(T), \tag{3.2}$$

where $f(\mu)$ can be approximated as $(1/\mu)^\delta$ with $\delta \sim 1.5$ and 3 for suspended and on-substrate devices, respectively, and $g(T)$ is related to the temperature-dependent dynamic nature of the trapping-detrapping process, density fluctuations, etc. in the devices.

By treating $g(T)$ as temperature and device dependent but mobility independent, we can
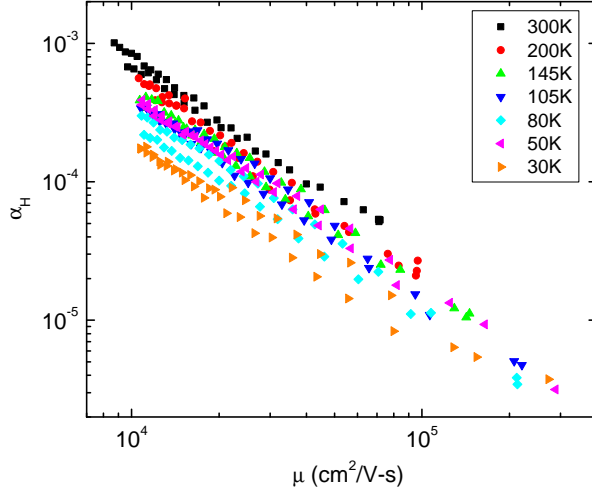
Figure 3.12: Hooge parameter $\alpha_H$ dependence on carrier mobility $\mu$ in SG5 at temperatures from 30 to 300K.

divide $\alpha_H$ in Fig.3.11 by different constant values (for different devices) to get a "master" curve shown in the lower part of Fig.3.11. All of the curves fall on top of a "master" curve. This is in good agreement with our assumption that the "static" scattering has a universal contribution to the noise amplitude from mobility fluctuations while the values of the actual noise amplitude is also affected by "dynamic" contributions that do not have a direct correspondence in the DC transport characteristics.

Based on the mobility dependence of the Hooge parameter $\alpha_H \sim f(\mu)$, the experimentally observed $V_g$ dependence of noise amplitude is directly related to the $V_g$ dependence of mobility $\mu$. Here we consider the two major scattering mechanisms that limit graphene device mobility, short-range disorder scattering and long range Coulomb scattering (from charged impurities, etc.)[15]. These two types of scatterings exhibit different $V_g$ dependence: the contribution to the mobility associated with short range scattering follows $\mu_S = 1/(C_S V_g)$ whereas the contribution related to long range Coulomb scattering is constant $\mu_L = 1/C_L$[60–
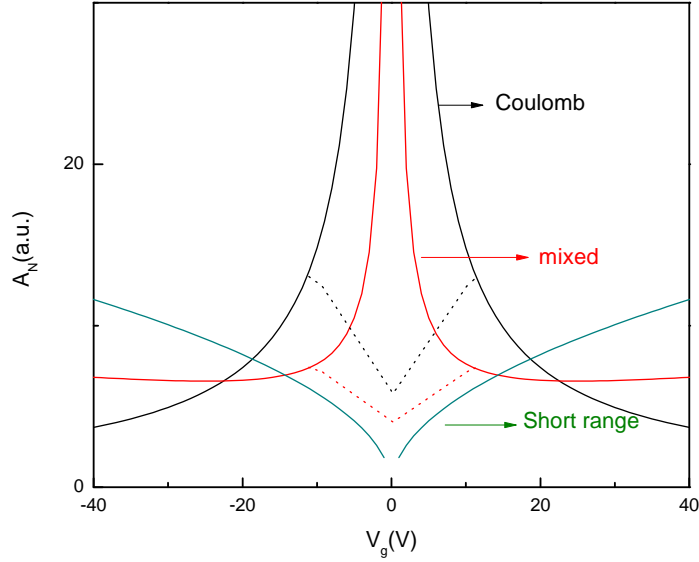
Figure 3.13: Qualitative noise amplitude dependence on gate voltage for the Coulomb, short range, and mixed scattering. The dotted lines near charge neutrality indicate the gate voltage dependence of noise amplitude when considering charge carrier inhomogeneity.

62]. Here $C_S$ and $C_L$ are constants that depend on the density and intensity of their corresponding scattering centers. The resulting device mobility follows $\mu = (1/\mu_S + 1/\mu_L)^{-1}$ (Matthiessen's rule). From Hooge's relation and $\alpha_H \sim 1/\mu^\delta$ at fixed temperature, we can write the noise amplitude as,

$$A = \alpha_H/N \sim (1/\mu)^\delta/N \sim (1/\mu_S + 1/\mu_L)^\delta/V_g \sim (C_S \cdot V_g + C_L)^\delta/V_g. \qquad (3.3)$$

The above expression explains (at large $V_g$ away from the e-h puddles) the variety of $V_g$ dependences of noise observed in different samples. For example, in SG devices the noise amplitude increases with increasing magnitude of gate voltage, while in many NSG devices the dependence is the opposite. Such difference can be understood as a result of the relative

contribution of different types of scatterings. In SG devices, due to the near-absence of Coulomb scatterers, the mobility is mainly affected by the short range disorders, which give rise to: $A \sim V_g^{\delta-1}$, increasing with increasing $V_g$ for $\delta > 1$. For NSG, on the other hand, the mobility is mainly limited to Coulomb scattering, and $A \sim 1/V_g$, decreasing with increasing $V_g$. More generally, in Fig.3.13 we plot qualitatively noise amplitude $A$ vs. $V_g$ for three representative cases in which charge scattering is Coulomb, short range, and mixed. The solid lines represent ideal situations where there is no potential fluctuation.

However, the $V_g$ dependent noise near the charge neutrality point needs to be considered with potential fluctuation. Here the observed noise amplitude increases with increasing $V_g$ even for Coulomb scattering dominated devices, creating a "dip" in the noise vs. $V_g$ dependence (thus the "M"-shape for these NSG devices). Such a behavior cannot be explained by the model mentioned above. Near the charge neutrality point, potential fluctuation from impurity scattering and temperature excitation affect the charge transport, and the graphene channel is no longer homogeneous, but consists of "puddles" with different carrier densities. Such a complicated system can be no longer described by a simple Hooge's relation. We may consider the graphene channel as a network of resistors, each with different carrier number. Within the potential fluctuation regime, changing $V_g$ creates an imbalance of electrons and holes, while the total number of carriers $(N_e + N_h)$ remains roughly the same. We notice that such scenario has been proposed by Xu *et al.*(2010) [53], where the "dip" in the noise–$V_g$ dependence was explained by the sum of normalized current noise from parallel conduction channels of electrons and holes. Here we consider the problem with similar idea, but calculate the total noise (instead of normalized noise) for resistors both in series and in parallel. When considering the effect of resistors in series, taking the simplest example of two resistors, the

total noise amplitude is:

$$S_R = S_{R1} + S_{R2} = \frac{R_1^2 \alpha_H}{N_1} + \frac{R_2^2 \alpha_H}{N_2} \sim \frac{1}{N_1^3} + \frac{1}{(N - N_1)^3} \tag{3.4}$$

Here we simplify the resistance of each resistor as $R_i \sim 1/N_i$ for easy discussion, considering that Coulomb scattering dominates low carrier densities, which gives rise to a conductance that is linear in carrier density. Based on the above model, the minimum noise happens when $N_1 = N_2 = N/2$. It should be noted that such result can be generally reached as long as the resistance $R_i$ decreases monotonically with increasing $N_i$ (not necessarily as $R_i \sim 1/N_i$).

One should also consider the case when the two resistors are in parallel. In this case it is convenient to calculate noise in terms of conductivity noise:

$$S_\sigma = S_{\sigma 1} + S_{\sigma 2} = \frac{\sigma_1^2 \alpha_H}{N_1} + \frac{\sigma_2^2 \alpha_H}{N_2} \sim N_1 + N_2 = N \tag{3.5}$$

Hence the total noise of two resistors in parallel is independent on the imbalance of the carrier number in electrons and holes, as long as the total carrier number is constant.

In all, when we consider the total noise of the network of resistors representing puddles of graphene with different carrier densities, the total noise of the graphene channel has its minimum when the channel is at its charge neutrality point, where all the puddles have generally the same carrier number. As gate voltage increases into the electron (hole) branch, the carrier numbers in the hole (electron) puddles decrease, resulting an increase in the total noise amplitude as long as these puddles are partially in series with each other. With higher $V_g$ where the system is outside of the potential fluctuation regime, noise starts to decrease with increasing $V_g$, determined by long range Coulomb scattering as explained earlier, which generates an M-shape gate-voltage dependence of noise amplitude.

## 3.5 Conclusion

In summary, we have studied low-frequency noise in suspended-graphene and graphene-on-SiO$_2$ devices. To explain the experimental data, we have used a modified Hooge's relation in which the parameter $\alpha_H$ is not constant but depends monotonically on the device's mobility. From an analysis of the experimental results it follows: 1) at large carrier densities where the Fermi level is outside of the potential fluctuation regime, the details of the noise – $V_g$ dependence is determined by the relative strength of short- and long-range scattering at large carrier densities; 2) within the potential fluctuation regime the dependence of noise on $V_g$ is mainly determined by the evolution of charge carrier inhomogeneity/imbalance near the charge neutrality point. By suspending the graphene devices and reducing the charge trapping and scattering centers, we demonstrate reduction in Hooge parameter in suspended graphene devices.

| Sample Name | Name in thesis | Suspended? | Length($\mu m$) | Width($\mu m$) |
|:---:|:---:|:---:|:---:|:---:|
| LZ61-F1 | NSG1 | No | 11.5 | 6.25 |
| LZ74-F6-12 | NSG2 | No | 0.85 | 0.4 |
| LZ74-F6-14 | NSG3 | No | 0.87 | 0.59 |
| LZ74-F6-74 | NSG4 | No | 0.85 | 1.12 |
| LZ74-F6-78 | NSG5 | No | 1.02 | 1.9 |
| LZ73-F2 | NSG6 | No | 1.07 | 0.25 |
| LZ71-F1 | SG1 | Yes | 0.63 | 3.3 |
| LZ71-F3 | SG2 | Yes | 0.7 | 2.6 |
| LZ71-F4 | SG3 | Yes | 0.75 | 2.1 |
| LZ75-F2 | SG4 | Yes | 0.94 | 1.8 |
| LZ75-F4 | SG5 | Yes | 0.92 | 1.3 |

Table 3.1: Description of samples used in noise measurements.

# Chapter 4

# Magnetotransport Study of Graphene

## 4.1 Metal to insulator transition on the n=0 Landau level in graphene

### 4.1.1 Introduction

As described in Sec.2.5, graphene has quantized Landau levels (LLs) with four-fold degeneracy. The $n = 0$ LL corresponds to two Fermi points in the honeycomb lattice ($K$ and $K'$ valleys) and two spin states. States with different spin and valley indices will split in energy under interactions (see Fig.4.1 (a)). Spin splitting results from Zeeman interaction, while valley splitting results from lattice imperfections and inter-valley scatterings[63]. The nature of the electronic states at the $n = 0$ LL has recently come under intense theoretical and experimental scrutiny but still remains unclear. While some theories predict unusual metallic transport via gapless edge states [12, 13], others suggest that a gap may appear at high magnetic fields, resulting in an insulating state near the charge neutrality point (CNP) [14, 15]. However, theories mainly focus on quantum Hall transport in the absence of strong

electrostatic disorder, which, along with the Coulomb interaction, plays a key role in defining electron localization in 2DEG[64, 65].

Several groups have experimentally studied charge transport in the $n = 0$ LL regime near the CNP in graphene, with conflicting results [11, 13, 43, 66–71]. Some groups have observed finite longitudinal resistance $R_{xx} \lesssim R_K$ ($R_K = h/e^2$ is the resistance quantum) even at high magnetic fields, where the QHE plateau at $R_{xy} = R_K/2$ is well developed [11, 13, 43, 67, 68]. In contrast, others have found a marked resistance increase, to $R_{xx} \gg R_K$, and a plateau of nearly zero Hall conductivity near the CNP in high fields, suggesting a breakdown of the $n = 0$ QHE and an insulating state at low temperatures[66, 69–71].

In some high-mobility samples a plateau at $\nu = 1$ ($\nu = n_s h/(eB)$ is the filling factor) and $R_{xy} = R_K$ was also observed, indicating inter-valley splitting of the $n = 0$ LL, [66, 71]. In Ref. [69], $R_{xx}(B) \gtrsim 100 R_K$ was reported at the CNP, and its divergence with the field was associated with a Kosterlitz-Thouless (KT) transition at a sample-dependent critical field $B_c$ ($\gtrsim 18$ T), which was lower for better quality samples. The field-induced insulator behavior was later correlated with the filling factor $\nu$, and evidence for two different insulating regimes at $\nu \lesssim 1$ was found [71]. More recently, magnetic field driven insulator phases have been observed in both single and double layer high mobility suspended graphene samples, where they emerge from $\nu = 1$, as well as fractional $\nu = 1/3$ QHE states [72–74].

The phase diagram of the electronic states at the $n = 0$ LL in graphene emerging from the above observations is quite complex. However, it seems to have a universal constituent: a metal-insulator transition (MIT) where the incompressible electronic liquid state of the QHE plateau is followed by a localized insulating phase (Fig. 4.1 (b)). How the dissipative regime develops in a system of Dirac electrons in graphene – where robust quantum Hall transport is sustained up to 100 K and above – is a fundamental open issue, which we address here by performing temperature-dependent magnetotransport measurements. We identify the first
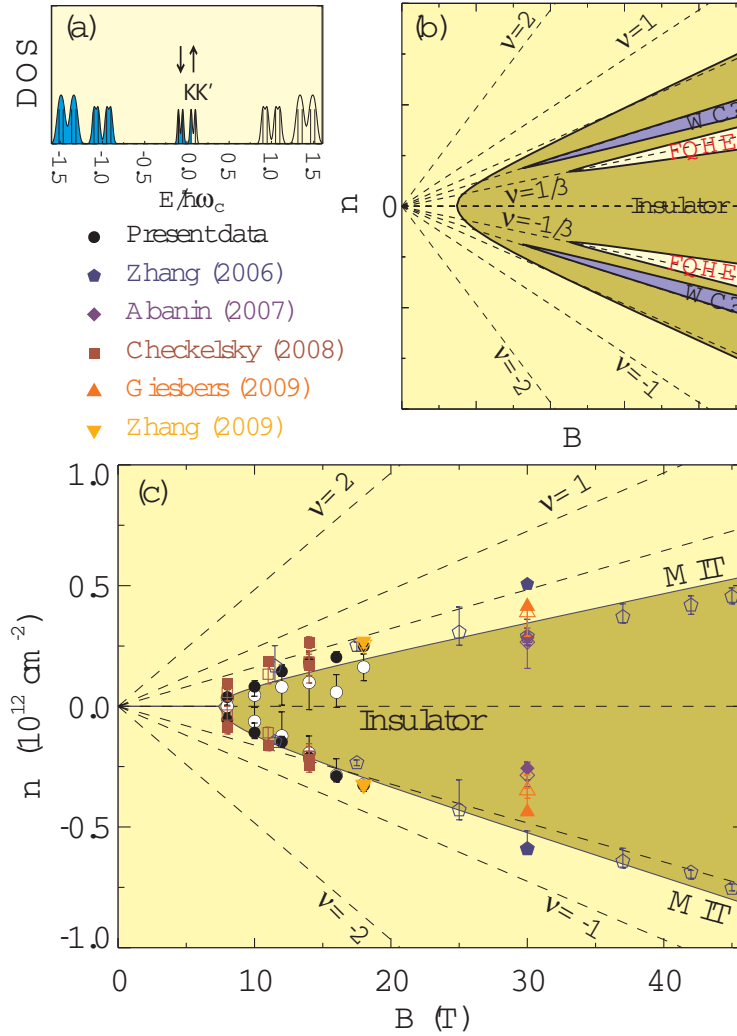
Figure 4.1: (a) Splitting of the Landau levels in graphene. (b) A schematic phase diagram of the electronic states on the $n = 0$ LL consistent with the results of Refs. [66–74]. (c) The experimental phase diagram of the quantum Hall metal-insulator transition in graphene obtained from our data and data published in Refs. [66–74], reconciling various existing observations. Symbols are explained in the text.

of these MIT, which occurs at $\nu \approx 0.65$, and establish its low-temperature ($n_s$, B) phase diagram, shown in Fig. 4.1 (c).

### 4.1.2 Experimental

Monolayer graphene FETs were fabricated following the methods stated in Sec.2.6. The device was defined as hall bar geometry with a separate EBL, and later etched with $O_2$ plasma. (The optical image of the device investigated in this study is shown in the inset of Fig. 4.3 (a)). Transport measurements were conducted at National High Magnetic Field Laboratory (NHMFL) in Tallahassee, Florida. The measurements were conducted with lock-in technique, where we connected $100 M\Omega$ resistor in series between the lock-in output and the device with a lock-in output voltage of 1V to supply a constant 10nA through the graphene device, and the lock-in frequency was set to 7Hz.

### 4.1.3 Results and discussion

The longitudinal and Hall resistivities $\rho_{xx(xy)}$ of our graphene sample at the base temperature (T = 0.25 K) and B = 18 T are shown in Fig. 4.2. The corresponding conductivities were obtained by standard matrix inversion, $\sigma_{xx(xy)} = \rho_{xx(xy)}/(\rho_{xx}^2 + \rho_{xy}^2)$. A peculiar behavior is observed near n = 0 LL filling, where $\rho_{xx}$ (and $R_{xx} \approx 3\rho_{xx}$) become large, noticeably exceeding $R_K$, and a two-peak structure in $\sigma_{xx}$ concomitant with a "zero plateau" of $\sigma_{xy} \approx 0$ appears (Fig. 4.2 (b)). These observations agree with previously reported findings [13, 69–71].

The full ($n_s$, B) dependence of the longitudinal resistivity and conductivity at T = 0.25 K is summarized in Fig. 4.3 in the form of color contour plots. The data was collected by gate voltage sweeps at fixed B every 2 T.To adjust for the number of squares between the voltage
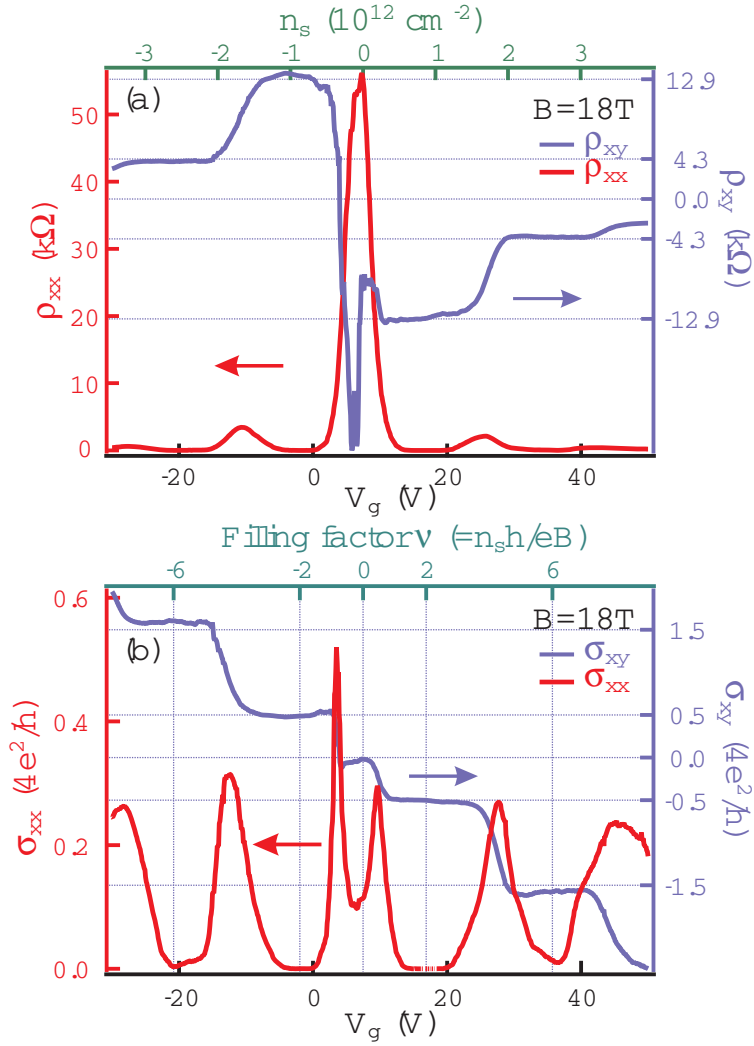
Figure 4.2: QHE data as a function of the gate voltage $V_g$, for B = 18 T at T = 0.25 K, used in Fig. 4.3. (a) $\rho_{xx}$ and $\rho_{xy}$, top axis shows the corresponding carrier density $n_s$. (b) $\sigma_{xx}$ and $\sigma_{xy}$, top axis shows LL filling factor $\nu$.

probes, longitudinal and Hall measurements were performed for two opposite directions of magnetic filed, and $\rho_{xx}$ and $\rho_{xy}$ were obtained by enforcing the symmetries on the resulting quantities. As seen in Fig. 4.3 (a), $\rho_{xx}$ displays well-developed Shubnikov-de Haas oscillations (SdHOs) fanning away from the CNP, $V_0 \approx 7.5$ V, with increasing B. Maxima of $\rho_{xx}$ track LL filling $\nu = 0, \pm 2, \pm 6, \pm 10, ...$, which is typical of graphene [11, 34, 43]. Despite the moderate mobility of our sample, ($\mu \approx 5.8 \times 10^3$ $cm^2/V \cdot s$), the QHE regime develops for B $\gtrsim 4$ T, with plateaus at $\rho_{xy} \approx \frac{1}{2} R_K$ and $\rho_{xx} \approx 0$. However, the $\nu = 1$ plateau is not observed, indicating that electrostatic disorder is strong enough so that the inter-valley splitting of the $n = 0$ LL is not resolved for B $\leq 18$ T.

A striking feature in Fig. 4.3 (a) is a well-defined resistive region near $n_s = 0$ that appears at B $\gtrsim 9$ T, where $\rho_{xx} \gtrsim R_K/2$. Its boundary is clearly correlated with maxima in $\sigma_{xx}(n_s, $ B$)$ (Fig. 4.3 (b)), and in the derivative of the Hall conductivity, $d\sigma_{xy}(n_s, $ B$)/dn_s$ (Fig. 4.3 (c)). The latter implies step-like behavior of $\sigma_{xy}$, corresponding to a plateau phase near $n_s = 0$. While these observations clearly identify a well-defined region in $(n_s, $ B$)$ space corresponding to a resistive plateau phase near $n_s = 0$ for B $\gtrsim 9$ T, its nature remains unclear. Is this indeed a new electronic phase (insulator?) at the $n = 0$ LL, bounded by a phase-transition line in the $(n_s, $ B$)$ phase diagram?

In order to answer this question and understand the appearance of the resistive $n = 0$ LL state in Fig. 4.3, we studied the temperature dependence of the magnetoresistance data at B $= 18$ T shown in Fig. 4.2. The results of gate voltage sweeps at T $= 0.5, 1.5, 4, 10,$ 20, 30 and 50 K are shown in Fig. 4.4. Two regions are easily identified in the figure: a low-$n_s$ region where the longitudinal resistance increases with decreasing temperature, and another region at high carrier densities in which the resistance shows the opposite, metallic behavior (Fig. 4.4 (a)). An obvious feature separating the two regions are crossing points of the curves measured at different temperatures, where $\rho_{xx}$ is temperature-independent.
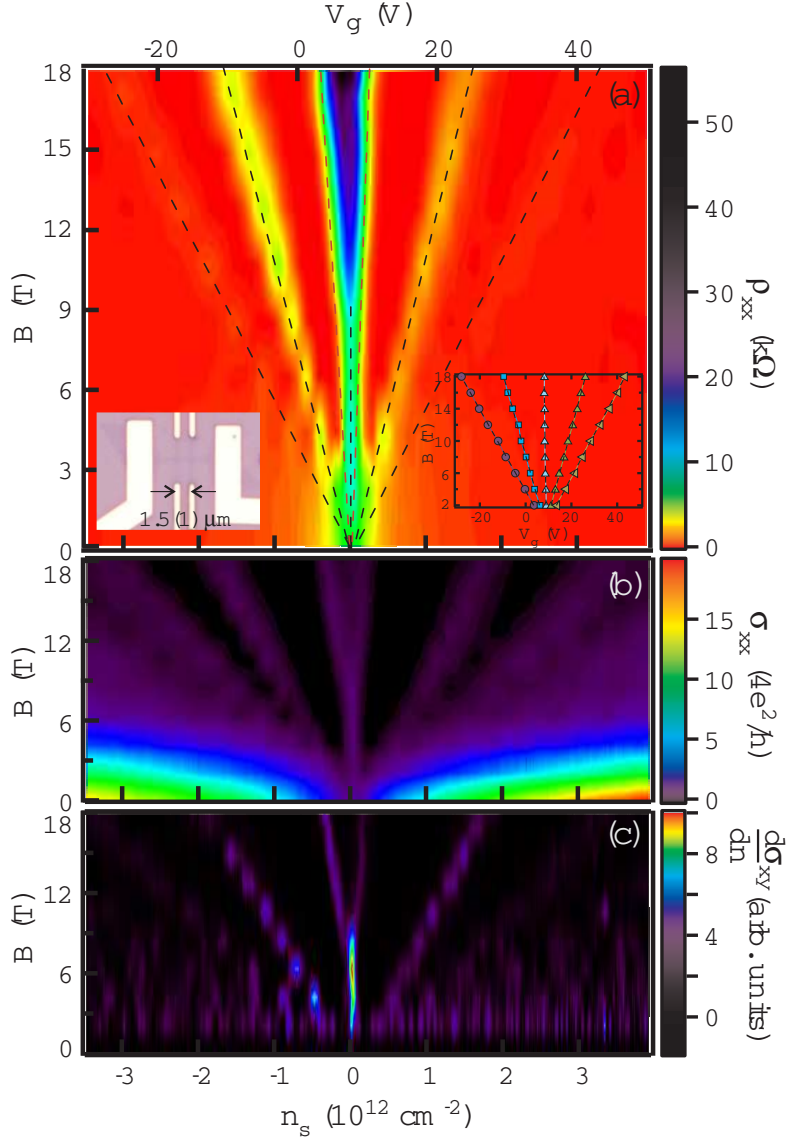
Figure 4.3: (a) Contour map of the longitudinal resistivity, $\rho_{xx} = R_{xx} \cdot W_s / L_s$, as a function of charge density $n_s$ and magnetic field B, $L_s = 1.5(1)\mu$m, $W_s = 0.5(1)\mu$m are sample dimensions. Top axis shows $V_g$. LL are clearly identified by ridges fanning away from $n_s = 0$ with increasing $B$, traced by black broken lines. Left bottom inset is the optical image of the device. Right bottom inset shows the LL fan diagram with fits yielding $n_s = C_V(V_g - V_0)$, $C_V = 9.2 \cdot 10^{10}$ cm$^{-2}$/V, for charge density and $V_0 = 7.5$V for the CNP. (b) The corresponding maps of the longitudinal conductivity, $\sigma_{xx}$, and (c) the derivative of the Hall conductivity, $d\sigma_{xy}/dn_s$.
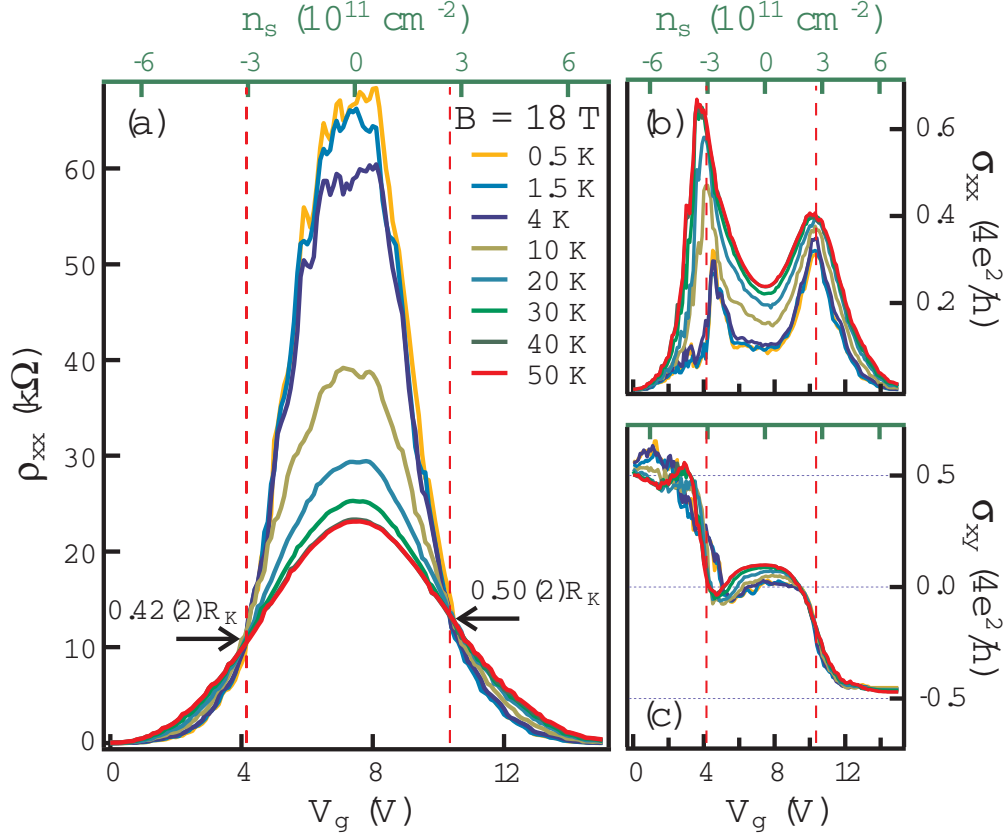
Figure 4.4: Temperature dependence of the longitudinal resistivity (a), and longitudinal (b), and Hall (c), conductivities versus $V_g$ and carrier density (top axes) at B = 18 T. Vertical broken lines show critical densities separating the insulating and the metallic phases, and are determined from the crossing points in panel (a).

Inspection of Fig. 4.4 (b), (c) shows that the insulator phase at low $n_s$ is marked by the appearance of a $\sigma_{xy} \simeq 0$ plateau and an accompanying two-peak structure in $\sigma_{xx}$. Thus, the low-$n_s$ plateau phase identified by the behavior of the conductivity in Figures 4.2, 4.3 at T = 0.25 K for B $\gtrsim$ 9 T, indeed corresponds to a distinct, insulating phase.

The metal-insulator transition in Fig. 4.4 occurs for $\nu_c^{(e)} \approx 0.57$, $\rho_{xx}^{(e)} \approx 0.5 R_K$ and $\nu_c^{(h)} \approx -0.75$, $\rho_{xx}^{(h)} \approx 0.42 R_K$, showing some 20% asymmetry between the electron and hole sides, respectively. However, the critical resistivity is remarkably close to the value $R_K/2$

expected for a metal-insulator transition in disordered 2DEG systems (the denominator 2 is a consequence of graphene valley degeneracy) [75–78]. Since contacts in our etched Hall bar device are non-invasive, the observed electron-hole asymmetry is unlikely to be contact-related. It probably arises from breaking of the particle-hole symmetry by random external potential, suggesting a connection of the observed MIT with electrostatic disorder [64].

A similar behavior of resistivity isotherms measured at different T as a function of magnetic field has previously been observed in conventional 2DEG systems at low carrier densities [75–77]. The crossing point of the $\rho_{xx}(B, T)$ curves where the sign of the temperature derivative $d\rho_{xx}/dT$ changes, has been associated with a transition from the QHE plateau phase to an insulator. Plateau-insulator transitions (PIT) have been observed both for integer and fractional QHE and are understood as metal-insulator quantum phase transition induced by Anderson (strong) localization of electrons in the presence of electrostatic disorder [64]. In 2DEGs the transition from the last integer QHE plateau to an insulator occurs at $\rho_{xx} \sim R_K$ and in the range $0.52 \lesssim \nu_c \lesssim 0.8$, similar to what we find in graphene, even though massless Dirac charge carriers could be expected to avoid localization by electrostatic potential.

Association of the MIT with the crossing point of resistivity isotherms is only meaningful when $\rho_{xx}(B, T)$ shows clear metallic and insulating behavior in a finite temperature range on the two sides of the transition [79]. As shown in Fig. 4.5, this is indeed the case for $1 \text{ K} \lesssim \text{T} \lesssim 50 \text{ K}$ for the $\text{B} = 18 \text{ T}$ data in our graphene sample. In a temperature window $10 \text{ K} \lesssim T \lesssim 50 \text{ K}$, $\log \rho_{xx}(B, T)$ is consistent with nearly linear dependence on $T^{-1/2}$ (Fig. 4.5 (b)), typical of Coulomb-gap-induced variable range hopping. Despite the limited dynamical range of our data, such dependence agrees visibly better than a simple activation dependence $T^{-1}$. This suggests that screened Coulomb interaction is an important player in driving the insulator state. The same T-dependence is retained across the transition, persisting with the slope sign change on the metallic side. Similar symmetry, where $\rho_{xx}(T, \nu - \nu_c) \propto 1/\rho_{xx}(T, \nu_c - \nu)$

near PIT, has also been observed in low mobility 2DEG [77].

Having established the signature of the MIT on the $n = 0$ LL in graphene, we now return to constructing its low-T (B, $n_s$) phase diagram. This is shown in Fig. 4.1 (c), which compiles various data reported earlier by other groups along with our own results. Closed symbols show the transition identified from the longitudinal resistivity, using $\rho_{xx} = R_K/2$, while open symbols correspond to the $\sigma_{xy} \simeq 0$ plateau phase, identified from $\sigma_{xy}(\nu_c) = 1/(2R_K)$, i.e. the mid-point between the $\nu = 0$ and the undeveloped $\nu = 1$ plateaus. The overall topology of the phase diagram, including the electron-hole asymmetry, is remarkably universal, although the exact MIT critical fields are slightly sample-dependent, especially at low B.

### 4.1.4   Conclusion

Thus, we have established the phase diagram of the metal-insulator transition at the $n = 0$ LL in graphene. MIT occurs in the regime of the dissipative transport, where $R_{xx} > R_K/2$, and at $\rho_{xx} \approx R_K/2$ ($R_{xx} \approx 3\rho_{xx}$ for our sample). It is surprisingly similar to the plateau-insulator transition in 2DEG [75–77], even though the strong localization driving the PIT in 2DEGs should be absent in graphene. This difference is clearly seen in the low-field part of the phase diagram of Fig. 4.1, where Klein tunneling of Dirac electrons in graphene impedes the low-density insulating phases [79]. In 2DEGs, the conductivities in the vicinity of the PIT follow a semicircle relation [80], indicating a transition to a peculiar quantum Hall insulator state [77]. It was found that in graphene a semicircle describes very well the transitions between plateaus in the metallic phase [13, 81]. For the $n = 0$ LL it predicts $\rho_{xx}^2 + \rho_{xy}^2 = (R_K/2)^2$, and therefore $\rho_{xx} \leq R_K/2$. We find that this is violated in the insulating phase, suggesting that $\rho_{xx} \approx R_K/2$ ($\sigma_{xx} \approx 2e^2/\hbar$) is the maximum metallic resistivity (minimum conductivity) of the dissipative Hall state on the $n = 0$ LL in graphene.
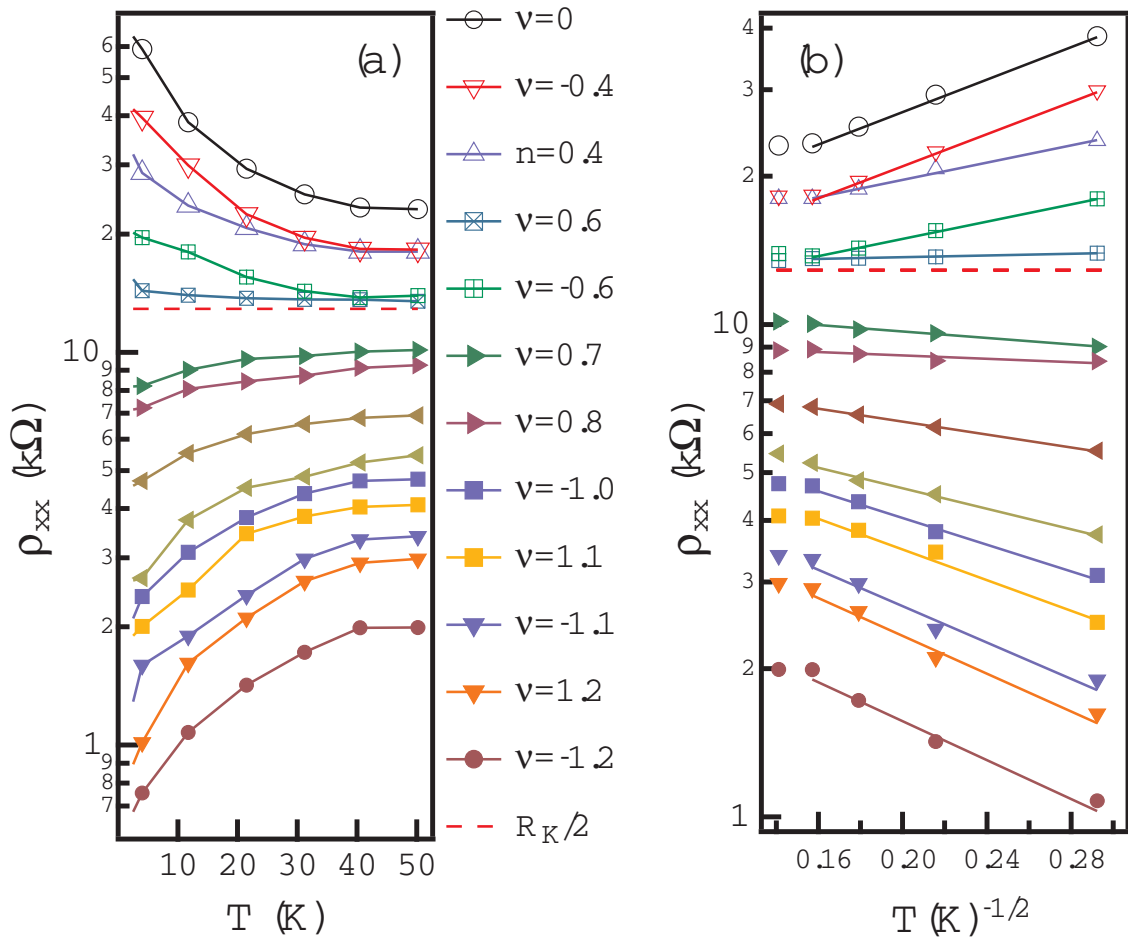
Figure 4.5: (a) Semi-log plot of $\rho_{xx}$ versus temperature at $B = 18$ T for 12 filling factors $\nu$, revealing the metal-insulator transition at $\nu_c \approx -0.7$ and $0.6$, where $\rho_{xx}(\nu_c) \approx R_K/2$ (dashed line). (b) Same data as a function of $T^{-1/2}$.

## 4.2 Quantum Hall effect in trilayer graphene

### 4.2.1 Introduction

As introduced in Sec.2.5, in monolayer graphene, the low energy band structure is described by chiral fermions with linear dispersion, and Berry's phase $\pi$. In bilayer graphene[16], chiral charge carriers have parabolic dispersion near the CNP, and Berry's phase $2\pi$. Unusual properties are revealed with magnetotransport experiments in perpendicular magnetic field, where Berry's phase determines the shift of SdHOs and their period is governed by the filling of Landau levels (LL) of chiral charge carriers. The peculiar nature and the four-fold degeneracy of electronic states lead to an unconventional sequence of QHE, where $\sigma_{xy}$ is spaced by $4e^2/h$ except for the first plateau, which is governed by the Berry's phase. While there is a significant interest in studying multiple-layer graphene systems, experimental progress has been limited, as low energy electronic properties depend heavily on the stacking orders of graphene layers, therefore it requires sample with well controlled stacking sequence[18, 34].

The electronic structure of multi-layer graphene is derived from hybridization of monolayer states via interlayer hopping. Its main features are captured by considering only hopping between the nearest-neighbor carbons, which are stacked on top of each other in adjacent layers with $\gamma_1 \sim 0.1\gamma_0$ as shown in Fig. 4.6(a), where $\gamma_0$ and $\gamma_1$ are the intra- and inter-layer hopping amplitude ($\gamma_0 \approx 3$ eV and $\gamma_1 \approx 0.4$ eV in bulk graphite)[22, 23, 82]. The low-energy electronic band structure of ABA-stacked trilayer graphene consists of superimposed linear and quadratic spectrum. Hence, transport is governed by two types of chiral quasiparticles, monolayer-like massless and bilayer-like massive, with an effective mass $m_{ABA} = \sqrt{2}\, m_{AB} \approx 0.05 m_e$ ($m_e is electron mass$), which is larger than it in bilayer graphene. Recent studies revealed that in contrast to bilayer graphene, where external electric field opens up a bandgap[83], in ABA-stacked trilayer graphene the electric field leads to a tunable
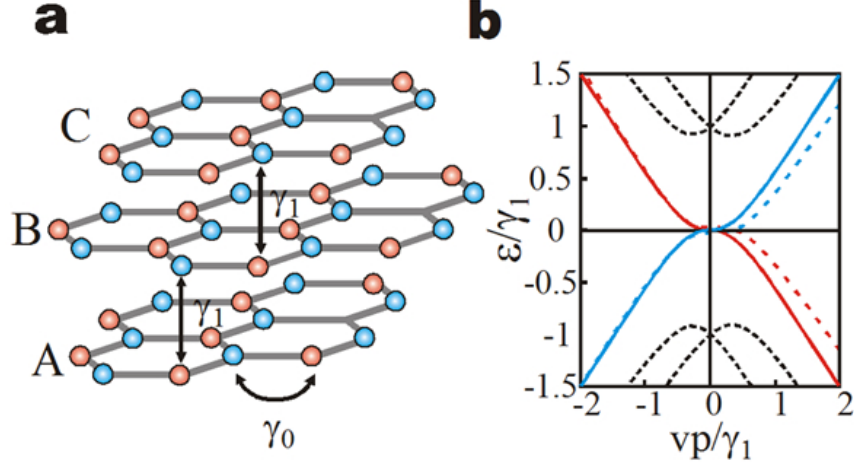
Figure 4.6: (a) ABC-stacked trilayer graphene. (b) Band structure of ABC-stacked trilayer graphene, with cubic low-energy dispersion $\varepsilon(p) = \gamma_1(vp/\gamma_1)^3$.

band overlap[17–20, 84, 85], whereas ABC-stacked trilayer graphene has chiral quasiparticles with cubic dispersion[22, 23, 29, 34, 82], $\varepsilon(p) = \gamma_1(v_F p/\gamma_1)^3$, as shown in Fig. 4.6(b).

So far no group has reported magnetotransport in ABC-stacked trilayer graphene. We have measured the magnetotransport properties in ABC-stacked trilayer graphene FET as a function of charge carrier density, magnetic field (up to 31 Tesla) and temperature ($0.3K < T < 50K$). SdHOs reveal four-fold degeneracy of Landau levels, and a Berry's phase of $3\pi$. We have also observed the corresponding unconventional sequence of QHE plateaus, where $\sigma_{xy} = \pm 6e^2/h, \pm 10e^2/h, \pm 14e^2/h, \cdots$.

### 4.2.2 Device preparation and identification of stacking order

The trilayer graphene device's preparation procedure and measurement method are described in Sec.4.1.2. We used kish graphite, instead of HOPG, to exfoliate graphene.

The number of layers was identified by measuring intensity difference of reflected green light between graphene and the substrate under optical microscope, and confirmed by the full
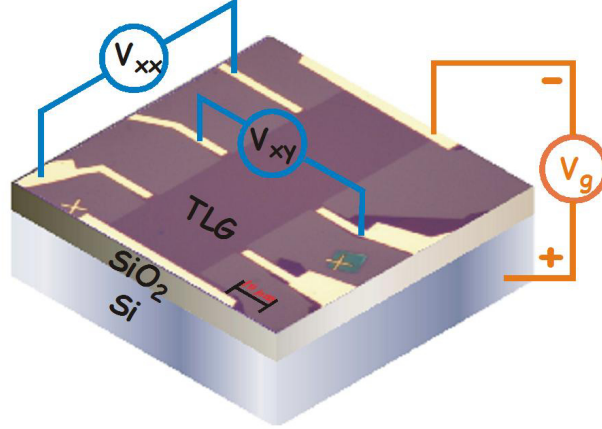
Figure 4.7: The image of the etched Hall bar trilayer graphene (TLG) device used in our experiments and schematics of the measurement setup. The black scale bar is 10 $\mu$m.

width at half-maximum (FWHM) of the 2D band of Raman spectroscopy[49]. This method can provide the number of layers precisely, but only until recently, it can give information about the stack orders of carbon layers in trilayer graphene[86, 87]. Raman spectroscopy was carried out in a WITec Raman system with laser wavelengths of 514 nm. In Fig. 4.8, the red curve corresponds to our trilayer graphene device. For comparison, the Raman spectrum of ABA-stacked trilayer graphene (exfoliated from HOPG) is plotted with blue curve. By observing the characteristic asymmetric shape of the 2D Raman band with a dip near 2700 cm$^{-1}$, as shown in Fig. 4.8 red curve, the device was identified as ABC-stacked.

In order to verify the sample uniformity, we performed scanning Raman mapping of large areas in our device. Raman spectra were recorded pixel-by-pixel by moving the motor controlled sample stage with WITec software at a step size of 0.5 $\mu$m. In addition to the G peaks and 2D peaks spectra at each pixel (with spacial dimension 12.5$\mu$m $\times$ 25$\mu$m), we also fit all spectra with Gaussian function. The spatial map of FWHM and center peaks of the 2D band are shown in Fig. 4.9 (a) and (b), respectively. The distinct shape of peaks in the
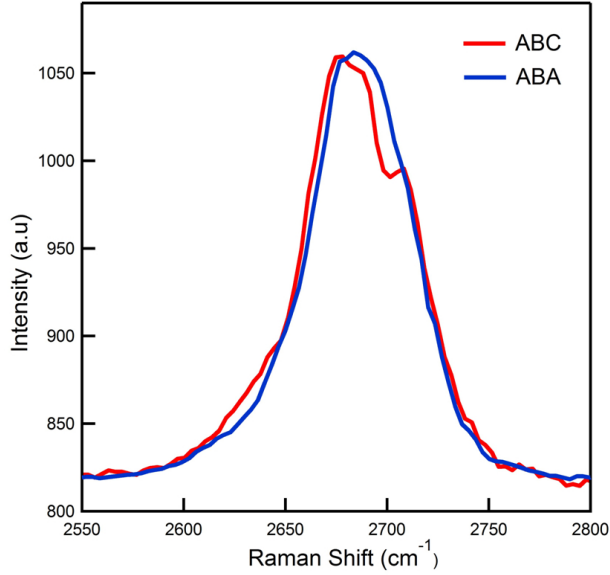
Figure 4.8: Raman spectrum of 2D band in trilayer graphene with different stacking orders. Red line (our device) is ABC-stacked, in contrast to graphene exfoliated from HOPG whose 2D band of Raman spectrum is believed to be ABA-stacked.

ABC- and ABA-stacked graphene leads to a slight but noticeable difference in the position and FWHM of the Gaussian peaks. The mapping results exhibited a homogeneous ABC stacking order instead of a mixture of ABA and ABC stacking order in the device.

### 4.2.3 Transport measurements

Fig. 4.7 shows the transport measurement setup and the trilayer graphene device measured in our experiments. The conductivity $\sigma_{xx}$, shown in Fig. 4.10(b), increases linearly with increasing carrier density $n_s$ (or gate voltage $V_g$) for both polarities(electron/hole), and charge neutrality point shifts to around $V_g$=20V which is due to unintentional charge impurity doping. The mobility $\mu$, calculated with Drude model $\sigma = n_s e \mu$, is characterized as a function of carrier density $n$ in the sample, and is shown in Fig. 4.10(a). In this trilayer device, $\mu$ is around 1800 $cm^2 V^{-1} s^{-1}$ at high carrier concentration.
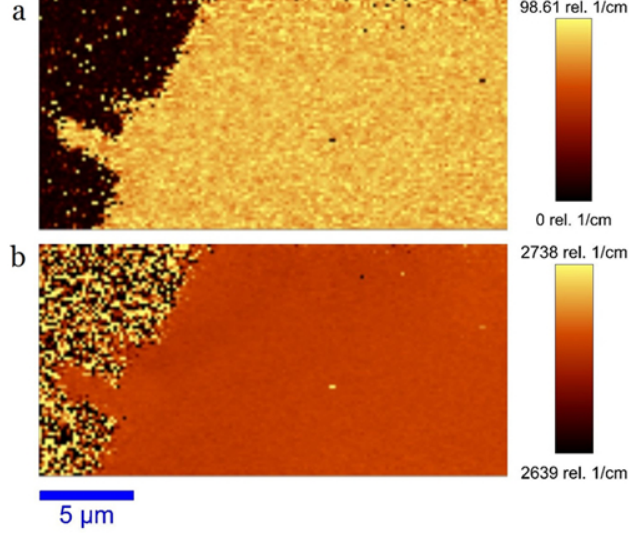
Figure 4.9: The spatial map of FWHM and center peaks of the 2D band. The figures illustrate that graphene device has uniform domain of stacking order. The scale bar is 5 $\mu$m.

Having established high quality ABC-stacked trilayer graphene device, we proceeded with magnetotransport measurements in perpendicular field B. We have observed unusual QHE developed in our sample at T $\approx$ 0.35K in fields above 15 Tesla, as shown in Figs.4.11, 4.12. Plateaux of Hall conductivity are observed at $\sigma_{xy} = \pm 6e^2/h, \pm 10e^2/h, \pm 14e^2/h, \cdots$, with a step of $12e^2/h$ between the hole and electron gases across the $n = 0$ LL, suggesting its 12-fold degeneracy. This, perhaps, is most clearly seen in Fig. 4.12, which shows the magnetic field dependence of the longitudinal resistivity $\rho_{xx}$, and Hall resistivity $\rho_{xy}$, for $V_g = 70$V ($n_s \approx 5 \times 10^{12} cm^{-2}$). The minima of $\rho_{xx}$ occur near the center of $\rho_{xy}$ plateaux, at LL filling factors $\nu = n_s h/(Be) = 6, 10, 14, \cdots$, as indicated by the arrows. The behavior near the $n = 0$ LL is in sharp contrast to that in the monolayer and bilayer graphene, where the first QHE plateau develops at $\sigma_{xy} = \pm 2e^2/h$ ($\nu = 2$) and $\sigma_{xy} = \pm 4e^2/h$ ($\nu = 4$), respectively. There is only a weak anomaly in our sample for $n_s$ below the first QHE plateau at $\nu = 6$, which can be associated with $\sigma_{xy} = \pm 3e^2/h$ ($\nu = 3$), and is probably an indication of

65
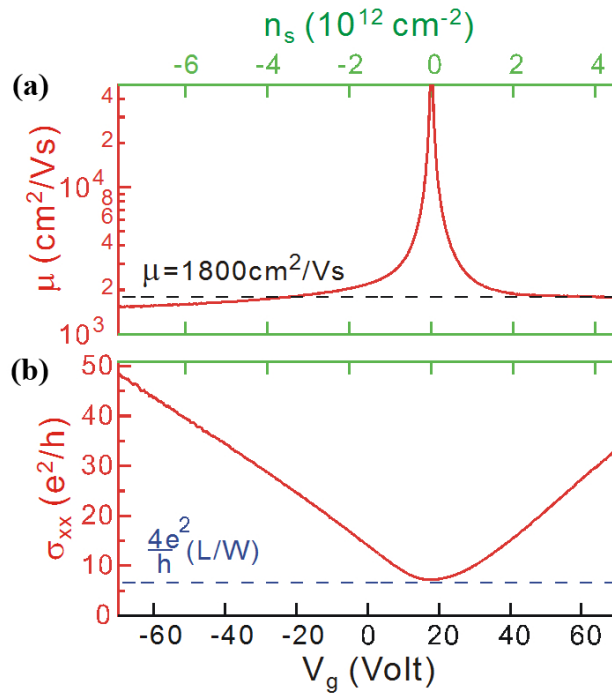
Figure 4.10: Mobility and conductance of trilayer graphene as a function of $V_g$ at temperature T=0.35K (a) Mobility as a function of back gate voltage $V_g$. Top scale shows the corresponding carrier density induced by electric field effect.(b) Longitudinal conductivity of the trilayer graphene device in Fig. 4.7.
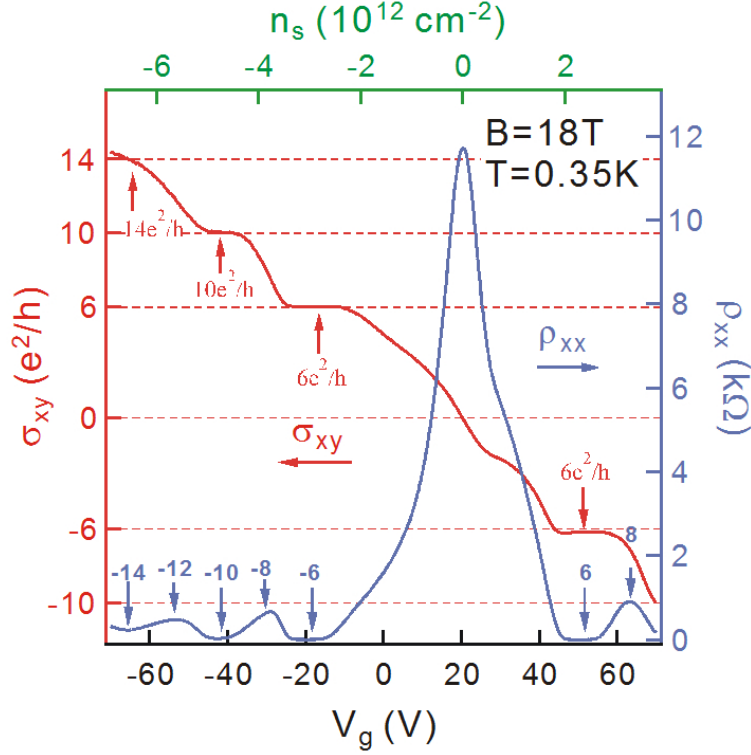
Figure 4.11: Longitudinal resistivity $\rho_{xx}$ (blue, right scale) and Hall conductivity, $\sigma_{xy} = \rho_{xy}/(\rho_{xx}^2 + \rho_{xy}^2)$, (red, left scale) of the trilayer graphene device as a function of $V_g$ (carrier concentration $n_s$) at B = 18 T and T = 0.35 K. The unit for $\sigma_{xy}$ is the conductance quantum, $e^2/h$. Vertical arrows with numbers show Landau level filling, $\nu = n_s h/eB$, for the corresponding quantum Hall states.

development of spin-splitting.

Now let's take a closer look at the SdHOs. SdHOs at $V_g$=43, 53, 70V as a function of $B$ at $T$=0.35K is shown in Fig. 4.13. In the semi-classical limit of small magneto-oscillations, the ratio of $\Delta\rho_{xx}$ and $\rho_0$, where $\rho_0$ is the resistivity at B=0 and $\Delta\rho_{xx}$ is $\rho$ (B≠0) $- \rho_0$, can be described by the Ando-Lifshitz-Kosevich (ALK) formula[43, 88],

$$\Delta\rho_{xx} = \rho(B,T)cos[2\pi(B_F/B + 1/2 + \beta)] \tag{4.1}$$
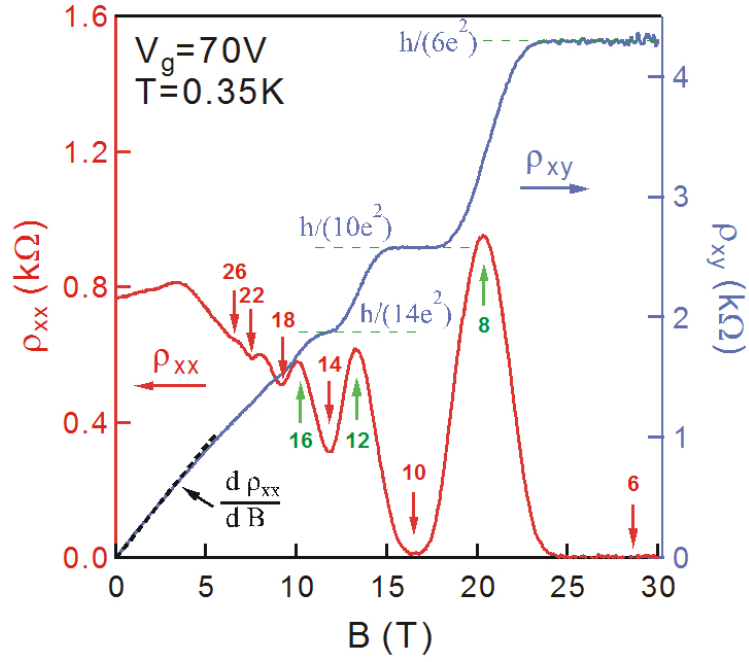
Figure 4.12: Longitudinal resistivity $\rho_{xx}$ (red, left scale) and Hall resistivity $\rho_{xy}$ (blue, right scale) measured in the device of Fig. 4.7 for $V_g$=70 V at T = 0.35 K. Dashed horizontal lines show value of $h/\nu e^2$. Quantized plateaus of $\rho_{xy}$ and zero $\rho_{xx}$ are clearly observed for filling factors $\nu = 6$ and 10. Vertical arrows with numbers show LL fillings 14, 18, 22, 26, which can be identified in the SdHO of $\rho_{xx}$.

where $\rho(B, T)$ is the SdHO amplitude, $B_F = n_s \Phi_0 / g_{LL}$ is the frequency of the SdHOs in 1/B, where $\Phi_0 = h/e \approx 4.14 \times 10^{-11} T \cdot cm^2$ is the flux quantum and $g_{LL}$ is the LL degeneracy, and $\beta$ is the associated Berry's phase of the quasiparticles.

The decay of the magnitude of SdHOs with increasing charge density $n_s$, or decreasing magnetic field, is much faster than decay observed in monolayer or bilayer[11, 16, 43] (at least half a dozen oscillations were seen in similar measurements for the latter systems, while we can only reliably identify 3-4 in Fig.4.13). The simplest analysis of SdHOs is achieved by plotting positions of $\rho_{xx}$ minima and maxima as a function of $1/B$. The locations of $1/B$ for the $n$-th minimum and $n$-th maximum of $\rho_{xx}$, are plotted against Landau level index $n$ and $(n + 1/2)$, respectively. The so obtained Landau fan diagram is shown in Fig. 4.14.

The broken lines correspond to a linear fit, in which the slope indicates $B_F$ and $n$-axis interception provides a direct probe of Berry's phase $2\pi\beta$ in the magneto-oscillation. The slopes $B_F$ and interceptions $\beta$ as a function of $V_g$, are quantified in Fig.4.15 and 4.16, respectively. Linear fits of $B_F(n_s)$ in Fig.4.15 yield LL degeneracy $g_{LL} = 4\pm0.1$, with the definition of $B_F = n_s \Phi_0 / g_{LL}$, in perfect agreement with the expected valley and spin degeneracy. Similarly, the average $|\beta|$ or the interceptions in fan diagram Fig.4.14 is $\sim 1.5$. So Berry phase in Fig. 4.16 is $2\pi\beta = 2\pi \times (1.5 \pm 0.1) \approx 3\pi$. Hence, the step of $12e^2/h$ between the hole and electron gases across the $n$=0 LL, or the 12-fold degeneracy shown in Fig. 4.11 can be understood. A schematic illustration of the LL in ABC-stacked trilayer graphene is concluded in Fig.4.17, where the Hall conductivity $\sigma_{xy}$ appears at values of $\nu e^2/h$ with filling factors $\nu = 6, 10, 14, \cdots$, reflecting a unique 12-fold degenerate $n = 0$ LL and 4-fold spin and valley degenerate LLs with $n > 0$.
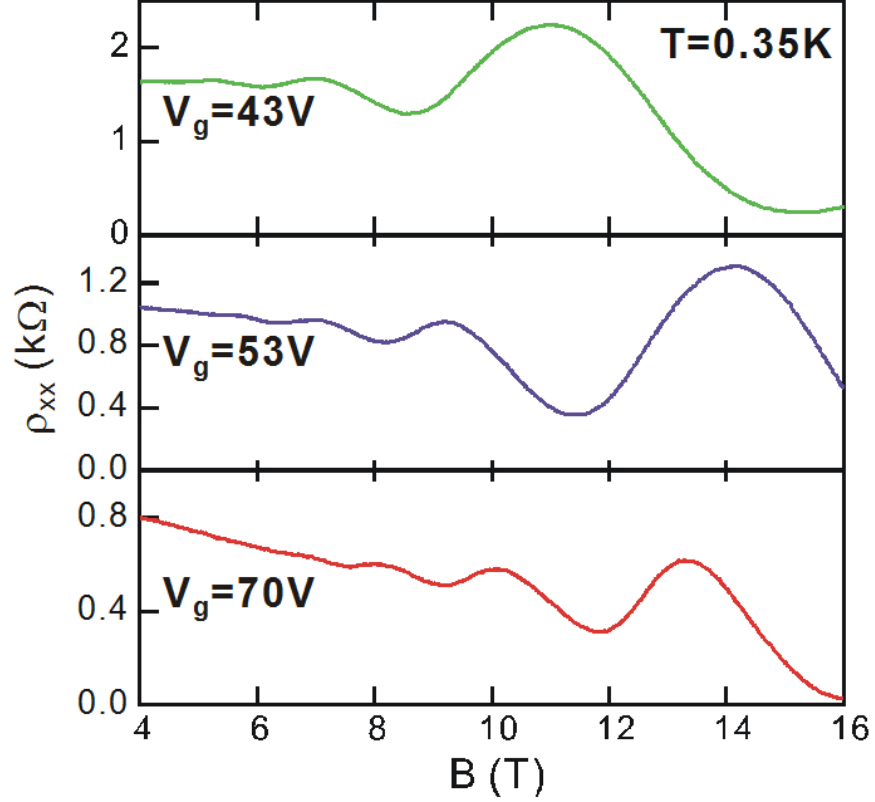
Figure 4.13: SdHOs as a function of magnetic field at different carrier concentrations. Positions of maxima and minima of $\rho_{xx}$ are determined by the frequency of SdHOs in $1/B$, $B_F = n_s h/(e g_{LL})$ ($g_{LL} = 4$ is the degeneracy of n-th Landau level when n>0), and by the Berry phase, which adds the overall shift with respect to $B_F$ and accounts for the peculiar high degeneracy of the n=0 LL arising at the band degeneracy point. Decay of the magnitude of SdHOs with magnetic field is governed by the cyclotron mass of charge carriers, $m_c$, which depends on their carrier concentration $n_s$, and the quantum scattering time $\tau_q$.
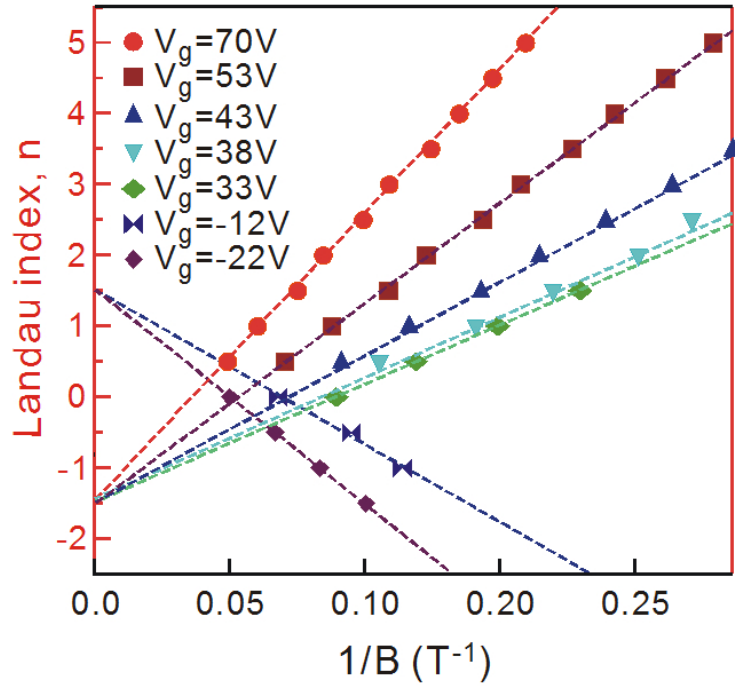
Figure 4.14: Fan diagram of SdHOs at different Vg. Values of 1/B for integer n correspond to n-th minimum, for semi-integers, n+1/2, to n-th maximum of $\rho_{xx}$(B), counting from n = 0 and B = $B_F$. The linear fit determines the slope, $B_F$, while the n-axis intercept, $\beta$, provides a direct probe of the Berry's phase, $2\pi \mid \beta \mid$, in magneto-oscillations measurement.
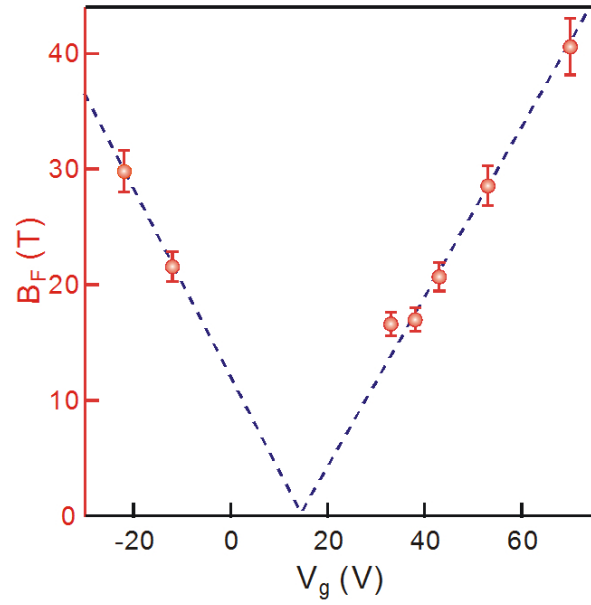
Figure 4.15: Dependence of $B_F$ on $V_g$, the error bars show standard deviation of the fitting. The dashed line is the linear fit of $B_F(V_g)$.
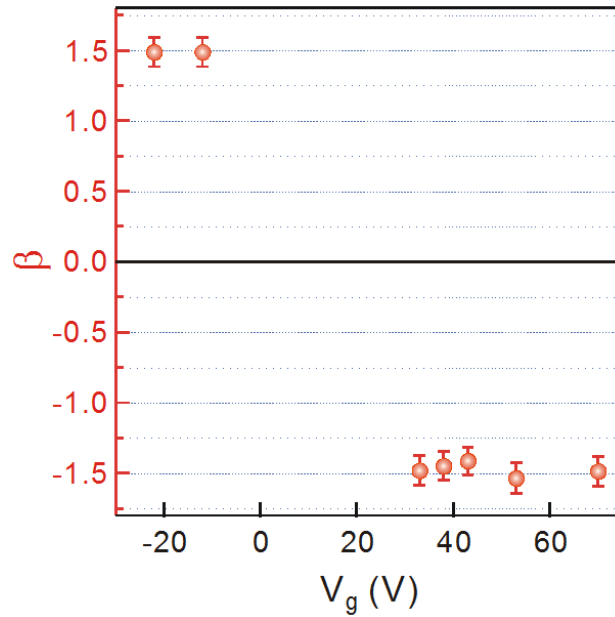


Figure 4.16: The phase shift of magneto-oscillations, $\beta$, as a function of $V_g$.
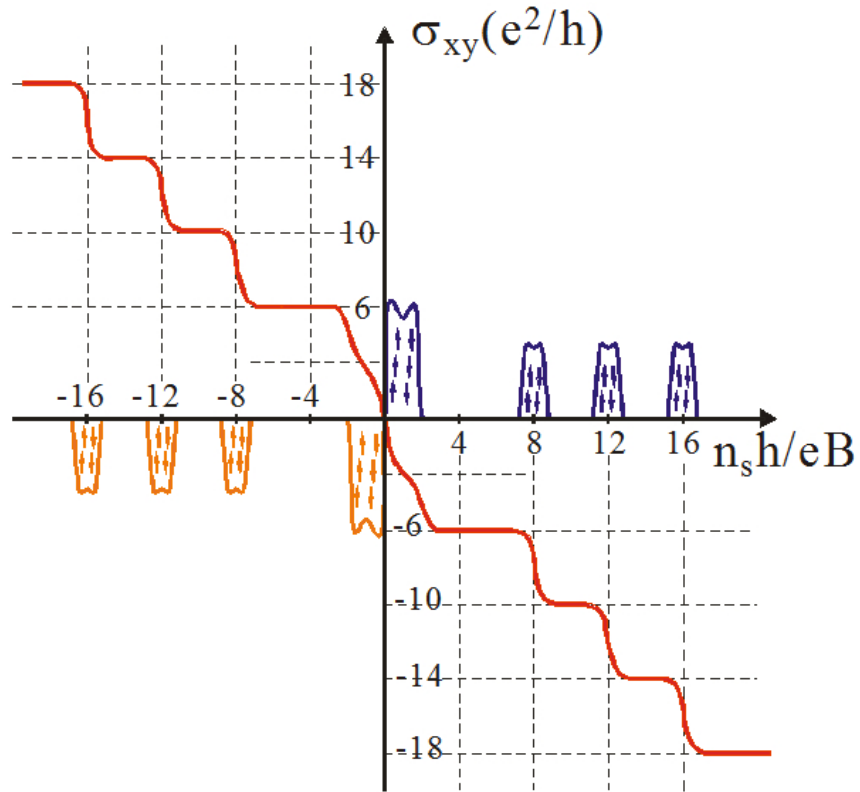
Figure 4.17: Schematic illustration of the Landau level density of states (DOS) in ABC-stacked trilayer graphene. Plateaus in Hall conductivity $\sigma_{xy}$ occur at values $\nu e^2/h$, where the sequence of filling factors $\nu = 6, 10, 14, \cdots$ reflects the unique nature of 12-fold degenerate $n = 0$ Landau level, and the fourfold spin-valley degeneracy of Landau levels with $n > 0$.

### 4.2.4 Conclusions

We have shown that chiral fermions exist in the ABC-stacked trilayer graphene and govern properties of the relativistic fermions, so they can be detected in experiments. These quasiparticles accumulate Berry's phase $3\pi$ along cyclotron trajectories and acquire unusual LL quantization in a magnetic field[21, 29, 33, 34]. Thus well quantized Hall conductivities of $\nu e^2/h$ with $\nu = 6, 10, 14, \cdots$ were observed. The $n$=0 Landau level has 12-fold degeneracy, however, the $n$ >0 Landau levels still maintain the 4-fold degeneracy as in monolayer and bilayer graphene. Our results provide experimental validation for recent theoretical works, and uncover possibilities for future studies.

# Chapter 5

# Scanning Photocurrent Study of Graphene

## 5.1 Introduction

Band bending and the associated spatially inhomogeneous population of Landau levels play a central role in the physics of the QHE by constraining the pathways for charge carrier transport and scattering[89]. Recent progress in understanding such effects in low-dimensional carrier gases in conventional semiconductors has been achieved by real-space mapping using local probes[90, 91]. Photocurrent, electron-hole pairs generated by incoming light and separated effectively by local electric field in the absence of external field, can be measured to reconstruct information about the local potential distribution and carrier transport pathways. By scanning the incoming light position on graphene and collecting the corresponding photocurrent in the quantum Hall regime, we measured spatially resolved photocurrent maps, which show that the net photocurrent is determined by hot carriers transported to the periphery of the graphene channel, where QHE edge states provide efficient

pathways for their extraction to the contacts. The photocurrent is sensitive to the local filling factor, which allows us to reconstruct the local charge density in the entire conducting channel of a graphene device.

Since the demonstration of the unusual half-integer quantum Hall effect (QHE) in graphene[11, 43], many related QHE experiments have been interpreted within the framework of edge-state transport[92–94], i.e., the backscattering-free flow of charge through edge-states[95] bounded by insulating barriers with incompressible electron densities[96]. Though compressible and incompressible electron densities have recently been observed in graphene[97], their role in shaping the QHE in graphene remains to be elucidated. Spatially inhomogeneous charge distributions due to unintentional charge impurity doping[98] are expected to be particularly pronounced in graphene and could cause deviations from pure edge-state transport.

## 5.2 Experimental

### 5.2.1 Device fabrication

For those experiments described in this chapter, devices were fabricated following the technique described in Sec.2.6, with extra precautions. Since the devices were used for spatially resolved measurement, which requires a surface area as large as possible, monolayer graphene flakes larger than $10 \times 20 \mu m^2$ were selected for device fabrication. Due to the large surface area, graphene flakes were easier to be broken in the process of resist spinning and metal liftoff. Thus slower ramping/accelaration in resist spinning was used, with a number of 1000rpm/s compared to 3000rpm/s for regular devices. During metal liftoff, devices were immersed in acetone on top of a hot plate (70°C) for two hours. If the metal film didn't liftoff naturally, tweezers were used to gently peel off the metal film.
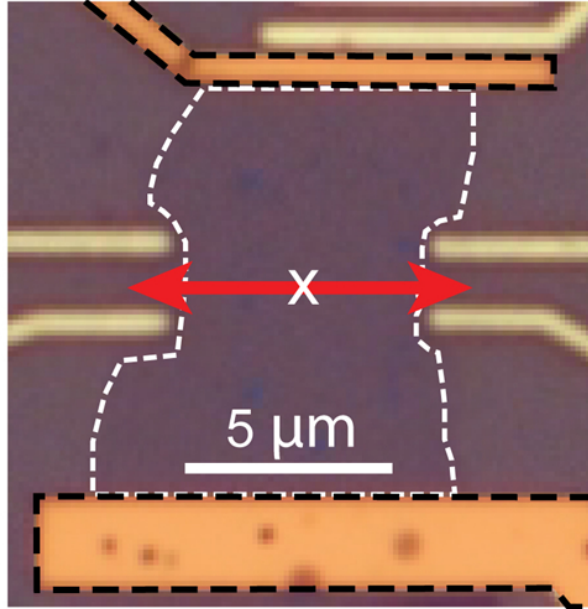
Figure 5.1: Optical image of the device. Dashed outlines mark the channel and the two connected electrodes. The four side electrodes are not in contact with the device.

## 5.2.2 Photocurrent measurement setup

Electrical transport and photo-transport experiments were carried out at 4.2 K in a Helium-4 cryostat with a variable-temperature insert, equipped with a superconducting magnet (up to 9 Tesla) and an integrated confocal optical microscope used to project a focused laser beam onto the graphene channel while measuring the electrical response between the source and drain electrodes (top and bottom contacts in Fig. 5.1) of the device. The side electrodes shown in Fig. 5.1 were not in contact with the device channel. Due to the low resistance of graphene devices, measurements of photovoltage (PV) were more appropriate than photocurrent (PC) for low-level signals. To avoid large signal-level variations between PV maps, we report PC data converted from PV measurements via $PC(V_G) = PV(V_G) \times G(V_G)$. We have also directly measured PC and found similar results. PV and PC measurements
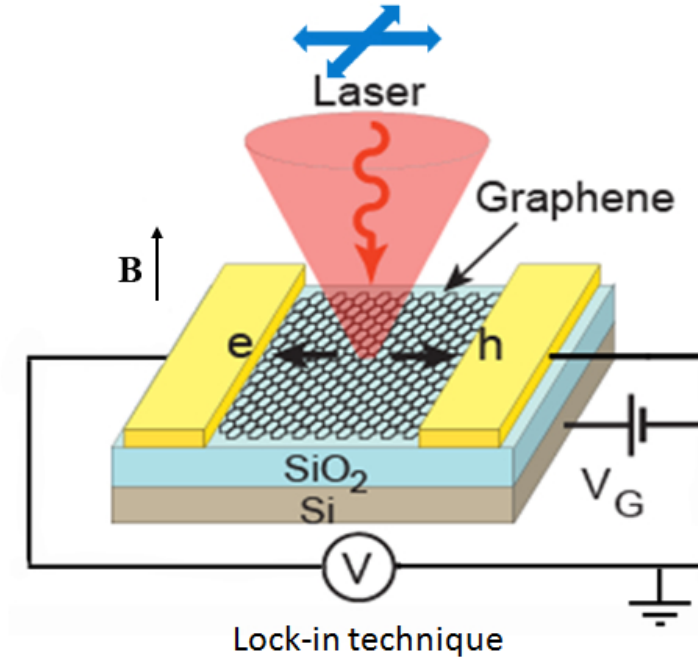
Figure 5.2: Schematic diagram of the photocurrent measurement.

were carried out by modulating the laser intensity at 2 kHz with an optical chopper, and feeding the frequency to a lock-in amplifier as reference to measure the low-level PV accurately. The laser wavelength was 650 nm, the power on the sample was 160 nW, and the spatial resolution was ~500 nm. Four devices were measured, showing similar behavior.

## 5.3    Results and discussions

The experiments were performed on monolayer graphene FETs at 4.2 K and in a magnetic field B up to ±9 T (Figs. 5.1, 5.2). In these conditions, as shown in Fig.5.3(a), the conductance of our device shows series of local extrema[65, 92, 94, 97, 99] associated with individual LLs,[99, 100] with maxima predicted to occur at quantized Hall conductances of 2, 4, 6, 10, and 14 $e^2/h$.[99, 100] The observed maxima are higher due to an inhomogeneous
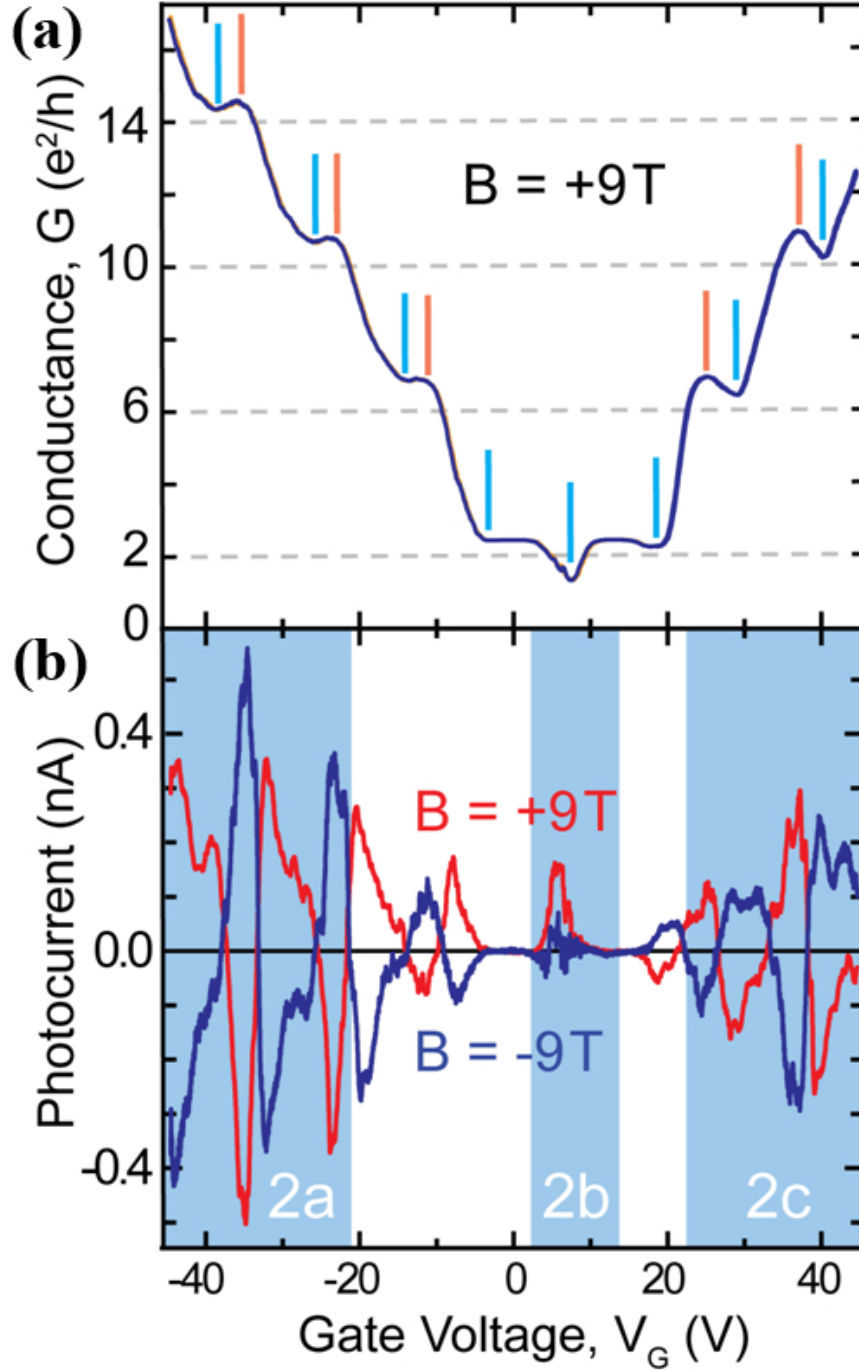
Figure 5.3: (a) Conventional two-terminal conductivity, G, as a function of gate voltage, $V_G$. Blue and red lines mark local conductivity minima and maxima. (b) PC measured with laser spot at the center of the graphene channel (cross in Fig.5.1) for B = ± 9 T. Shaded regions denoted "2a" to "2c" mark the different $V_G$ ranges in the sequence of PC maps of Fig.5.4.

filling factor distribution across the device, which will be explained later. The Dirac point is ∼7.5V in this device.

PC maps were obtained by scanning a focused laser across the graphene channel, and recording the two-terminal PC signal as a function of beam position. Previously, a similar approach has been used to investigate contact-induced band bending[101–104] and the photo-thermoelectric effect[105] in graphene at B = 0, as well as the electrostatics of the QHE in conventional semiconductor devices[106–108]. We observe that the $V_G$ dependent PC at fixed locations is oscillatory, with polarity determined by the direction of the magnetic field (Fig.5.3(b)). Such local oscillations are due to a recurring global PC distribution across the device, synchronous with the filling of consecutive LLs (Fig.5.4). While the patterns for n- and p-type doping and near the neutrality point differ, pairs of maps in the same columns of Fig. 5.4(a) and (c) show nearly identical spatial PC distributions. For specific carrier densities, e.g., $V_G$ = -45 V, -37.5 V, -33 V, -25.5 V, etc., we observe sharply delineated areas with PC response of the same polarity aligned roughly along the channel axis.

To further analyze these periodically recurring PC distributions, we consider the PC as a function of $V_G$ along a line across the graphene channel(Fig.5.5), as indicated in Fig.5.1 with red arrows. In a perpendicular magnetic field, the energy level spectrum of Dirac fermions in graphene comprises n- and p-type LLs, as well as a degenerate n = 0 level at the Dirac point (Fig.5.6)[43]. In the PC section of Fig.5.5, every LL except $n = 0$ is associated with a distinct "butterfly" pattern comprising four lobes of alternating polarity. The sign of the PC response changes abruptly on crossing the channel centerline, and on either side alternates with varying $V_G$. The patterns suggest that the energies of LLs are higher in the center than at the edges. This type of band bending has been observed in all tested devices, and similar band bending is likely to present in some degree in all graphene devices used in conventional transport experiments.
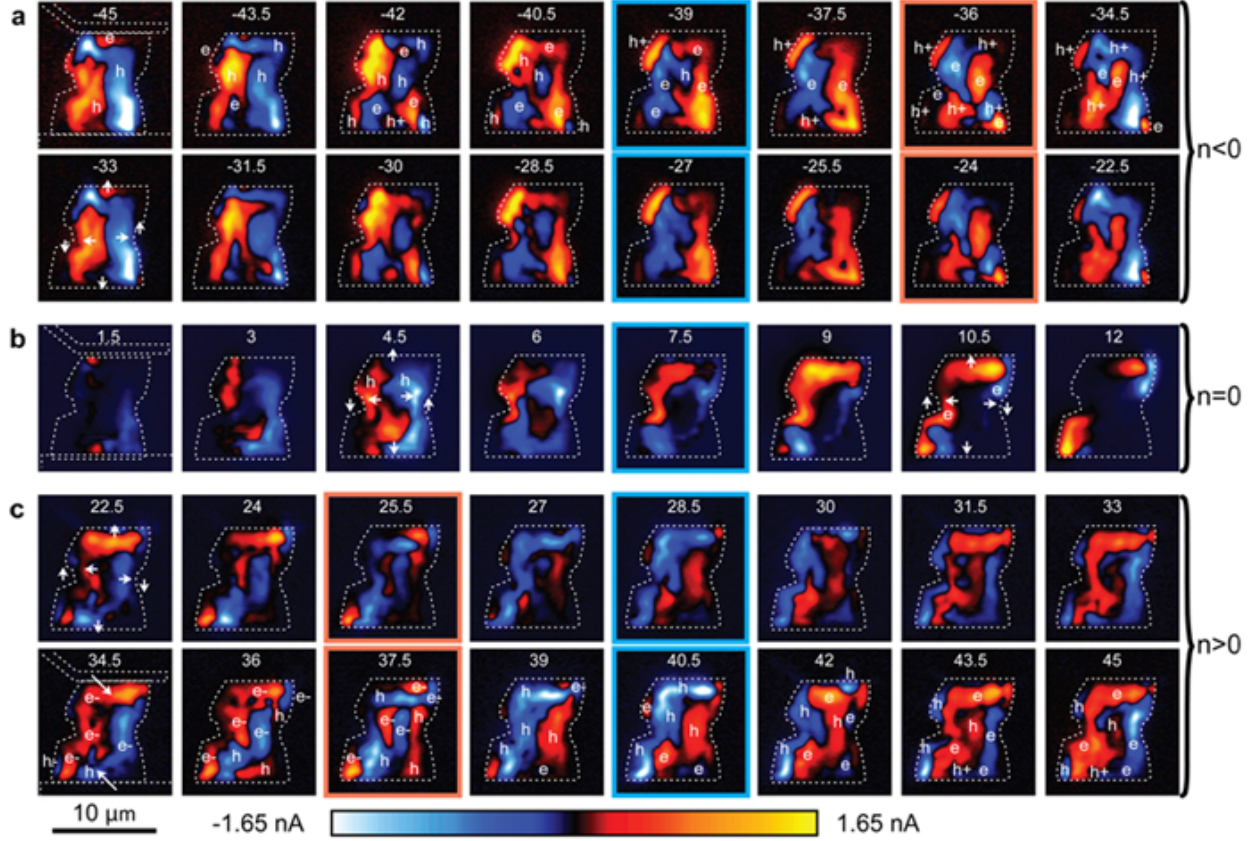
Figure 5.4: Spatial photocurrent maps for different gate voltages at B = 9 T. (a) PC maps of p-type Landau levels. (b) PC maps near the n = 0 Landau level. (c) PC maps of n-type Landau levels. Positive current corresponds to hole collection into the bottom contact of the device (Fig.5.1). Arrows in maps with $V_G$ = -33 V and +22.5 V show the prevalent directions of "hot" charge carrier transport in (a) and (c), respectively. Maps with blue (red) borders correspond to conductance maxima (minima) in Fig.5.3(a). In the top row of (a) and bottom row of (c), the predominant type of "hot" charge carriers for different regions are shown, where e and h denote electron and hole transport, and plus and minus signs stand for Landau levels (n+1) and (n-1). The outline of the maximum spatial extent of the PC signal is shown as a dashed contour in each panel.

81
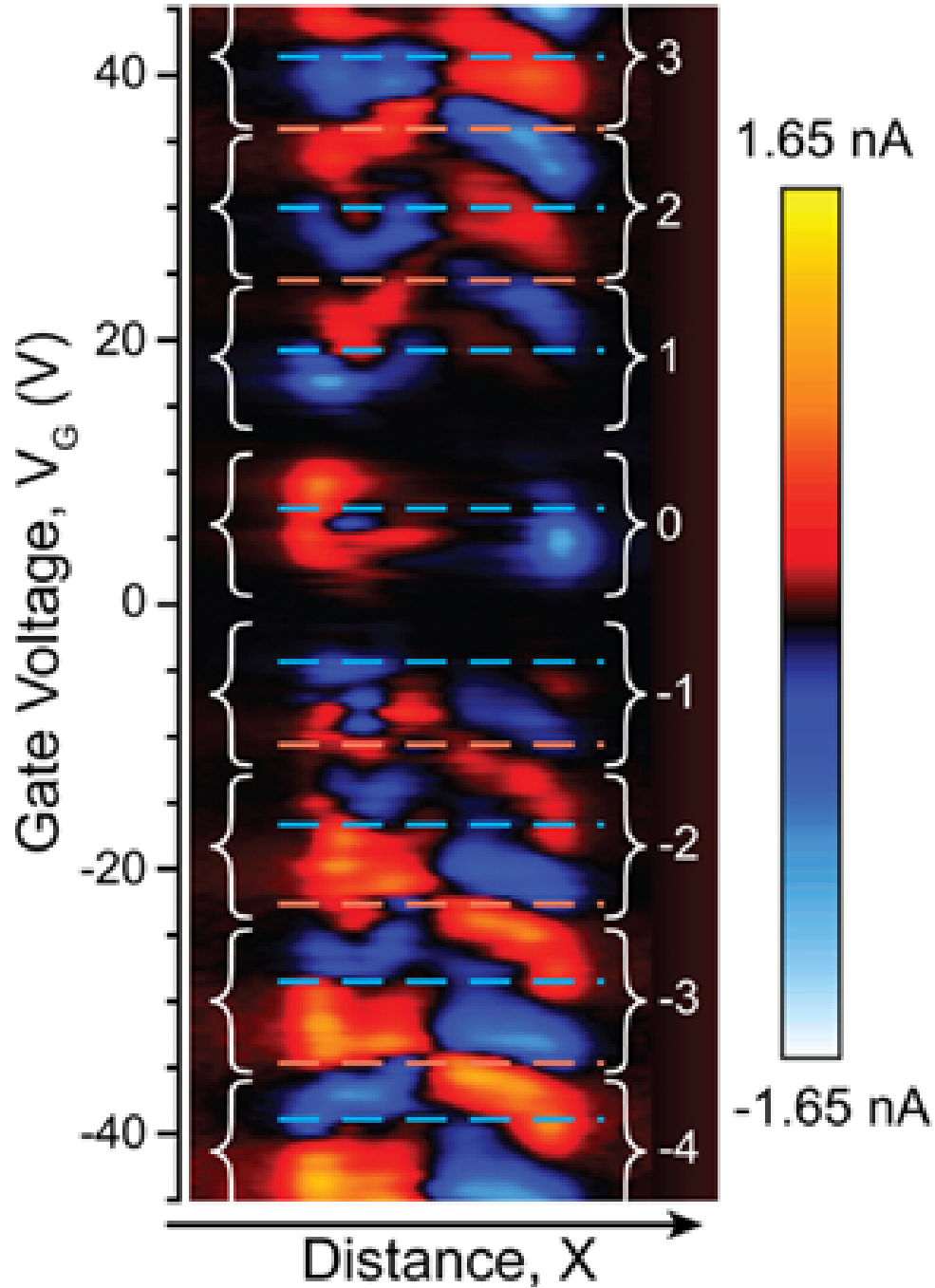
Figure 5.5: PC as a function of gate voltage along the arrow shown in Fig.5.1, extracted from 240 individual scans across the graphene channel for $V_G$ from -45 V to +45 V (B = 9 T). Dashed red and blue lines correspond to conductivity minima and maxima in Fig. 5.3(a). Braces indicate the $V_G$ ranges corresponding to individual Landau levels, numbered sequentially $n = 0, \pm 1, \pm 2, etc.$
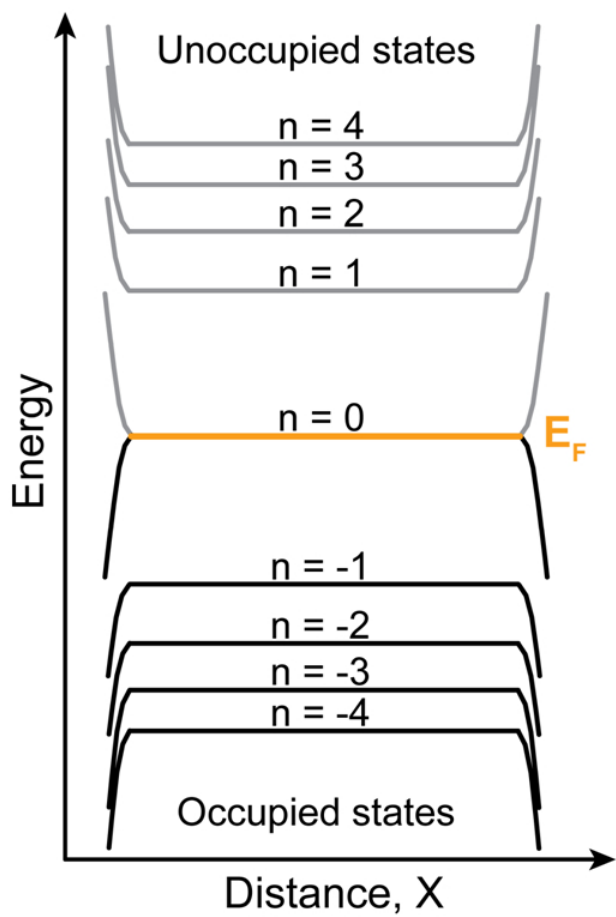
Figure 5.6: Landau levels in graphene. At the edges, the magnetic field bends levels with n > 0 (n < 0) upward (downward); the degenerate n = 0 level splits into two branches.

The butterfly patterns of Fig.5.5 can be understood by considering PC generation and collection in graphene in the QHE regime (Fig.5.7(a) and (b)). At our photon energy (1.9 eV), local light absorption excites an electron-hole pair to high-order LLs, followed by rapid relaxation and either recombination or charge transport. Due to screening of the electrical fields in the interior of the channel, the sensitivity of the PC to the magnetic field (Fig.5.3(b)) implies that carriers generated in the interior can reach the edges to be extracted to the contacts by edge-state transport. For the same carrier type, the currents carried at opposing edges are anti-parallel, with directions given by the vector product of the B-field and the gradient of the LL edge state band bending. Carriers that relax to the partially-filled LL at the Fermi energy, $E_F$, can propagate over long distances through the percolating conducting network formed by this LL in the presence of disorder, i.e., are extracted symmetrically at both edges and give zero net contribution to the PC. In contrast, intra-level relaxation of "hot" electrons (holes) in LLs not aligned with $E_F$ leads to transport involving states at the bottom (top) of the disorder-broadened levels, where localization effects are stronger compared to the LL at $E_F$[97]. The net PC due to these carriers is dominated by the edge closest to the point of illumination. This physical picture is analogous to the microscopy of photo- and electron-beam induced current in semiconductor devices[109, 110], where the net induced current reflects the transport of minority carriers. In the present case, both "hot" electrons and "hot" holes simultaneously act as "minority" carriers. The polarity of the net PC is determined by the type of hot carriers reaching the edges in larger numbers, which in turn depends on the local filling factor $\nu$ controlling the phase space available for relaxation to $E_F$. Indeed, for a nearly empty LL at $E_F$, the relaxation of hot electrons to this LL must be more efficient than that of holes, so that the latter prevail in the hot carrier transport. Conversely, for a nearly full LL at $E_F$ hot electrons will dominate the net PC. For high-order LLs, the transitions between "mostly hot-electron" and "mostly hot-hole" transport should

occur roughly at zero- and at half-filling of the individual LLs.

Using this picture of PC generation, we can explain the observed characteristic butterfly patterns. The schematics of Fig.5.8 illustrate the spatial PC distribution for two situations (at different $V_G$): one LL close to half-filling in the interior of the channel (Fig.5.8(a) – n-type LL; Fig.5.8(e) – p-type LL); and two LLs close to half-filling (Fig.5.8(b) – n-type LLs; Fig.5.8(f) – p-type LLs). This picture is analogous to the one developed in Ref. [111]. If, for instance, the n = 2 level forms a compressible, partially filled state spanning nearly the entire width of the channel, the charge density would rearrange itself to screen external potentials and disorder, leading to a non-uniform population of this LL across the device (Fig.5.8(a))[97]. According to the discussion in the previous paragraph, electrons dominate the PC when $\nu_2 > \nu_2^0$; holes prevail in areas with $\nu_2 < \nu_2^0$, where $\nu_2^0$ corresponds to the filling factor for which electron and hole hot carrier currents exactly compensate each other. This scenario indeed gives rise to a four-lobe pattern similar to that of Fig.5.5. One can readily generalize to a situation in which two n-type LLs intersect $E_F$ in the interior (Fig.5.8(b)), and to p-type LLs with downward edge band bending (Fig.5.8(e)(f)), all of which will give rise to similar butterfly patterns in the PC collection. The n = 0 LL at the neutrality point is an interesting special case. Here, Fig.5.5 shows only two lobes in the PC signal. In this regime, both the carrier type and band bending invert as the filling factor changes from $\nu < 0$ to $\nu > 0$, i.e., sweeping $V_G$ through the neutrality point does not alter the PC polarity (Fig.5.8(d)(h)). The net hot carrier current is always given by extraction to the closest edge channel, producing a two-lobe pattern around the centerline of the device.

By tracing the evolution of the PC signal with $V_G$ in Fig.5.5, we can now identify the type of hot carriers giving rise to the net PC response in every part of the device. We find that PC maps in Fig. 5.4(a)(c) corresponding to conductance minima involve a single LL close to half-filling over most of the device (Fig.5.8(a)(e)). Maps at the maxima show two different LLs
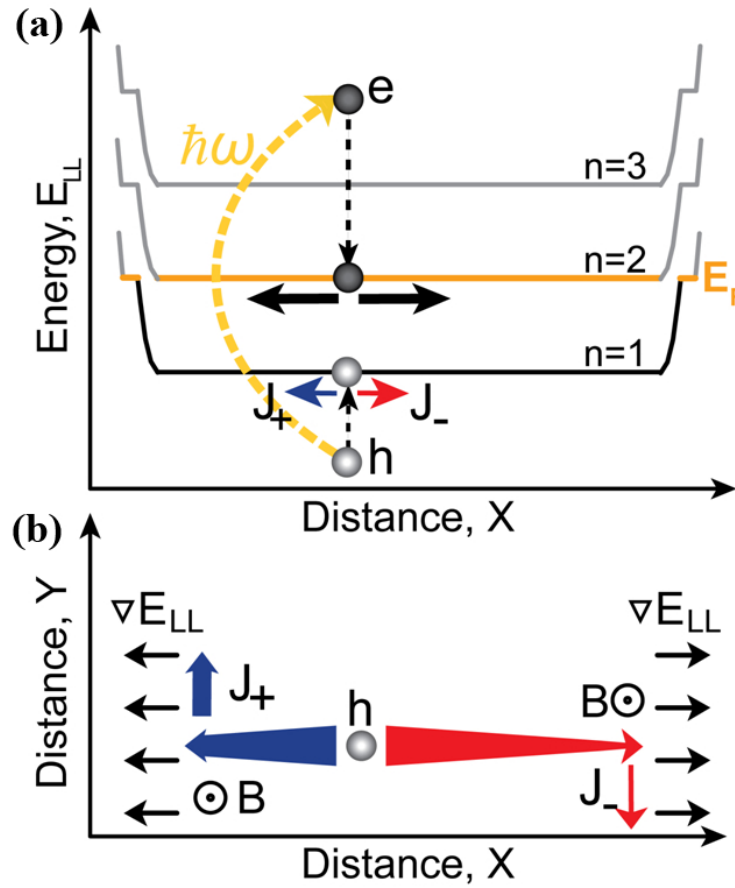
Figure 5.7: Illustration of PC generation and collection, assuming a partially occupied n = 2 Landau level. The level with n = 1 is fully occupied except at the edges where it forms a set of edge states. (a) Light absorption and electron-hole pair excitation. (b) Collection of "hot" carriers involving initial slow transport across the channel (X-direction) and subsequent fast transport via edge states (Y-direction). Arrow thicknesses indicate variations in current due to carrier relaxation to the Fermi level.
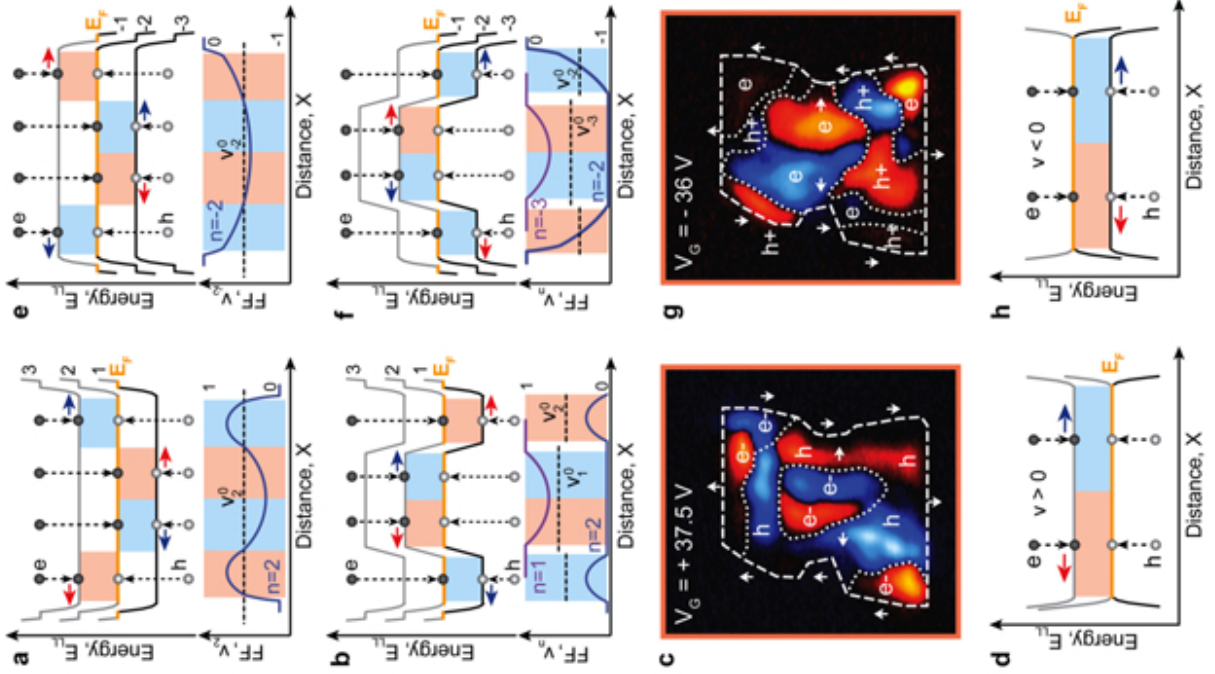
Figure 5.8: Carrier relaxation and PC collection in graphene devices in the QHE regime. (a) to (d) - Photocurrent collection for n-type doping. (a) Dominant pathways of charge carrier relaxation and collection across the graphene channel, for the case of one Landau level (here: n = 2) near $E_F$ inside the channel; and local filling factor $\nu_2$(FF) of this level across the device. Here and in all other panels, $\nu_n^0$ corresponds to the filling factor (of level n) for which electron and hole hot carrier currents exactly compensate each other. Colored rectangles connect the Fermi level with the Landau levels responsible for hot carrier transport; the color indicates the resulting PC polarity. (b) Same as (a) for the case of two Landau levels (n = 1, 2) at $E_F$ inside the channel, and local filling factors of these levels across the device. Schematics are not to scale. (c) Photocurrent map at $V_G = +37.5$ V. Approximate locations of the incompressible boundaries are shown as dotted contours. (d) Carrier relaxation and collection for the n = 0 LL near the neutrality point. (e) to (h) - Photocurrent collection for p-type doping. (e) One Landau level (n = -2) at $E_F$, and local filling factor $\nu_{-2}$ of this level across the device. (f) Two Landau levels at $E_F$ (n = -2, -3) inside the channel, and local filling factors of these levels across the device. Schematics are not to scale. (g) Photocurrent map at $V_G = -36$ V. (h) Carrier relaxation and collection for the n = 0 LL.

87

at $E_F$ in the center and at the periphery (Fig.5.8(b)(f)); the dividing boundaries, traced in the zoomed experimental maps of Fig. 5.8(c)(g), are expected to be incompressible[97], i.e., and form insulating barriers that profoundly affect the electrostatic landscape and current pathways in the device. In the conventional QHE, incompressible boundaries isolate counter-propagating currents in edge states[90, 91], reduce backscattering[112], and hence give rise to conductance quantization. Similarly, they affect the magnetoconductance in graphene channels with non-uniform potential. For n-type LLs (Fig.5.8(a) to (c)), the conductance in a graphene channel with inhomogeneous charge distribution not only comprises contributions of edge states, but also includes the bulk conductance of a LL near the periphery (areas marked "h" in Fig. 5.8(c)), which also couples to the contacts. This bulk contribution causes the overall conductance to exceed the expected quantized values. For p-type LLs, Fig.5.5 shows that the induced positive charge density is always highest in the center of the device. The LL crossing $E_F$ inside the channel does not form edge states (Fig.5.8(e) to (g)), but it can suppress backscattering between edge states at opposite sides of the channel. The reduced backscattering together with the bulk conductance of this LL (through areas marked "e" in Fig. 5.8(g)) again causes G maxima higher than the expected quantized conductance values for this branch of the conductance curve.

## 5.4   Summary and future work

The unique geometry of a two-dimensional carrier gas confined close to the surface makes graphene particularly suitable for scanning probe experiments. The advantage of the presented PC-based approach is the capability to map not only the charge density, which could be determined by other scanning probe methods, but also the carrier propagation in graphene in the QHE regime. Based on the analysis of the photocurrent collection mechanism in

graphene in the presence of high magnetic fields, our results demonstrate the formation of counter-propagating edge states, with direction of propagation determined by the unique LL spectrum of graphene and the LL bending at the edges of the channel. Further, we observe the interplay between bulk and edge state conduction due to inhomogeneously populated Landau levels, a situation commonly found in graphene devices that gives rise to deviations from exact conductance quantization. The present approach is well suited for more detailed investigations of the QHE physics in graphene, including electrostatics and current pathways in externally biased devices and the effects of local disorder and contact-induced band bending. Finally, our method could be used to probe carrier transport and the QHE in high-mobility suspended graphene devices[38, 39], giving access to phenomena that cannot be measured by conventional two-probe magnetotransport experiments.

# Chapter 6

# Electronic and Optoelectronic Study of $(GaN)_{1-x}(ZnO)_x$ Solid Solution Nanowires

## 6.1 Introduction

Solid solutions of gallium nitride (GaN) and zinc oxide (ZnO) have emerged as promising photocatalysts for water splitting driven by visible light[27, 113]. Although GaN and ZnO are semiconductors with comparable bandgap energies ($\sim$3.3 eV) that correspond to the ultraviolet (UV) region of the electromagnetic spectrum, the bandgap of their $(GaN)_{1-x}(ZnO)_x$ solid solution has been predicted to be as small as 2.29 eV, that is, well in the visible region of the spectrum[114]. Experimentally, bandgaps in the 2.8–2.4 eV range have been found, for $0.05 < x < 0.42$[27]. Such a significant bandgap reduction makes it now possible to prepare materials that capture a larger fraction of the incident solar spectrum than traditional photocatalysts, for instance, $TiO_2$. However, very little is known about the electrical

properties of $(GaN)_{1-x}(ZnO)_x$, even though quantities such as charge carrier concentration, carrier mobility, and charge trap density are essential to understand catalytic behavior and optimize photocatalytic activity. The correlation between electronic and catalytic properties is best established when working with single-crystal catalysts with well-defined geometry.

Nanostructuring a catalyst can in principle be advantageous to further accelerate chemical reactions. Nanostructured semiconductors have larger interfacial surface areas than their bulk counterparts and often show more efficient electron-hole pair separation and shorter electron-hole diffusion lengths to the surface[115]. Besides, by varying the characteristic size of nanostructures, their optical and electrical properties can be tailored to optimize light absorption and energy transfer. When nanostructured, photocatalysts can also show larger polarizability and water wettability than in bulk[116]. An ideal photocatalyst is then a nanostructured single-crystal material that efficiently absorbs visible light and induces large chemical activity.

With the ultimate goal of producing such a catalyst, we have used a new method to synthesize highly uniform $(GaN)_{1-x}(ZnO)_x$ solid-solution single-crystal nanowires with $x \sim 0.12$. When properly gated, the nanowires showed field-effect transistor (FET) behavior, from which the background electron density and mobility were deduced. Photocurrent measurements yielded an energy bandgap for the nanowires of $\approx 2.7$ eV and revealed the effects of charge traps.

## 6.2  Experimental

### 6.2.1  Synthesis of $(GaN)_{1-x}(ZnO)_x$ solid solution nanowires

$ZnGa_2O_4$ nanoparticles were used as a precursor material for the growth of $(GaN)_{1-x}(ZnO)_x$ solid solutions and were prepared in this way: mixtures of gallium nitrate hydrate (12.8 g) and zinc acetate dehydrate (5.6 g) in ethanolamine solution (6 ml) were heated at 65 °C for 1 h and subsequently aged at 0 °C for one week. Sintering the resulting gel-like precursor material (400 °C, 1 hr) produced a final $ZnGa_2O_4$ precursor composed of crystallites with 3.2 nm average size, as measured by x-ray diffraction and high-resolution transmission electron microscopy (HRTEM). Next, the $ZnGa_2O_4$ nanoprecursor was placed in a quartz tube located in the hot zone of a tube furnace. Ammonia (flow rate of 100 $cm^3/min$) was used as the nitrogen source and as the carrier gas. Cleaned Si $\langle 110 \rangle$ substrates were coated with a 2 nm Au layer using a 230-mesh hexagonal copper grid as a mask during Au deposition. The patterned Au-coated Si substrate was placed downstream of the gas flow at about 1 cm away from the source material. The temperature of the reaction was held at 900 °C for one hour, and then lowered to 20 °C.

### 6.2.2  Microstructural characterization

A JEOL-2100F microscope, operated at 200 kV and equipped with energy-dispersive X-ray spectroscopy (EDS) and electron energy loss spectroscopy (EELS), was used to determine the nanowires' shape, size, composition, and structure. Scanning electron microscopy (SEM) images were obtained on a Hitachi S-4800 with a field-emission gun, using samples taken directly from the substrate. For the HRTEM measurements, samples were removed from the Si substrate by sonicating it in an ethanol solution.

### 6.2.3   Preparation and electrical characterization of nanowire FET devices

Individual nanowires were ohmically contacted by metallic electrodes (50 nm Ti/50 nm Au, defined by electron-beam lithography and electron-beam evaporation, similar to process in Sec.2.6) and electrostatically coupled to the underlying silicon substrate (0.01 $\Omega \cdot cm$) through a 200nm thick $Si_3N_4$ dielectric layer. Nanowire devices were completed with a 400 °C anneal in nitrogen to reduce the source/drain contact resistance. The two-terminal current-voltage $(I_D - V_D)$ characteristics of a single nanowire FET device for various gate voltages $(V_G)$ was measured with a semiconductor parameter analyzer (Agilent HP 4156C). A non-gated $(V_G = 0)$ device biased at a constant source/drain voltage was illuminated with light produced from a UV lamp (power density $\sim 3 \ mW/cm^2$) or from a xenon-arc lamp equipped with a monochromator (output power density: 40 to 56 $\mu W/cm^2$, depending on the wavelength).

## 6.3   Structure and composition analysis

Typically, $(GaN)_{1-x}(ZnO)_x$ solid solutions are synthesized by nitriding either a mixture of submicron-sized $Ga_2O_3$ and ZnO, or $ZnGa_2O_4$[27]. The size of the resulting $(GaN)_{1-x}(ZnO)_x$ particles reflects that of the precursor material[27]. By preparing ultra-small $ZnGa_2O_4$ nanoparticles ($\sim$ 3.2 nm) via a sol-gel process and using them as Ga-Zn-O precursor, we have been able to synthesize nanowires as long as 20 $\mu m$ and with uniform diameters ranging from 30 nm to 100 nm, and the SEM images are shown in Figs.6.1(a) and (b). When the size of $ZnGa_2O_4$ precursor is larger, in submicron range, or a mixture of GaN and ZnO powders were used as precursors, no nanowires were obtained. The ultra-small size of the
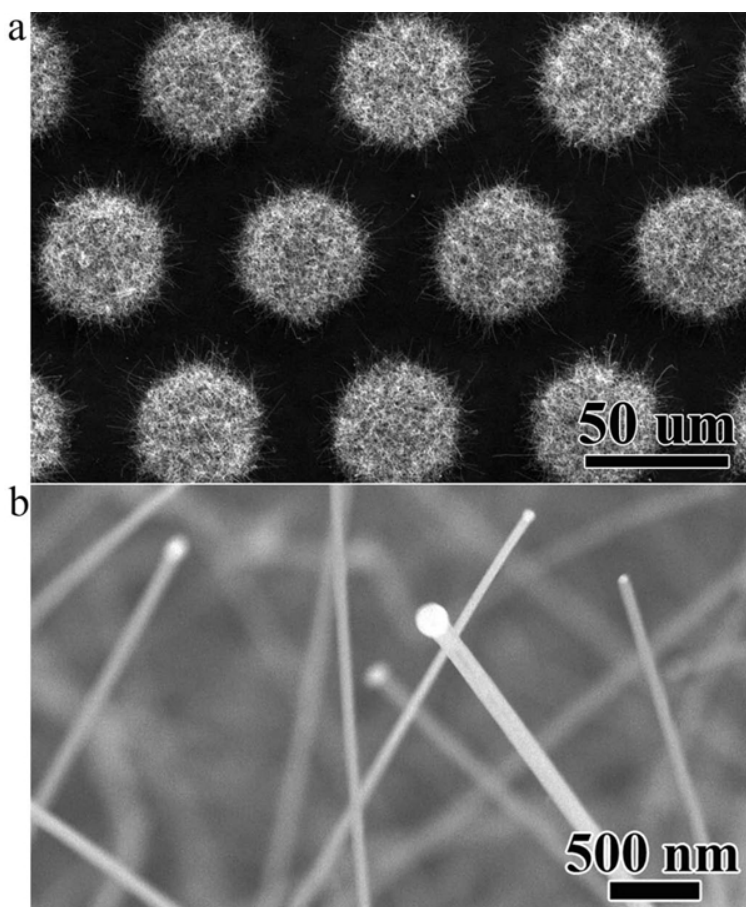
Figure 6.1: (a) Low-magnification SEM image of patterned nanowires; (b) high-magnification SEM image of nanowires, showing Au nanoparticles at their tips.

$ZnGa_2O_4$ precursor ensures the efficiency of its thermal evaporation in the temperature range that is adequate for nanowire growth and without excessive volatilization of $Zn^{2+}$.

HRTEM revealed the crystalline structure and the chemical composition of individual nanowires. High magnification images and their corresponding fast-Fourier-transform electron-diffraction patterns showed the nanowires to be single crystals with an hexagonal wurtzite structure and with their long axis along the [100] crystal direction as shown in Figs.6.2(a)-(c).

94
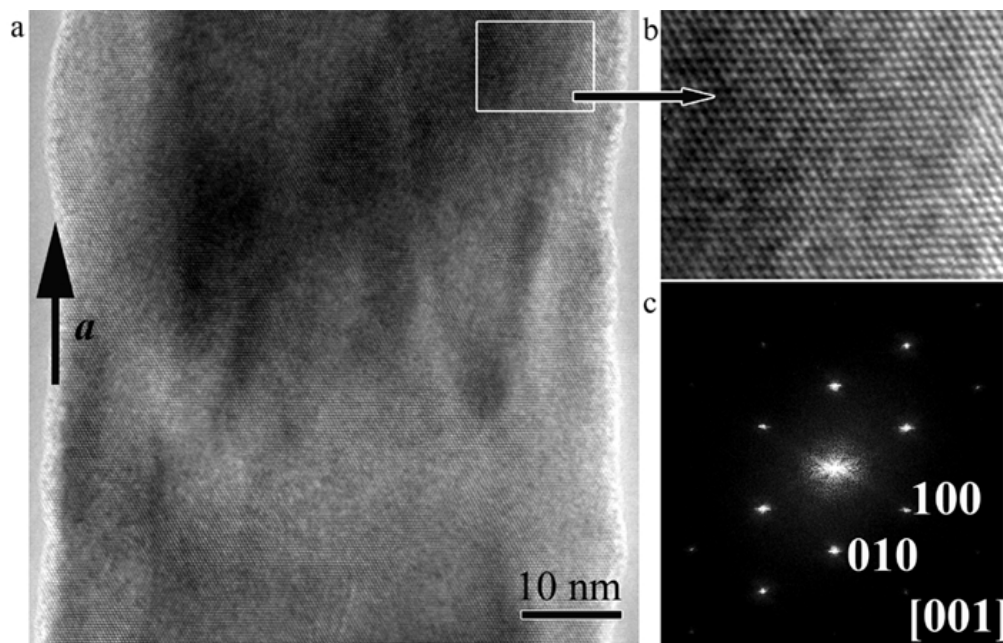
Figure 6.2: (a) High-magnification TEM image of a longitudinal section of a nanowire; (b) enlarged image of the small rectangular area indicated in (a); (c) fast-Fourier-transform electron diffraction pattern from a large area of the nanowire.
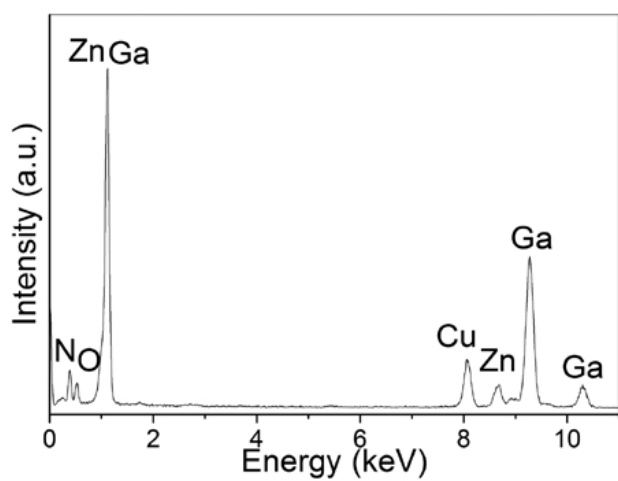


Figure 6.3: EDS spectrum taken from a large region of the nanowire.
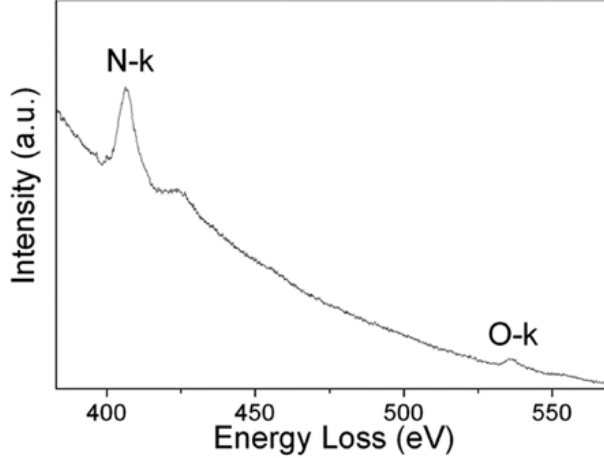
Figure 6.4: EELS spectrum taken from the same part of the nanowire as in Fig.6.3.

EDS showed that the nanowires are composed of Ga, Zn, N, and O, with Zn/(Zn+Ga) and Ga/N atomic ratios of 0.12 and ~1, respectively (Fig.6.3). The 0.12 ratio is almost three times smaller than the corresponding one (0.33) in the $ZnGa_2O_4$ precursor, which is consistent with reduction and volatilization of $Zn^{2+}$ found during the processing of $(GaN)_{1-x}(ZnO)_x$ powders[27]. EELS measurements also yielded a value of $\sim 0.12$ for the O/(N+O) atomic ratio, so that the nanowire composition was unambiguously determined to be $(Ga_{0.88}Zn_{0.12})(N_{0.88}O_{0.12})$.

EDS spectra showed that the single spherical particles located at the tip of each nanowire are composed of Au, with small amounts of Ga and Zn. This, combined with selective wire growth from patterned Au catalysts, suggests a vapor-solid-liquid growth mechanism[117], similar to that previously reported for GaN nanowires grown from iron catalysts[118], wherein liquid Au clusters at elevated temperature catalyze reaction between Ga-Zn-O and N radical vapors originating from reduced $ZnGa_2O_4$ nanoclusters and decomposed ammonia, resulting in axial growth of solid solution nanowires.
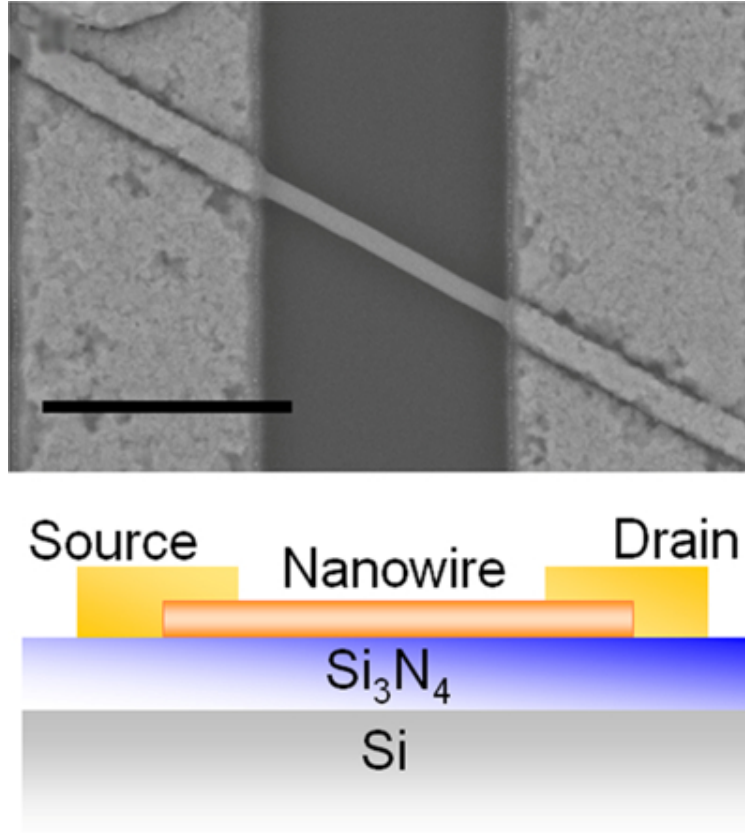
Figure 6.5: Scanning electron microscope image of a typical $(Ga_{1-x}Zn_x)(N_{1-x}O_x)$ nanowire FET, and a corresponding schematic diagram of its lateral profile. The scale bar is 1 $\mu m$.

## 6.4 Electrical properties of $(Ga_{0.88}Zn_{0.12})(N_{0.88}O_{0.12})$ FET

The electrical properties of the nanowires were determined by analyzing the current-voltage characteristics of back-gated FETs fabricated from individual wires (Fig.6.5). Consistent with n-channel operation, the current ($I_D$) of the FET shown in Fig.6.5 increased with increasing gate voltage ($V_G$) for positive source/drain bias ($V_D$)(Fig.6.6). Upon changing $V_G$ from -15 to +5 V, the conductance increased a thousand times, to 1 $\mu S$ (inset in Fig.6.6), which, given the dimensions of the nanowire, corresponds to a resistivity of $\sim 0.3$ $\Omega \cdot cm$.
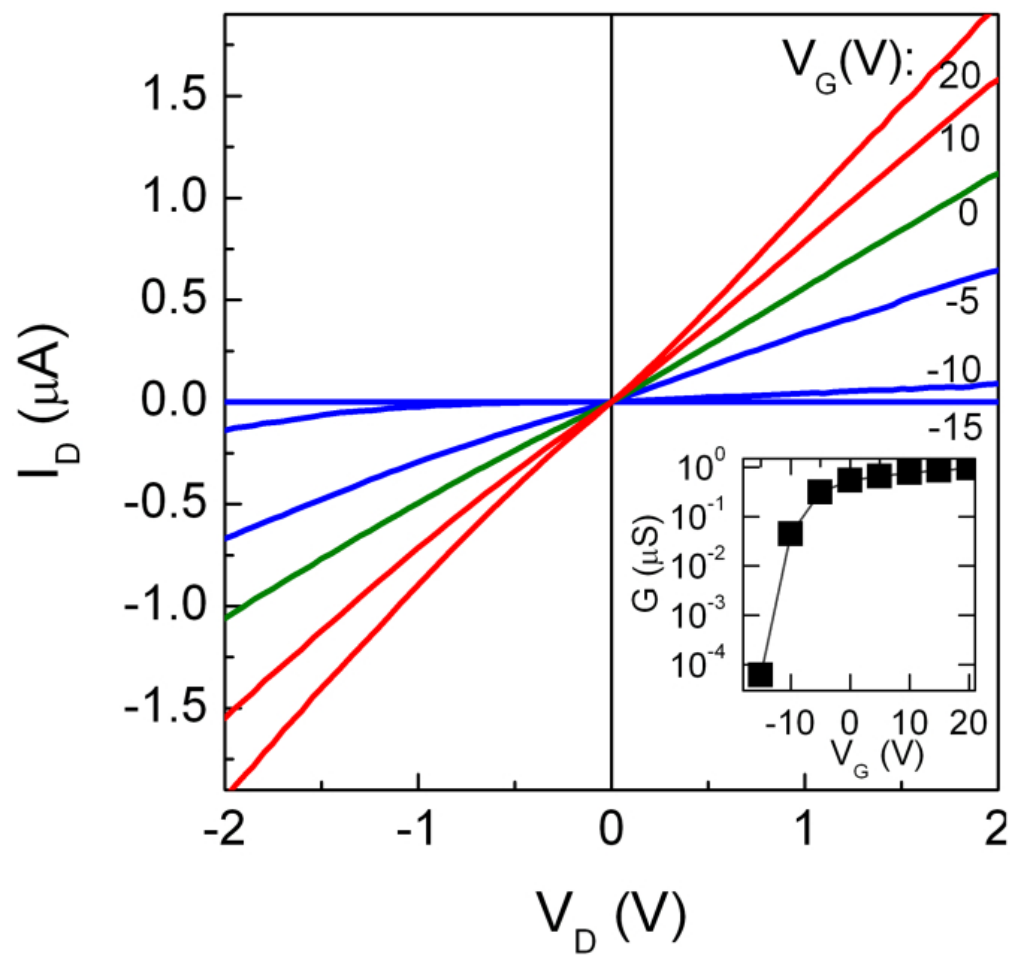
Figure 6.6: Gate-dependent $I_D - V_D$ characteristics of a $\sim$70 nm diameter nanowire for several gate voltages, from +20 V to -15 V. Inset: plot of the conductance versus gate voltage.
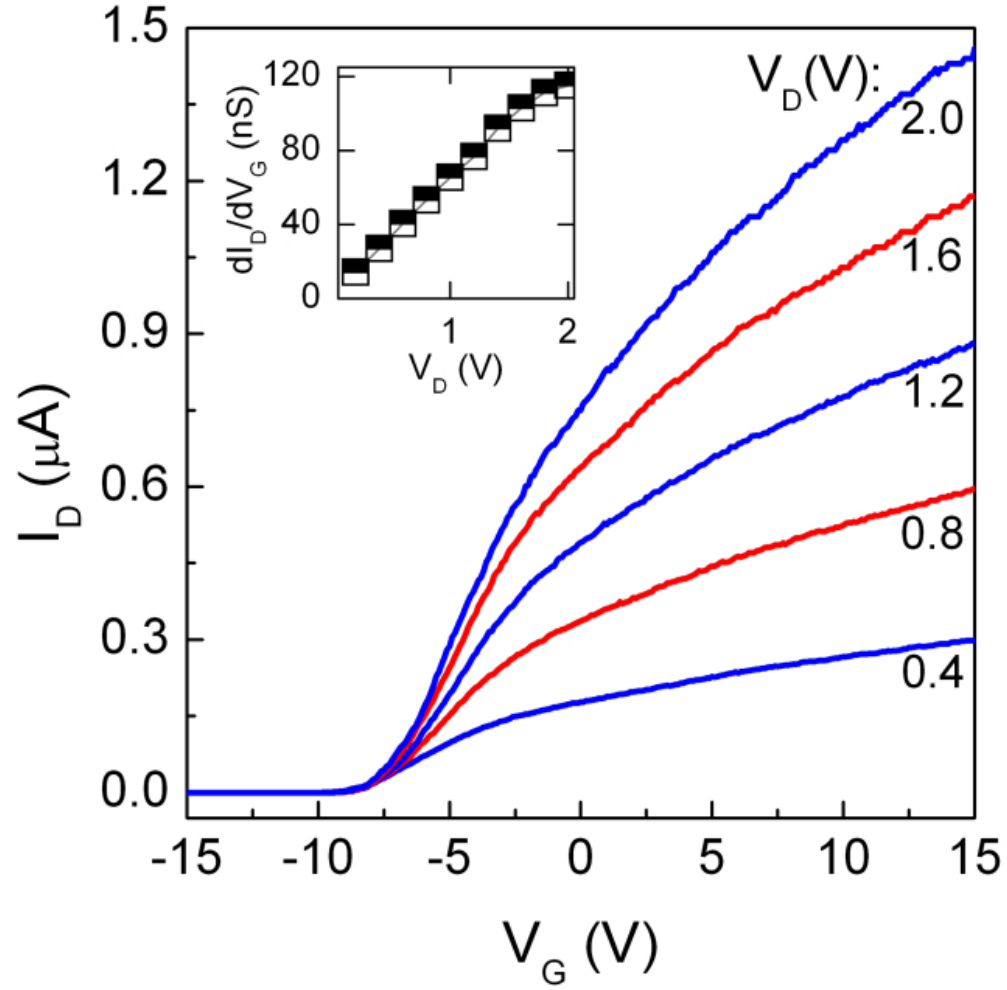
Figure 6.7: $I_D - V_G$ curves recorded for $V_D$ from 0.4 V to 2.0 V (curves with $V_D$=0.2, 0.6, 1.0, 1.4 and 1.8V are not shown for figure simplicity). The inset shows transconductance $dI_D/dV_G$ versus $V_D$, and the transconductance is calculated by fitting the linear region of $I_D - V_G$ curve soon after the device was turned on.

The transfer characteristics ($I_D - V_G$) provided information about the free-carrier concentration and charge mobility of the nanowire (Fig.6.7). The threshold voltage ($V_{Th}$) for full depletion (-8V for the device of Fig.6.5) is related to the nanowire's electron carrier concentration ($N_e$) through the geometric capacitance (C) between the wire and the conducting substrate[119, 120]:

$$N_e = \frac{C|V_{Th}|}{e\pi r^2 L} \approx \frac{2\epsilon_0 \epsilon_r |V_{Th}|}{er^2 ln(2h/r)} \tag{6.1}$$

where e and $\epsilon_0$ are fundamental constants, r and L are the nanowire's radius ($\sim$35 nm) and length ($\sim$1.5 $\mu m$), respectively, and h and $\epsilon_r$ are the thickness (200 nm) and relative permittivity ($\sim$7.5) of $Si_3N_4$, respectively. Equa.6.1, which treats the wire as an infinitely long cylinder, yields $N_e \sim 1 \times 10^{19} cm^{-3}$, a value that is comparable to those previously reported for unintentionally-doped GaN nanowires[119]. Likely dopants are nitrogen vacancies or oxygen atoms incorporated during wire growth[119, 121], and/or from the incorporation of ZnO in the solid solution.

At low $V_D$, the device's transconductance ($dI_D/dV_G$) is proportional to both $V_D$ and the electron mobility ($\mu$) in the nanowire[120]:

$$\frac{dI_D}{dV_G} = \mu \frac{C}{L^2} V_D \approx \mu \frac{2\pi \epsilon_0 \epsilon_r}{L ln(2h/r)} V_D \tag{6.2}$$

From the slope of $dI_D/dV_G$ versus $V_D$ (inset to Fig.6.7), we estimate an electron mobility $\mu \sim 1.0 cm^2/V \cdot s$, which is considerably smaller than that previously reported for GaN nanowires (150-650 $cm^2/V \cdot s$)[119] and ZnO nanowires (17 $cm^2/V \cdot s$)[122] with similar carrier concentrations. In a solid solution formed by isoelectronic substitution of atoms in a parent material, long-range lattice order and the type of chemical bonding are preserved, and the main features in the electronic band structure of the host remain largely unchanged.

In contrast, in a solid solution like $(GaN)_{1-x}(ZnO)_x$, where there is a non-isoelectronic substitution of $Zn^{2+}$ for $Ga^{3+}$ and of $O^{2-}$ for $N^{3-}$, chemical bonding changes and disorder increases[123]. This, in turn, may generate local fluctuations of the elemental molar fraction and lead to local changes in the energy bands and effective mass of charge carriers[123], which reduce electron mobility.

Another contribution to the low mobility may come from charge traps originating from the substitution of Zn for Ga in the $(GaN)_{1-x}(ZnO)_x$ solid solution. When added to GaN as a substitutional impurity in concentrations above $10^{19} cm^{-3}$, Zn is known to create deep midgap acceptor-levels $\sim$ 0.7-1.4 eV below GaN's conduction band edge[124, 125]. In our $(Ga_{0.88}Zn_{0.12})(N_{0.88}O_{0.12})$ nanowires, the equivalent concentration of Zn is $\sim 10^{21} cm^{-3}$, which is more than enough to create a considerable number of deep charge traps that hinder electronic mobility.

## 6.5  Light decay and optical bandgap in $(Ga_{0.88}Zn_{0.12})$ $(N_{0.88}O_{0.12})$ nanowires

The time dependence of the device's response to light supports the existence of those traps in the nanowire's channel. When illuminated with a 365 nm UV lamp ($\sim 3 mW/cm^2$), the nanowire FET exhibited a photocurrent ($I_{Light}$) that increased slowly, and then saturated after $\sim$ 150 seconds (Fig.6.8). Similarly, after the light was switched off the photocurrent decayed very slowly, requiring more than 2000 seconds to return to the dark current value ($I_{Dark}$) (Fig.6.8). Such behavior suggests a strong influence from charge traps on the generation and recombination of photo-excited free carriers[126].

The dynamics of the photocurrent decay gives information about the distribution of trap
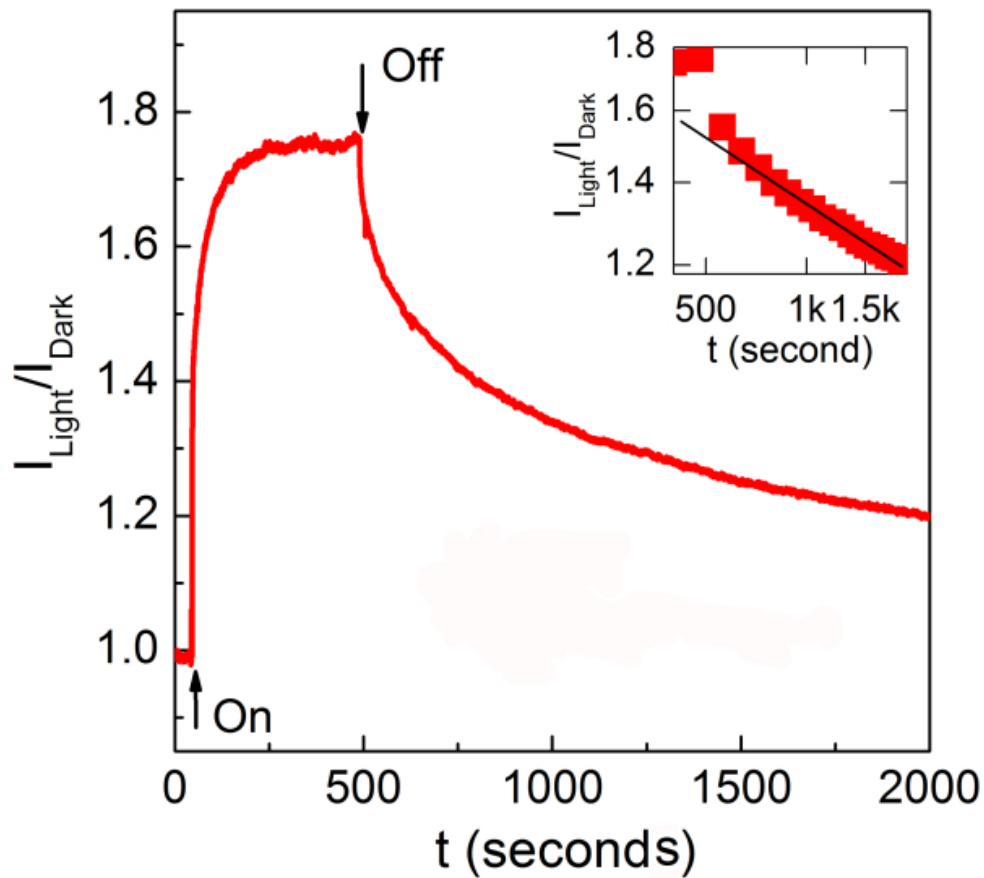
Figure 6.8: Photocurrent response ($I_{Light}/I_{Dark}$) versus time t of a nanowire FET under $V_G$ = 0 V and $V_D$ = 2 V. A 365 nm UV light was turned on at t = 40 s and switched off at t = 490 s. Inset: log-log plot for the time dependence of the photocurrent decay.
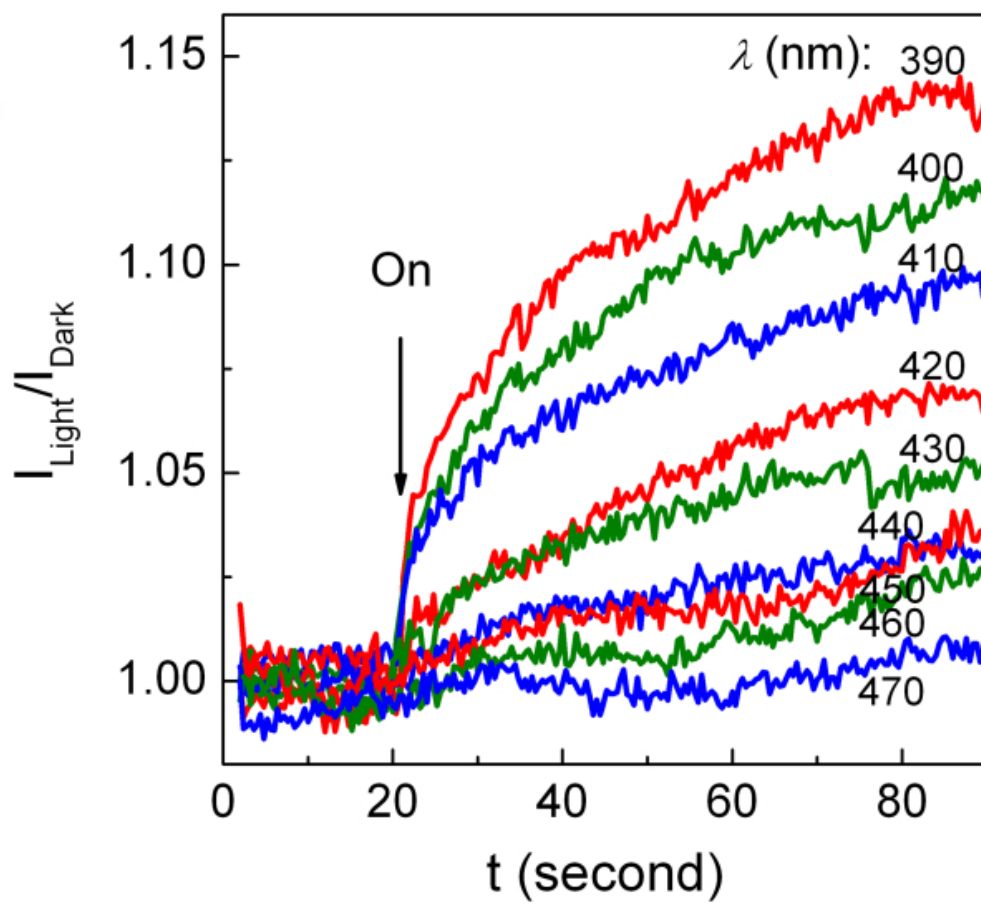
Figure 6.9: Photocurrent response under various incident light wavelengths ranging from 390 nm to 470 nm. Light was turned on at t = 20 s.

states. A high density will significantly retard charge recombination, primarily through repeated charge trapping and detrapping processes, and lead to a photocurrent decay with a power-law time dependence[127, 128],

$$I_{Light} \propto t^{-\alpha} \tag{6.3}$$

where $\alpha$ is a constant whose value depends on the specific distribution of charge trap energies. This is in contrast with an exponential dependence, characteristic of decay by direct electron-hole recombination. For times longer than $\sim$200 sec after illumination is turned off, the photocurrent of our nanowire shows a power-law behavior (Fig.6.8 inset, $t > 700 sec$) with $\alpha \sim 0.16$. At earlier times, the decay cannot be explicitly described by either a single power law or a single exponential, which suggests that initial decay may have been affected by shallow trap levels with multiple exponential distributions.

As expected, the strength of the photoresponse depended on the wavelength ($\lambda$) of the illumination. As shown in Fig.6.9, the magnitude of the photocurrent continuously declines to near zero as $\lambda$ increases from 390 nm to 470 nm (from a xenon arc lamp equipped with a monochromator). From that dependence we have estimated the bandgap energy of the $(Ga_{0.88}Zn_{0.12})(N_{0.88}O_{0.12})$ nanowires. As seen in Fig.6.10, the photocurrent increases monotonically with decreasing $\lambda$, from almost zero at $\lambda$ = -470 nm to a value that at $\lambda$ = 390 nm (normalized by illumination intensity) represents 15% of the dark current. From this dependence, we estimate a band gap energy in the range of $\sim$ 2.76 - 2.64 eV, which is consistent with previously reported bandgaps of 2.75 eV and 2.64 eV in bulk $(Ga_{0.9}Zn_{0.1})(N_{0.9}O_{0.1})$ and $(Ga_{0.8}Zn_{0.2})(N_{0.8}O_{0.2})$, respectively[27].
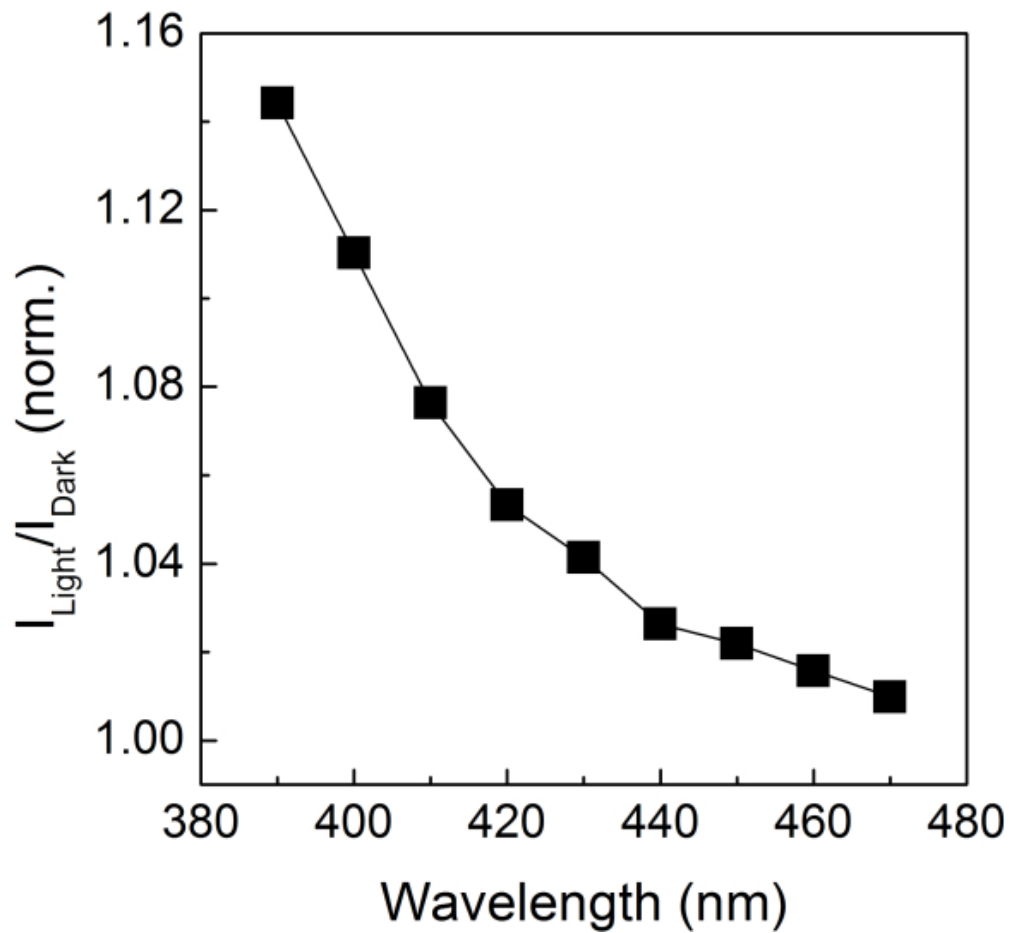
Figure 6.10: Photocurrent on-off ratio normalized by the incident light's power density plotted against wavelength. Each data point was obtained from Fig.6.9 by: $I_{Light}/I_{Dark}$ (norm.) = mean $I_{Light}$ ($t$: 70-88 s) / mean $I_{Dark}$ ($t$: 2-15 s) / (incident light power density).

## 6.6   Summary

In short, we have demonstrated a new synthesis route for crystalline $(GaN)_{1-x}(ZnO)_x$ solid-solution nanowires that utilizes nanostructured precursor materials prepared by sol-gel methods – a technique that is applicable to other semiconducting solid-solution nanostructures as well. From electrical transport measurements in individual nanowire FET devices, we have identified the conduction as n-type and determined the background carrier density ($\sim 10^{19}/cm^3$) and electron mobility ($\sim 1 cm^2/V{\cdot}s$). This low mobility value is consistent with chemical disorder and a large number of charge traps, as confirmed by the devices' photocurrent response. We have also determined the energy bandgap of $(Ga_{0.88}Zn_{0.12})(N_{0.88}O_{0.12})$ to be as much as $\sim 0.4$ - 0.5 eV lower than that of GaN or ZnO.

This work should be seen as a first step toward producing highly efficient photocalysts at visible-light wavelengths. To reduce the bandgap even further, it will be necessary to increase the ZnO fraction in the solid solution, which will require to lower the growth temperature or to use a different catalyst. In parallel, experiments are needed to determine the photocatalytic effectiveness of these $(GaN)_{1-x}(ZnO)_x$ crystalline nanowires.

# Chapter 7

# Summary

Semiconductor nanostructures are of great interest partially due to the flexibility of allowing control of their electronic and optical properties. By studying these properties, we can better understand the materials and therefore tailor them for advanced applications. In this dissertation, graphene and $(GaN)_{1-x}(ZnO)_x$ solid solution nanowires were studied.

In graphene FETs, low-frequency noise, which poses a limit on signal to noise ratio in broadband or low-frequency electrical circuit, has been studied. Peculiar noise-carrier density dependence has been observed, and explained by a Hooge relation with a mobility-dependent Hooge parameter. This model fits our data and most of the reported results. Suspended graphene FETs were also studied, and we found that the Hooge parameter was significantly reduced compared to on-substrate (not suspended) devices.

The magnetotransport properties of graphene were also studied. Metal-insulator transition at $n=0$ Landau level was studied in monolayer graphene, and a phase diagram was proposed, which summarized the metal and insulator phases in reported results and our own data. Besides monolayer graphene, we have also studied ABC-stacked trilayer graphene, because of its interesting cubic energy dispersion relation which is quite different from mono-

layer or bilayer graphene. We discovered that chiral fermions exist in the ABC-stacked trilayer graphene with Berry's phase $3\pi$ and have unusual Landau level quantization with 12-fold and 4-fold degeneracy in the $n{=}0$ and $n{>}0$ Landau levels, respectively.

Spacially resolved scanning photocurrent in a magnetic field was studied in graphene FETs. The unique geometry of a two-dimensional carrier gas confined close to the surface makes graphene particularly suitable for scanning probe experiments. By mapping the photocurrent across graphene in the quantum Hall regime, we demonstrated the formation of counter-propagating edge states with propagation direction determined by the unique Landau level spectrum and band bending at the edges of graphene.

Besides graphene, we have also studied $(GaN)_{1-x}(ZnO)_x$ solid solution nanowires, which are potential candidates as photocatalysts. The material was prepared by sol-gel methods and the nanowire structure and composition was analyzed with TEM, SEM, EDS and EELS. The nanowires we have studied have a composition $x \approx 0.12$, and an optical bandgap $\sim$2.7eV. Through electrical measurements, we found that the nanowire FETs showed n-type conduction, with background carrier density $\sim 10^{19}/cm^3$ and electron mobility $\sim 1cm^2/V \cdot s$. This low mobility value is consistent with chemical disorder and a large number of charge traps, as confirmed by the devices' photocurrent response.

# Bibliography

[1] K. S. Novoselov, A. K. Geim, S. V. Morozov, D. Jiang, Y. Zhang, S. V. Dubonos, I. V. Grigorieva, and A. A. Firsov. Electric field effect in atomically thin carbon films. *Science*, 306(5696):666–669, 2004.

[2] Changgu Lee, Xiaoding Wei, Jeffrey W. Kysar, and James Hone. Measurement of the elastic properties and intrinsic strength of monolayer graphene. *Science*, 321(5887): 385–388, 2008.

[3] Priscilla Kailian Ang, Wei Chen, Andrew Thye Shen Wee, and Kian Ping Loh. Solution-gated epitaxial graphene as pH sensor. *Journal of the American Chemical Society*, 130(44):14392–14393, 2008.

[4] F. Schedin, A. K. Geim, S. V. Morozov, E. W. Hill, P. Blake, M. I. Katsnelson, and K. S. Novoselov. Detection of individual gas molecules adsorbed on graphene. *Nat Mater*, 6(9):652–655, 2007.

[5] R. R. Nair, P. Blake, A. N. Grigorenko, K. S. Novoselov, T. J. Booth, T. Stauber, N. M. R. Peres, and A. K. Geim. Fine structure constant defines visual transparency of graphene. *Science*, 320(5881):1308–, 2008.

[6] Claire Berger, Zhimin Song, Tianbo Li, Xuebin Li, Asmerom Y. Ogbazghi, Rui Feng, Zhenting Dai, Alexei N. Marchenkov, Edward H. Conrad, Phillip N. First, and Walt A. de Heer. Ultrathin epitaxial graphite:2D electron gas properties and a route toward graphene-based nanoelectronics. *The Journal of Physical Chemistry B*, 108(52):19912– 19916, 2004.

[7] Claire Berger, Zhimin Song, Xuebin Li, Xiaosong Wu, Nate Brown, Cecile Naud, Didier Mayou, Tianbo Li, Joanna Hass, Alexei N. Marchenkov, Edward H. Conrad, Phillip N. First, and Walt A. de Heer. Electronic confinement and coherence in patterned epitaxial graphene. *Science*, 312(5777):1191–1196, 2006.

[8] Peter W. Sutter, Jan-Ingo Flege, and Eli A. Sutter. Epitaxial graphene on ruthenium. *Nat Mater*, 7(5):406–411, 2008.

[9] Keun Soo Kim, Yue Zhao, Houk Jang, Sang Yoon Lee, Jong Min Kim, Kwang S. Kim, Jong-Hyun Ahn, Philip Kim, Jae-Young Choi, and Byung Hee Hong. Large-scale pattern growth of graphene films for stretchable transparent electrodes. *Nature*, 457 (7230):706–710, 2009.

[10] Xuesong Li, Weiwei Cai, Jinho An, Seyoung Kim, Junghyo Nah, Dongxing Yang, Richard Piner, Aruna Velamakanni, Inhwa Jung, Emanuel Tutuc, Sanjay K. Banerjee, Luigi Colombo, and Rodney S. Ruoff. Large-area synthesis of high-quality and uniform graphene films on copper foils. *Science*, 324(5932):1312–1314, 2009.

[11] K. S. Novoselov, A. K. Geim, S. V. Morozov, D. Jiang, M. I. Katsnelson, I. V. Grigorieva, S. V. Dubonos, and A. A. Firsov. Two-dimensional gas of massless Dirac fermions in graphene. *Nature*, 438(7065):197–200, 2005.

[12] H. A. Fertig and L. Brey. Luttinger liquid at the edge of undoped graphene in a strong magnetic field. *Physical Review Letters*, 97(11):116805, 2006.

[13] Dmitry A. Abanin, Kostya S. Novoselov, Uli Zeitler, Patrick A. Lee, A. K. Geim, and L. S. Levitov. Dissipative quantum Hall effect in graphene near the Dirac point. *Physical Review Letters*, 98(19):196806, 2007.

[14] E. Shimshoni, H. A. Fertig, and G. Venketeswara Pai. Onset of an insulating zero-plateau quantum Hall state in graphene. *Physical Review Letters*, 102(20):206408, 2009.

[15] S. Das Sarma and Kun Yang. The enigma of the $\nu=0$ quantum Hall effect in graphene. *Solid State Communications*, 149(37-38):1502–1506, 2009.

[16] K. S. Novoselov, E. McCann, S. V. Morozov, V. I. Fal/'ko, M. I. Katsnelson, U. Zeitler, D. Jiang, F. Schedin, and A. K. Geim. Unconventional quantum Hall effect and Berry's phase of $2\pi$ in bilayer graphene. *Nat Phys*, 2(3):177–180, 2006.

[17] Kin Fai Mak, Jie Shan, and Tony F. Heinz. Electronic structure of few-layer graphene: Experimental demonstration of strong dependence on stacking sequence. *Physical Review Letters*, 104(17):176404, 2010.

[18] Wenjuan Zhu, Deborah Neumayer, Vasili Perebeinos, and Phaedon Avouris. Silicon nitride gate dielectrics and band gap engineering in graphene layers. *Nano Letters*, 10 (9):3572–3576, 2010.

[19] Yanping Liu, Sarjoosing Goolaup, Chandrasekhar Murapaka, Wen Siang Lew, and Seng Kai Wong. Effect of magnetic field on the electronic transport in trilayer graphene. *ACS Nano*, 4(12):7087–7092, 2010.

[20] Wenzhong Bao, Zeng Zhao, Hang Zhang, Gang Liu, Philip Kratz, Lei Jing, Jairo Velasco, Dmitry Smirnov, and Chun Ning Lau. Magnetoconductance oscillations and evidence for fractional quantum Hall states in suspended bilayer and trilayer graphene. *Phys. Rev. Lett.*, 105(24):246601, Dec 2010.

[21] F. Guinea, A. H. Castro Neto, and N. M. R. Peres. Electronic properties of stacks of graphene layers. *Solid State Communications*, 143(1-2):116–122, 2007.

[22] Mikito Koshino and Edward McCann. Trigonal warping and Berry's phase $N\pi$ in ABC-stacked multilayer graphene. *Phys. Rev. B*, 80(16):165409, Oct 2009.

[23] Fan Zhang, Bhagawan Sahu, Hongki Min, and A. H. MacDonald. Band structure of ABC-stacked graphene trilayers. *Physical Review B*, 82(3):035409, 2010.

[24] E. Becquerel. *C. R. Hebd. Séanc. Acad. Sci.*, 9:145, 1839.

[25] E. Becquerel. *Ann. Phys. Chemie*, 54:18, 1841.

[26] M. Ashokkumar. An overview on semiconductor particulate systems for photoproduction of hydrogen. *International Journal of Hydrogen Energy*, 23(6):427–438, 1998.

[27] Kazuhiko Maeda and Kazunari Domen. New non-oxide photocatalysts designed for overall water splitting under visible light. *The Journal of Physical Chemistry C*, 111 (22):7851–7861, 2007.

[28] P. R. Wallace. The band theory of graphite. *Phys. Rev.*, 71(9):622–634, May 1947.

[29] F. Guinea, A. H. Castro Neto, and N. M. R. Peres. Electronic states and Landau levels in graphene stacks. *Physical Review B (Condensed Matter and Materials Physics)*, 73 (24):245426, 2006.

[30] R. Saito, G. Dresselhaus, and M. Dresselhaus. *Physical properties of carbon nanotubes.* World Scientific Publishing Co. Pte. Ltd., 1998.

[31] A. K. Geim and K. S. Novoselov. The rise of graphene. *Nature Materials*, 6(3):183–191, 2007.

[32] M. Ezawa. Intrinsic Zeeman effect in graphene. *Journal of the Physical Society of Japan*, 76(9):12, 2007.

[33] Masato Aoki and Hiroshi Amawashi. Dependence of band structures on stacking and field in layered graphene. *Solid State Communications*, 142(3):123–127, 2007.

[34] A. H. Castro Neto, F. Guinea, N. M. R. Peres, K. S. Novoselov, and A. K. Geim. The electronic properties of graphene. *Reviews of Modern Physics*, 81(1):109, 2009.

[35] Eduardo Fradkin. Critical behavior of disordered degenerate semiconductors. I. Models, symmetries, and formalism. *Phys. Rev. B*, 33(5):3257–3262, Mar 1986.

[36] Jannik C. Meyer, A. K. Geim, M. I. Katsnelson, K. S. Novoselov, T. J. Booth, and S. Roth. The structure of suspended graphene sheets. *Nature*, 446(7131):60–63, 2007.

[37] J. C. Meyer, A. K. Geim, M. I. Katsnelson, K. S. Novoselov, D. Obergfell, S. Roth, C. Girit, and A. Zettl. On the roughness of single- and bi-layer graphene membranes. *Solid State Communications*, 143(1-2):101–109, 2007.

[38] Xu Du, Ivan Skachko, Anthony Barker, and Eva Y. Andrei. Approaching ballistic transport in suspended graphene. *Nat Nano*, 3(8):491–495, 2008.

[39] K. I. Bolotin, K. J. Sikes, J. Hone, H. L. Stormer, and P. Kim. Temperature-dependent transport in suspended graphene. *Physical Review Letters*, 101(9):096802, 2008.

[40] J. Moser, A. Barreiro, and A. Bachtold. Current-induced cleaning of graphene. *Applied Physics Letters*, 91(16):163513, 2007.

[41] V. P. Gusynin and S. G. Sharapov. Unconventional integer quantum Hall effect in graphene. *Physical Review Letters*, 95(14):146801, 2005.

[42] Igor A. Luk'yanchuk and Yakov Kopelevich. Phase analysis of quantum oscillations in graphite. *Physical Review Letters*, 93(16):166402, 2004.

[43] Yuanbo Zhang, Yan-Wen Tan, Horst L. Stormer, and Philip Kim. Experimental observation of the quantum Hall effect and Berry's phase in graphene. *Nature*, 438:201, 2005.

[44] Edward McCann and Vladimir I. Fal'ko. Landau-level degeneracy and quantum Hall effect in a graphite bilayer. *Physical Review Letters*, 96(8):086805, 2006.

[45] Edward McCann. Asymmetry gap in the electronic band structure of bilayer graphene. *Phys. Rev. B*, 74(16):161403, Oct 2006.

[46] Taisuke Ohta, Aaron Bostwick, Thomas Seyller, Karsten Horn, and Eli Rotenberg. Controlling the electronic structure of bilayer graphene. *Science*, 313(5789):951–954, 2006.

[47] J. R. Williams. *Electronic Transport in Graphene: p-n Junctions, Shot Noise, and Nanoribbons*. PhD thesis, Harvard University, Cambridge, Massachusetts, May 2009.

[48] Yu-Ming Lin and Phaedon Avouris. Strong suppression of electrical noise in bilayer graphene nanodevices. *Nano Letters*, 8(8):2119–2125, 2008.

[49] A. C. Ferrari, J. C. Meyer, V. Scardaci, C. Casiraghi, M. Lazzeri, F. Mauri, S. Piscanec, D. Jiang, K. S. Novoselov, S. Roth, and A. K. Geim. Raman spectrum of graphene and graphene layers. *Physical Review Letters*, 97(18):187401, 2006.

[50] A. N. Pal and A. Ghosh. Ultralow noise field-effect transistor from multilayer graphene. *Applied Physics Letters*, 95(8):3, 2009.

[51] G. Liu, W. Stillman, S. Rumyantsev, Q. Shao, M. Shur, and A. A. Balandin. Low-frequency electronic noise in the double-gate single-layer graphene transistors. *Applied Physics Letters*, 95(3):033103, 2009.

[52] Iddo Heller, Sohail Chatoor, Jaan Ma?nnik, Marcel A. G. Zevenbergen, Jeroen B. Oostinga, Alberto F. Morpurgo, Cees Dekker, and Serge G. Lemay. Charge noise in graphene transistors. *Nano Letters*, 10(5):1563–1567, 2010.

[53] Guangyu Xu, Carlos M. Torres, Yuegang Zhang, Fei Liu, Emil B. Song, Minsheng Wang, Yi Zhou, Caifu Zeng, and Kang L. Wang. Effect of spatial charge inhomogeneity on 1/f noise behavior in graphene. *Nano Letters*, 10(9):3312–3317, 2010.

[54] S. A. Imam, S. Sabri, and T. Szkopek. Low-frequency noise and hysteresis in graphene field-effect transistors on oxide. *Micro & Nano Letters*, 5(1):37–41, 2010.

[55] Zengguang Cheng, Qiang Li, Zhongjun Li, Qiaoyu Zhou, and Ying Fang. Suspended graphene sensors with improved signal and reduced noise. *Nano Letters*, 10(5):1864–1868, 2010.

[56] S Rumyantsev, G. Liu, W. Stillman, M. Shur, and A.A. Balandin. Electrical and noise characteristics of graphene field-effect transistors: ambient effects, noise sources and physical mechanisms. *Journal of Physics: Condensed Matter*, 22(39):395302, 2010.

[57] F. N. Hooge. 1/f noise is no surface effect. *Physics Letters A*, 29(3):139–140, 1969.

[58] F.N. Hooge, T.G.M. Kleinpenning, and L.K.J. Vandamme. Experimental studies on 1/f noise. *Reports on Progress in Physics*, 44(5):479, 1981.

[59] F. N. Hooge. 1/f noise sources. *Electron Devices, IEEE Transactions on*, 41(11): 1926–1935, 1994.

[60] Kentaro Nomura and Allan H. MacDonald. Quantum Hall ferromagnetism in graphene. *Physical Review Letters*, 96(25):256602, 2006.

[61] Shaffique Adam, E. H. Hwang, V. M. Galitski, and S. Das Sarma. A self-consistent theory for graphene transport. *Proceedings of the National Academy of Sciences*, 104 (47):18392–18397, 2007.

[62] E. H. Hwang, S. Adam, and S. Das Sarma. Carrier transport in two-dimensional graphene layers. *Physical Review Letters*, 98(18):186806, 2007.

[63] Igor A. Luk'yanchuk and Alexander M. Bratkovsky. Lattice-induced double-valley degeneracy lifting in graphene by a magnetic field. *Physical Review Letters*, 100(17): 176404, 2008.

[64] S. Ilani, J. Martin, E. Teitelbaum, J. H. Smet, D. Mahalu, V. Umansky, and A. Yacoby. The microscopic nature of localization in the quantum Hall effect. *Nature*, 427(6972): 328–332, 2004.

[65] J. Martin, N. Akerman, G. Ulbricht, T. Lohmann, J. H. Smet, K. von Klitzing, and A. Yacoby. Observation of electron-hole puddles in graphene using a scanning single-electron transistor. *Nat Phys*, 4(2):144–148, 2008. 10.1038/nphys781.

[66] Y. Zhang, Z. Jiang, J. P. Small, M. S. Purewal, Y. W. Tan, M. Fazlollahi, J. D. Chudow, J. A. Jaszczak, H. L. Stormer, and P. Kim. Landau-level splitting in graphene in high magnetic fields. *Physical Review Letters*, 96(13):136806, 2006.

[67] Z. Jiang, Y. Zhang, H. L. Stormer, and P. Kim. Quantum Hall states near the charge-neutral Dirac point in graphene. *Physical Review Letters*, 99(10):106802, 2007.

[68] A. J. M. Giesbers, U. Zeitler, M. I. Katsnelson, L. A. Ponomarenko, T. M. Mohiuddin, and J. C. Maan. Quantum-hall activation gaps in graphene. *Physical Review Letters*, 99(20):206803, 2007.

[69] Joseph G. Checkelsky, Lu Li, and N. P. Ong. Zero-energy state in graphene in a high magnetic field. *Physical Review Letters*, 100(20):206801, 2008.

[70] A. J. M. Giesbers, L. A. Ponomarenko, K. S. Novoselov, A. K. Geim, M. I. Katsnelson, J. C. Maan, and U. Zeitler. Gap opening in the zeroth Landau level of graphene. *Physical Review B*, 80(20):201403, 2009.

[71] L. Zhang, J. Camacho, H. Cao, Y. P. Chen, M. Khodas, D. E. Kharzeev, A. M. Tsvelik, T. Valla, and I. A. Zaliznyak. Breakdown of the N=0 quantum Hall state in graphene: Two insulating regimes. *Physical Review B*, 80(24):241412, 2009.

[72] Xu Du, Ivan Skachko, Fabian Duerr, Adina Luican, and Eva Y. Andrei. Fractional quantum Hall effect and insulating phase of Dirac electrons in graphene. *Nature*, 462: 192–195, 2009.

[73] Kirill I. Bolotin, Fereshte Ghahari, Michael D. Shulman, Horst L. Stormer, and Philip Kim. Observation of the fractional quantum Hall effect in graphene. *Nature*, 462(7270): 196–199, 2009.

[74] Benjamin E. Feldman, Jens Martin, and Amir Yacoby. Broken-symmetry states and divergent resistance in suspended bilayer graphene. *Nat Phys*, 5(12):889–893, 2009.

[75] H. W. Jiang, C. E. Johnson, K. L. Wang, and S. T. Hannahs. Observation of magnetic-field-induced delocalization: Transition from Anderson insulator to quantum Hall conductor. *Physical Review Letters*, 71(9):1439, 1993.

[76] R J F Hughes and et al. Magnetic-field-induced insulator-quantum Hall-insulator transition in a disordered two-dimensional electron gas. *Journal of Physics: Condensed Matter*, 6(25):4763, 1994.

[77] D. Shahar, D. C. Tsui, M. Shayegan, R. N. Bhatt, and J. E. Cunningham. Universal conductivity at the quantum Hall liquid to insulator transition. *Physical Review Letters*, 74(22):4511, 1995.

[78] Alexander Punnoose and Alexander M. Finkel'stein. Metal-insulator transition in disordered two-dimensional electron systems. *Science*, 310(5746):289–291, 2005.

[79] V. T. Dolgopolov, G. V. Kravchenko, A. A. Shashkin, and S. V. Kravchenko. Metal-insulator transition in si inversion layers in the extreme quantum limit. *Physical Review B*, 46(20):13303, 1992.

[80] A. M. Dykhne and I. M. Ruzin. Theory of the fractional quantum Hall effect: The two-phase model. *Physical Review B*, 50(4):2369, 1994.

[81] C. P. Burgess and Brian P. Dolan. Quantum Hall effect in graphene: Emergent modular symmetry and the semicircle law. *Physical Review B*, 76(11):113406, 2007.

[82] Mikito Koshino. Interlayer screening effect in graphene multilayers with *ABA* and *ABC* stacking. *Phys. Rev. B*, 81(12):125304, Mar 2010.

[83] Yuanbo Zhang, Tsung-Ta Tang, Caglar Girit, Zhao Hao, Michael C. Martin, Alex Zettl, Michael F. Crommie, Y. Ron Shen, and Feng Wang. Direct observation of a widely tunable bandgap in bilayer graphene. *Nature*, 459(7248):820–823, 2009.

[84] M. F. Craciun, S. Russo, M. Yamamoto, J. B. Oostinga, A. F. Morpurgo, and S. Tarucha. Trilayer graphene is a semimetal with a gate-tunable band overlap. *Nature Nanotechnology*, 4(6):383–388, 2009.

[85] Wenjuan Zhu, Vasili Perebeinos, Marcus Freitag, and Phaedon Avouris. Carrier scattering, mobilities, and electrostatic potential in monolayer, bilayer, and trilayer graphene. *Physical Review B*, 80(23):235402, 2009.

[86] Chun Hung Lui, Zhiqiang Li, Zheyuan Chen, Paul V. Klimov, Louis E. Brus, and Tony F. Heinz. Imaging stacking order in few-layer graphene. *Nano Letters*, pages null–null, 2010.

[87] Yufeng Hao, Yingying Wang, Lei Wang, Zhenhua Ni, Ziqian Wang, Rui Wang, Chee Keong Koo, Zexiang Shen, and John T. L. Thong. Probing layer number and stacking order of few-layer graphene by Raman spectroscopy. *Small*, 6(2):195–200, 2010.

[88] P. T. Coleridge, R. Stoner, and R. Fletcher. Low-field transport coefficients in GaAs/Ga$_{1-x}$Al$_x$As heterostructures. *Physical Review B*, 39(2):1120, 1989.

[89] T. Chakraborty and P. Pietilainen. *The quantum Hall effects*. Springer, Berlin, 1995.

[90] Kent L. McCormick, Michael T. Woodside, Mike Huang, Mingshaw Wu, Paul L. McEuen, Cem Duruoz, and J. S. Harris. Scanned potential microscopy of edge and bulk currents in the quantum Hall regime. *Physical Review B*, 59(7):4654, 1999.

[91] E. Ahlswede, P. Weitz, J. Weis, K. von Klitzing, and K. Eberl. Hall potential profiles in the quantum Hall regime measured by a scanning force microscope. *Physica B: Condensed Matter*, 298(1-4):562–566, 2001.

[92] J. R. Williams, L. DiCarlo, and C. M. Marcus. Quantum Hall effect in a gate-controlled p-n junction of graphene. *Science*, 317(5838):638–641, 2007.

[93] Barbaros Ozyilmaz, Pablo Jarillo-Herrero, Dmitri Efetov, Dmitry A. Abanin, Leonid S. Levitov, and Philip Kim. Electronic transport and quantum Hall effect in bipolar graphene p-n-p junctions. *Physical Review Letters*, 99(16):166804, 2007.

[94] Dong-Keun Ki, Sanghyun Jo, and Hu-Jong Lee. Observation of chiral quantum-Hall edge states in graphene. *Applied Physics Letters*, 94(16):162113, 2009.

[95] M. Buttiker. Absence of backscattering in the quantum Hall effect in multiprobe conductors. *Physical Review B*, 38(14):9375, 1988.

[96] D. B. Chklovskii, B. I. Shklovskii, and L. I. Glazman. Electrostatics of edge channels. *Physical Review B*, 46(7):4026, 1992.

[97] J. Martin, N. Akerman, G. Ulbricht, T. Lohmann, K. von Klitzing, J. H. Smet, and A. Yacoby. The nature of localization in graphene under quantum Hall conditions. *Nat Phys*, 5(9):669–674, 2009.

[98] M. R. Connolly, K. L. Chiou, C. G. Smith, D. Anderson, G. A. C. Jones, A. Lombardo, A. Fasoli, and A. C. Ferrari. Scanning gate microscopy of current-annealed single layer graphene. *Applied Physics Letters*, 96(11):113501, 2010.

[99] J. R. Williams, D. A. Abanin, L. DiCarlo, L. S. Levitov, and C. M. Marcus. Quantum Hall conductance of two-terminal graphene devices. *Physical Review B*, 80(4):045408, 2009.

[100] Dmitry A. Abanin and Leonid S. Levitov. Conformal invariance and shape-dependent conductance of graphene samples. *Physical Review B*, 78(3):035416, 2008.

[101] Eduardo J. H. Lee, Kannan Balasubramanian, Ralf Thomas Weitz, Marko Burghard, and Klaus Kern. Contact and edge effects in graphene devices. *Nat Nano*, 3(8):486–490, 2008.

[102] Fengnian Xia, Thomas Mueller, Roksana Golizadeh-Mojarad, Marcus Freitag, Yu-ming Lin, James Tsang, Vasili Perebeinos, and Phaedon Avouris. Photocurrent imaging and efficient photon detection in a graphene transistor. *Nano Letters*, 9(3):1039–1044, 2009.

[103] T. Mueller, F. Xia, M. Freitag, J. Tsang, and Ph. Avouris. Role of contacts in graphene transistors: A scanning photocurrent study. *Physical Review B*, 79(24):245430, 2009.

[104] Jiwoong Park, Y. H. Ahn, and Carlos Ruiz-Vargas. Imaging of photocurrent generation and collection in single-layer graphene. *Nano Letters*, 9(5):1742–1746, 2009.

[105] Xiaodong Xu, Nathaniel M. Gabor, Jonathan S. Alden, Arend M. van der Zande, and Paul L. McEuen. Photo-thermoelectric effect at a graphene interface junction. *Nano Letters*, 10(2):562–566, 2009.

[106] R. J. F. van Haren, W. de Lange, F. A. P. Blom, and J. H. Wolter. Imaging of edge channels in the integer quantum Hall regime by the lateral photoelectric effect. *Physical Review B*, 52(8):5760, 1995.

[107] A. A. Shashkin, A. J. Kent, J. R. Owers-Bradley, A. J. Cross, P. Hawker, and M. Henini. Hall photovoltage imaging of the edge of a quantum Hall device. *Physical Review Letters*, 79(25):5114, 1997.

[108] R. J. F. van Haren, F. A. P. Blom, and J. H. Wolter. Direct observation of edge channels in the integer quantum Hall regime. *Physical Review Letters*, 74(7):1198, 1995.

[109] D. E. Ioannou and C. A. Dimitriadis. A sem-ebic minority-carrier diffusion-length measurement technique. *Electron Devices, IEEE Transactions on*, 29(3):445–450, 1982.

[110] Michael D. Kelzenberg, Daniel B. Turner-Evans, Brendan M. Kayes, Michael A. Filler, Morgan C. Putnam, Nathan S. Lewis, and Harry A. Atwater. Photovoltaic measurements in single-nanowire silicon solar cells. *Nano Letters*, 8(2):710–714, 2008.

[111] D. B. Chklovskii, K. A. Matveev, and B. I. Shklovskii. Ballistic conductance of inter-acting electrons in the quantum Hall regime. *Physical Review B*, 47(19):12605, 1993.

[112] S. Kicin, A. Pioda, T. Ihn, K. Ensslin, D. C. Driscoll, and A. C. Gossard. Local backscattering in the quantum Hall regime. *Physical Review B*, 70(20):205302, 2004.

[113] Kazuhiko Maeda, Kentaro Teramura, Daling Lu, Tsuyoshi Takata, Nobuo Saito, Ya-sunobu Inoue, and Kazunari Domen. Photocatalyst releasing hydrogen from water. *Nature*, 440(7082):295–295, 2006.

[114] Lin Lin Jensen, James T. Muckerman, and Marshall D. Newton. First-principles stud-ies of the structural and electronic properties of the (Ga1-xZnx)(N1-xOx) solid solution photocatalyst. *The Journal of Physical Chemistry C*, 112(9):3439–3446, 2008.

[115] M. Gratzel. *Energy resources through photochemistry and catalysis*. Academic Press, New York, NY, 1983.

[116] Xinjian Feng, Lin Feng, Meihua Jin, Jin Zhai, Lei Jiang, and Daoben Zhu. Reversible super-hydrophobicity to super-hydrophilicity transition of aligned ZnO nanorod films. *Journal of the American Chemical Society*, 126(1):62–63, 2004.

[117] R. S. Wagner and W. C. Ellis. Vapor-liquid-solid mechanism of crystal growth and its application to silicon. *Trans. Metall. Soc. AIME*, 233:1053–1064, 1965.

[118] Wei-Qiang Han and A. Zettl. GaN nanorods coated with pure BN. *Applied Physics Letters*, 81(26):5051–5053, 2002.

[119] Yu Huang, Xiangfeng Duan, Yi Cui, and Charles M. Lieber. Gallium nitride nanowire nanodevices. *Nano Letters*, 2(2):101–104, 2002.

[120] R. Martel, T. Schmidt, H. R. Shea, T. Hertel, and Ph. Avouris. Single- and multi-wall carbon nanotube field-effect transistors. *Applied Physics Letters*, 73(17):2447–2449, 1998.

[121] D. Tham, C. Y. Nam, and J. E. Fischer. Defects in GaN nanowires. *Advanced Func-tional Materials*, 16(9):1197–1202, 2006.

[122] Zhiyong Fan, Dawei Wang, Pai-Chun Chang, Wei-Yu Tseng, and Jia G. Lu. ZnO nanowire field-effect transistor and oxygen sensing property. *Applied Physics Letters*, 85(24):5923–5925, 2004.

[123] Orazio Berolo, John C. Woolley, and J. A. Van Vechten. Effect of disorder on the conduction-band effective mass, valence-band spin-orbit splitting, and the direct band gap in III-V alloys. *Physical Review B*, 8(8):3794, 1973.

[124] B. Monemar, O. Lagerstedt, and H. P. Gislason. Properties of Zn-doped VPE-grown GaN. I. Luminescence data in relation to doping conditions. *Journal of Applied Physics*, 51(1):625–639, 1980.

[125] Takeshi Hirai, Kazuhiko Maeda, Masaaki Yoshida, Jun Kubota, Shigeru Ikeda, Michio Matsumura, and Kazunari Domen. Origin of visible light absorption in GaN-rich (Ga1-xZnx)(N1-xOx) photocatalysts. *The Journal of Physical Chemistry C*, 111(51): 18853–18855, 2007.

[126] Harvey Scher and Elliott W. Montroll. Anomalous transit-time dispersion in amorphous solids. *Physical Review B*, 12(6):2455, 1975.

[127] J. M. Hvam and M. H. Brodsky. Dispersive transport and recombination lifetime in phosphorus-doped hydrogenated amorphous silicon. *Physical Review Letters*, 46(5): 371, 1981.

[128] Joseph Orenstein and Marc Kastner. Photocurrent transient spectroscopy: Measurement of the density of localized states in a -$As_2Se_3$. *Physical Review Letters*, 46(21): 1421, 1981.

[129] Michael E. Levinshtein, Sergey L. Rumyantsev, and Michael S. Shur. *Properties of Advanced Semiconductor Materials : GaN, AlN, InN, BN, SiC, SiGe*. Wiley-Interscience, 1st edition, 2001.

[130] Q. Chen, J.W. Yang, M. Blasingame, C. Faber, A.T. Ping, and I. Adesida. Microwave electronics device applications of AlGaN/GaN heterostructures. *Materials Science and Engineering*, B59:395–400, 1999.

[131] Fan Ren and John C. Zolper. *Wide Energy Bandgap Electronic Devices*. World Scientific Publishing Co. Pte. Ltd., 2003.

# Appendix A

# Hydrostatic Pressure Study of AlGaN/GaN High Electron Mobility Transistors (HEMT)

GaN HEMT has a great potential for high voltage, high power and high speed electronic applications due to its fundamental properties such as wide band gap, high breakdown voltage and high mobility. However, it still lacks solid reliability. For example, it suffers power degradation during DC or RF stress. Understanding the physical mechanisms behind the device degradation is important to improve the device reliability.

## A.1   Crystal and Electronic structures of GaN

GaN have two types of crystal structures, wurtzite and zinc blende, as shown in Fig.A.1 (a) and (b), respectively. These two different crystal structures have slightly different energy band structures. Since wurtzite is the structure of our devices, I will focus on wurtzite GaN.
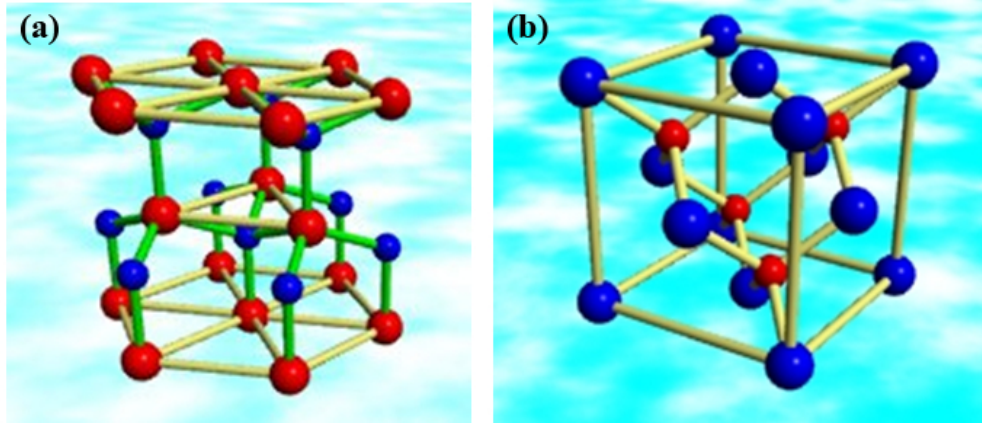
Figure A.1: Crystal structures of GaN (a) Wurtzite structure. (b) Zinc blende structure.

The energy band structure of wurzite GaN, shown in Fig.A.2, has 3.39 eV direct band gap at 300K[129]. The wide band gap, coming along with high breakdown voltage, makes it a good material for high power electronic applications.

## A.2 Structures of AlGaN/GaN HEMT

As shown in Fig.A.3(a), the heterostructure is grown on top of SiC substrate, due to its good lattice match to GaN or AlN (96.5%) and high thermal conductivity to dissipate generated heat efficiently[130]. The 2DEG formed on the interface between AlGaN and GaN is due to spontaneous and piezo-electric polarization, which is different from standard 2DEG formed by intentional doping. The AlGaN has an Al content of ∼28%.

The layout of AlGaN/GaN HEMT, with source, drain and gate marked, is shown in Fig.A.3(b). The transistor has four parallel FET devices connected together which can be seen from the four contact fingers on gate. A typical FET device has 50–100 $\mu m$-wide gate, a drain-source distance of 2–4 $\mu m$ and a gate-gate distance of 20–50 $\mu m$. For fair comparison,
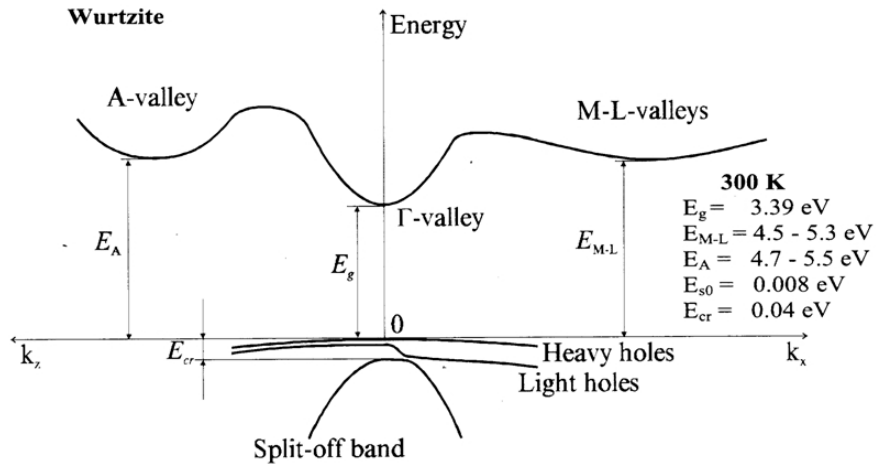
Figure A.2: Energy band structure of wurtzite GaN[129].
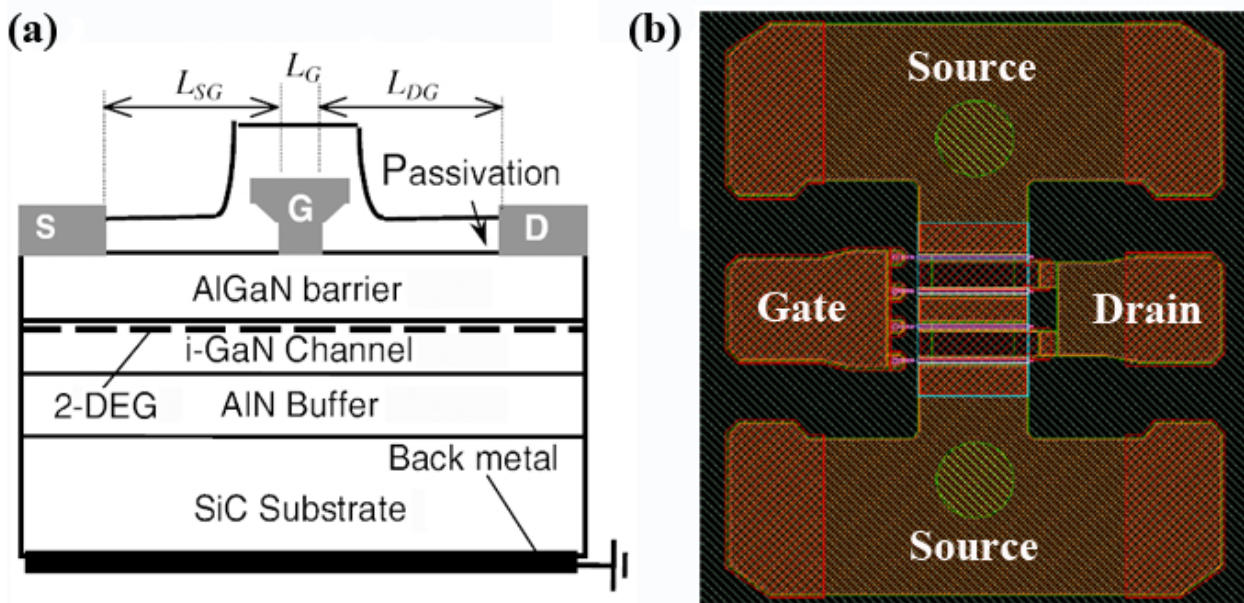


Figure A.3: (a) Cross-sectional view of AlGaN/GaN HEMT. (b) Planar layout of AlGaN/GaN HEMT
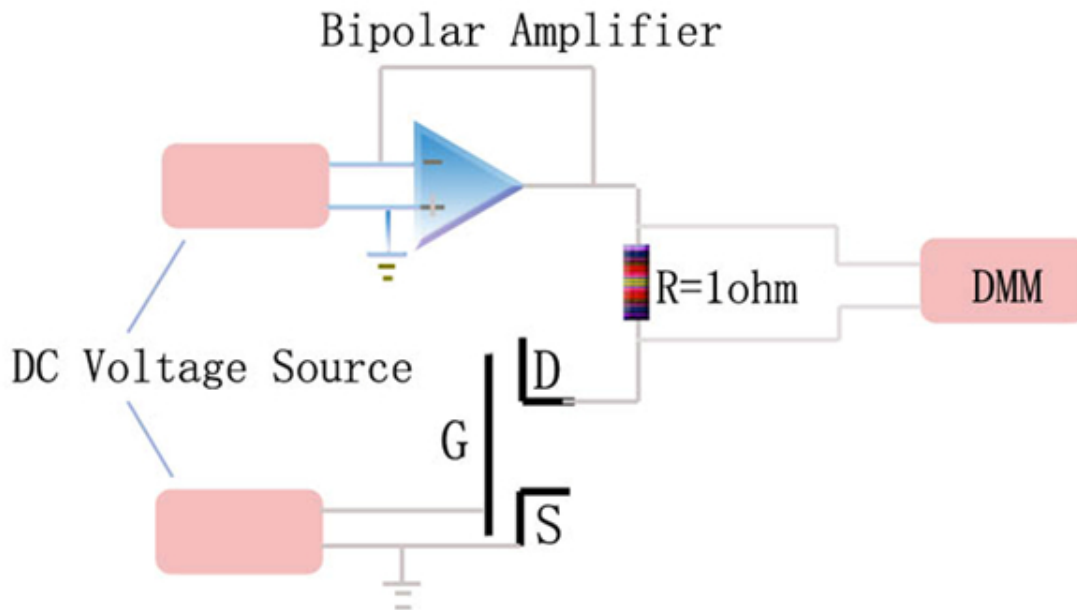
Figure A.4: Experimental setup for $I_D - V_{DS}$ and $I_D - V_G$ measurements.

in the measurements of devices with different lengths, quantities were normalized to the lengths.

## A.3   Measurement setup

As shown in Fig.A.4, in the electrical measurements, two Keithley 230 voltage sources were used to provide drain-source $(V_{DS})$ and gate $(V_G)$ voltage. For the drain-source voltage, a bipolar amplifier (HP 6825A bipolar power supply/amplifier) is connected in series with the device and voltage source, and this is due to the device's high current demand (up to 0.8 Ampere) which standard voltage sources won't be able to supply. The drain current $(I_D)$ is measured by measuring the voltage across a 1$\Omega$ resistor which is connected to the device drain contact in series.
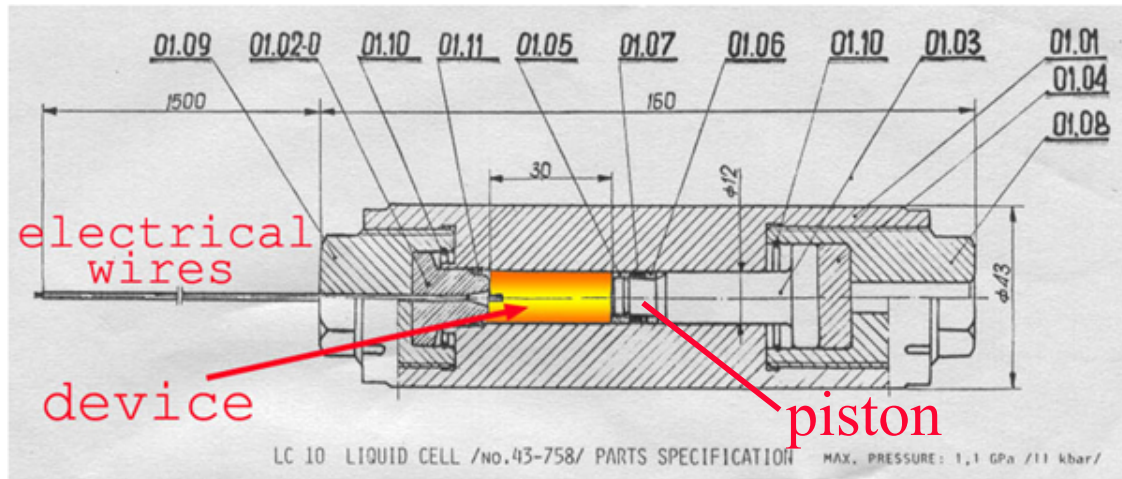
Figure A.5: Diagram of pressure cell with cables for electrical measurements.

For hydrostatic pressure measurement, a beryllium copper liquid pressure cell, is used and the diagram is shown in Fig.A.5. It is filled with kerosene and compressed from the outside with a hydraulic press to supply pressure up to 15kbar within the cell. The piston and electrical feedthrough are on opposite sides of the pressure cell, as indicated in Fig.A.5, and the pressure is sealed with metal gaskets. The electrical feedthrough has twelve wires: eight for electrical measurements and four for pressure measurement with a heavily doped bulk n-InSb single crystal as pressure gauge in a four-terminal measurement configuration. By measuring the resistance of the pressure gauge, we can calculate the hydrostatic pressure inside the cell using the equation $r(P) = R(P,T)/R(0,T) = 0.9996 + 1.98 \times 10^{-2} \times P + 4.05 \times 10^{-4} \times P^2$.
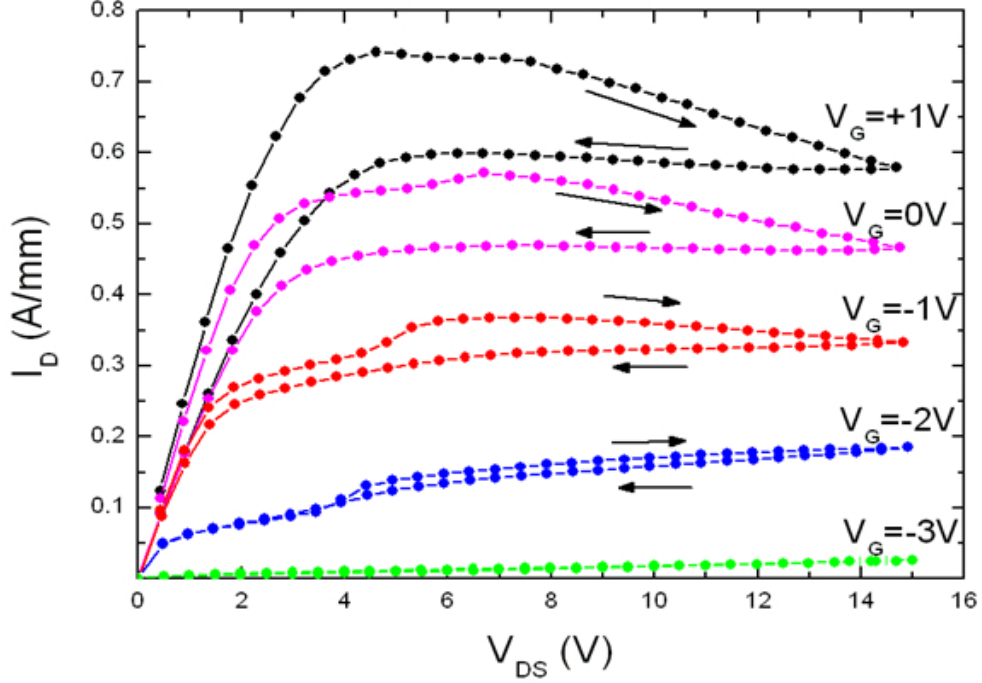
Figure A.6: $I_D - V_{DS}$ with $V_G$ from -3V to +1V at 1V interval, hysteresis is due to current collapse.

## A.4 Results of hydrostatic pressure study and stress study

First, we measured the $I_D - V_{DS}$ curves with different $V_G$ and the results are shown in Fig.A.6. The device is n-type, with larger $I_{DS}$ at more positive $V_G$. Except for $V_G$=-3V, all the other $V_G$ in the figure show hysteresis. The reduction in $I_D$ at low $V_{DS}$ after the application of a high $V_{DS}$ is usually called *current collapse*, which is typically due to the trapping of hot electrons in the buffer and donor layers adjacent to the conduction channel[131].

After that, we proceeded to do measurements under hydrostatic pressure. As shown in
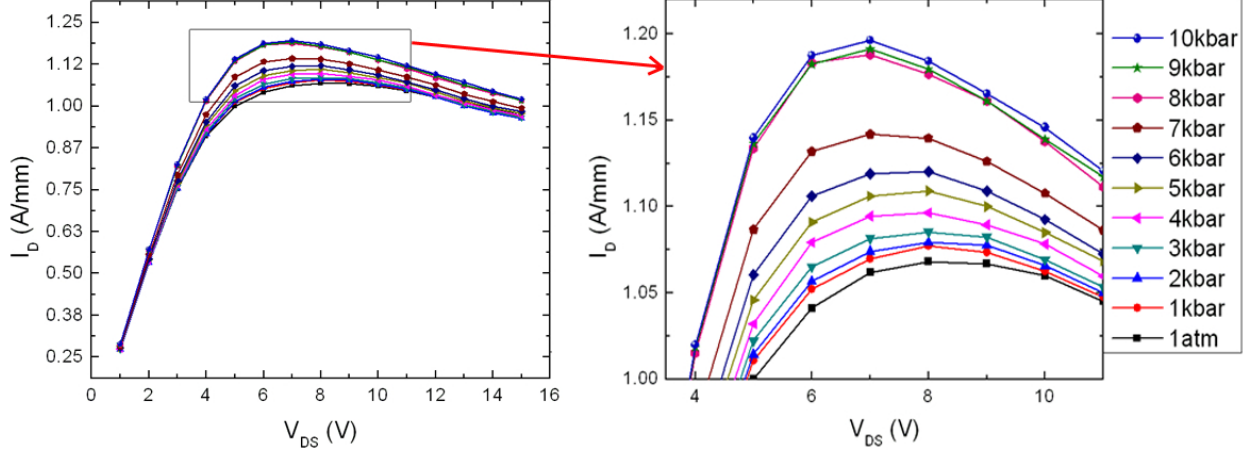
Figure A.7: $I_D - V_{DS}$ with $V_G = +1V$ in hydrostatic pressure from 1bar to 10kbar at 1kbar interval. The square in the left figure is magnified and shown in the right figure.

Fig.A.7, $I_D - V_{DS}$ with $V_G = +1V$ in pressures from 1atm ($\sim$1bar) to 10kbar at 1kbar interval are plotted. Due to the hysteresis shown in Fig.A.6, only the curves measured while increasing $V_{DS}$ are plotted, generally, the higher pressure the higher $I_D - V_{DS}$ curve. As shown in the magnified part on the right hand side of Fig.A.7, the maximum $I_D$ increases with pressure monotonically. Since the 2DEG in AlGaN/GaN HEMT is generated by spontaneous and piezo-electric polarizations, this observation suggests that the external hydrostatic pressure increases the overall polarizations which gives rise to higher charge carriers and higher $I_D$.

When taking a fresh AlGaN/GaN HEMT, after a few measurements, there will be a current degradation which is only partially recoverable. In order to study this behavior in detail, a time dependent measurement was designed, where device was stressed at $V_G = -3V, V_{DS} = 25V$ for 20 minutes and then relaxed at $V_G = 0V, V_{DS} = 0V$ for 20 minutes, then stressed again for 20 minutes. During this 60-minute measurement, the $I_D$ at $V_G = -1V, V_{DS} = 7V$ (close to the maximum $I_D$) was checked every 30 seconds, and the results are shown in Fig.A.8. The first point corresponds to $I_D$ of a fresh device. After a 20-minute
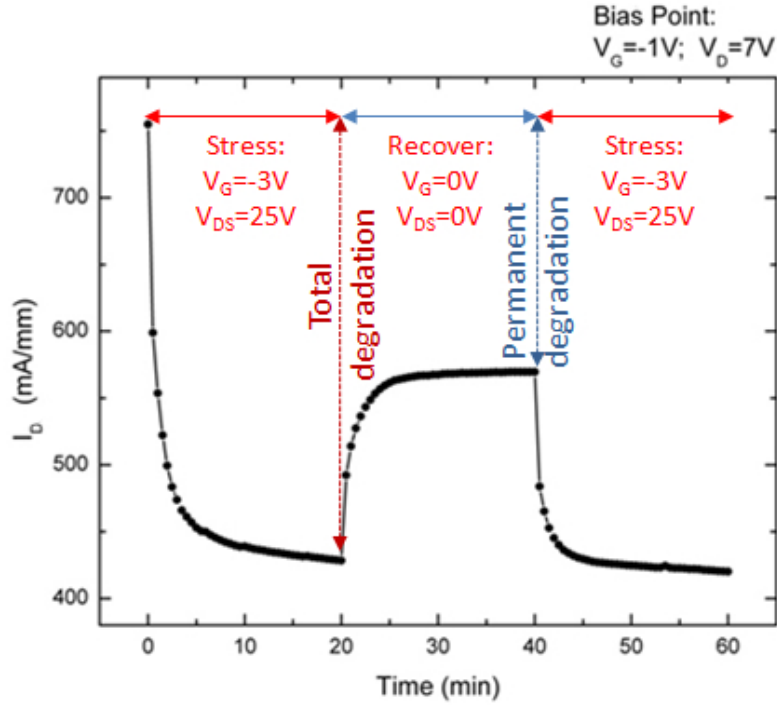
Figure A.8: Time dependent $I_D$ when the device goes through stress and recovery stage. There is a permanent degradation even after the stress is removed in the recovery stage.

stress, $I_D$ degrades by more than 40%. When the stress was removed, $I_D$ slowly recovered but not to the same value as in the fresh device. The difference between the recovered value and the fresh device's value was a permanent degradation. If we stressed the device again, $I_D$ quickly degraded to former stress test value.

We used a similar test method on AlGaN/GaN HEMT in hydrostatic pressure. Similarly, we chose $V_G = -20V, V_{DS} = 0V$ as stress condition for twelve consecutive hours, followed by recovery condition $V_G = 0V, V_{DS} = 0V$ for half an hour, and then stress again in different pressure, so on and so forth. The $I_D$ at $V_G = 1.5V, V_{DS} = 5V$ was monitored every minute, and the results, excluding recovery phase data, are shown in Fig.A.9, where we applied
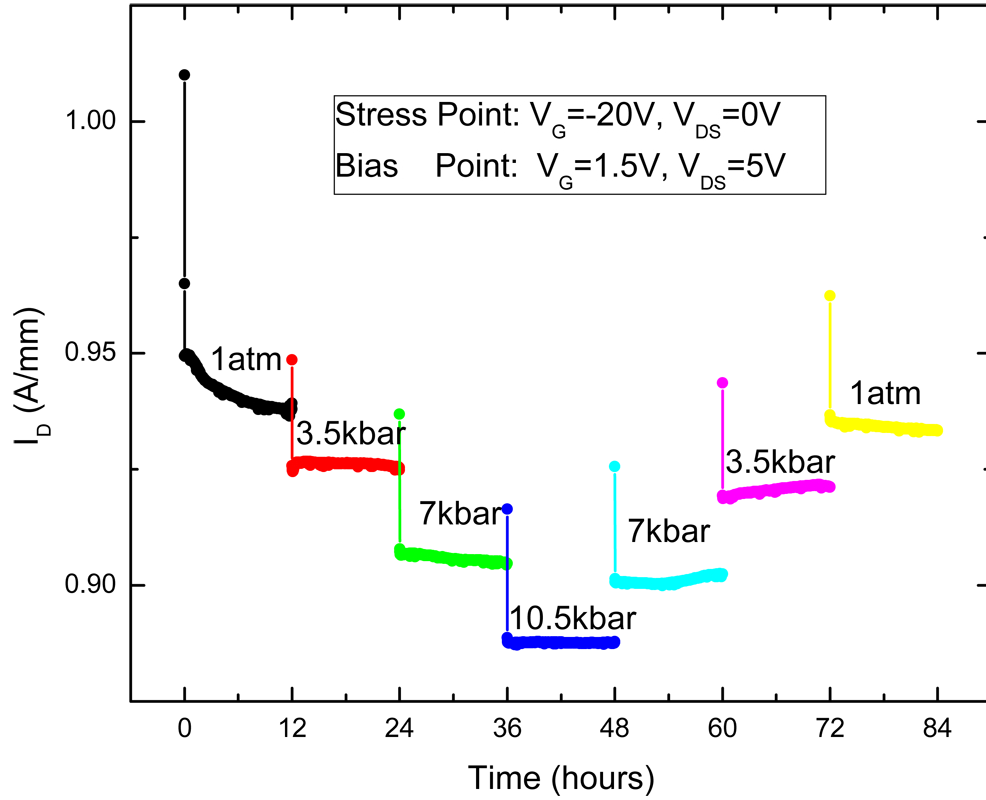
Figure A.9: Stress test for 84 consecutive hours in hydrostatic pressure 1atm, 3.5kbar, 7kbar, 10.5kbar, 7kbar, 3.5kbar and 1atm with 12 hours in each pressure. The stress condition is $V_G = -20V, V_{DS} = 0V$ and $I_D$ reading condition is $V_G = 1.5V, V_{DS} = 5V$.

hydrostatic pressure of 1atm, 3.5kbar, 7kbar, 10.5kbar, 7kbar, 3.5kbar and 1atm consecutively. The first $I_D$ point is always higher than the last $I_D$ point in the previous pressure stress data. The saturated $I_D$ with stress decreases with increasing pressure and increases with decreasing pressure in Fig.A.9. This suggests that, although external pressure helps to increase charge carrier (shown in Fig.A.7), with hours of stress it actually facilitates the current degradation, which results in lower $I_D$ while stressed in higher hydrostatic pressure.